The Astrophysical Journal, 988:215 (37pp), 2025 August 1 https://doi.org/10.3847/1538-4357/ade443

Timescales of Polycyclic Aromatic Hydrocarbon and Dust Continuum Emission from Gas Clouds Compared to Molecular Gas Cloud Lifetimes in PHANGS-JWST Galaxies

Jaeyeon Kim[1,27], Mélanie Chevance[2,3], Lise Ramambason[2], Kathryn Kreckel[4], Ralf S. Klessen[2,5,6,7], Daniel A. Dale[8], Adam K. Leroy[9,10], Karin Sandstrom[11], Ryan Chown[9], Thomas G. Williams[12], Sumit K. Sarbadhicary[9,10,13], Francesco Belfiore[14], Frank Bigiel[15], Enrico Congiu[16], Oleg V. Egorov[4], Eric Emsellem[17], Simon C. O. Glover[2], Kathryn Grasha[18,28], Annie Hughes[19], J. M. Diederik Kruijssen[3], Janice C. Lee[20], Debosmita Pathak[9,10], Ismael Pessa[21], Erik Rosolowsky[22], Jiayi Sun[23,25], Jessica Sutter[24], and David A. Thilker[13]

[1] Kavli Institute for Particle Astrophysics & Cosmology (KIPAC), Stanford University, CA 94305, USA; jyeonkim@stanford.edu
[2] Universität Heidelberg, Zentrum für Astronomie, Institut für Theoretische Astrophysik, Albert-Ueberle-Str 2, D-69120 Heidelberg, Germany
[3] Cosmic Origins Of Life (COOL) Research DAO, Germany[26]
[4] Astronomisches Rechen-Institut, Zentrum für Astronomie der Universität Heidelberg, Mönchhofstr. 12-14, D-69120 Heidelberg, Germany
[5] Universität Heidelberg, Interdisziplinäres Zentrum für Wissenschaftliches Rechnen, Im Neuenheimer Feld 205, 69120 Heidelberg, Germany
[6] Harvard-Smithsonian Center for Astrophysics, 60 Garden Street, Cambridge, MA 02138, USA
[7] Elizabeth S. and Richard M. Cashin Fellow at the Radcliffe Institute for Advanced Studies at Harvard University, 10 Garden Street, Cambridge, MA 02138, USA
[8] Department of Physics and Astronomy, University of Wyoming, Laramie, WY 82071, USA
[9] Department of Astronomy, The Ohio State University, 140 West 18th Avenue, Columbus, OH 43210, USA
[10] Center for Cosmology and Astroparticle Physics (CCAPP), 191 West Woodruff Avenue, Columbus, OH 43210, USA
[11] Department of Astronomy & Astrophysics, University of California, San Diego, 9500 Gilman Drive, La Jolla, CA 92093, USA
[12] Sub-department of Astrophysics, Department of Physics, University of Oxford, Keble Road, Oxford OX1 3RH, UK
[13] Department of Physics and Astronomy, The Johns Hopkins University, Baltimore, MD 21218, USA
[14] INAF—Osservatorio Astrofisico di Arcetri, Largo E. Fermi 5, I-50125, Florence, Italy
[15] Argelander-Institut für Astronomie, Universität Bonn, Auf dem Hügel 71, 53121 Bonn, Germany
[16] European Southern Observatory (ESO), Alonso de Córdova 3107, Casilla 19, Santiago 19001, Chile
[17] European Southern Observatory, Karl-Schwarzschild Straße 2, D-85748 Garching bei München, Germany
[18] Research School of Astronomy and Astrophysics, Australian National University, Canberra, ACT 2611, Australia
[19] IRAP, OMP, UPS, Université de Toulouse, 9 Av. du Colonel Roche, BP 44346, F-31028 Toulouse cedex 4, France
[20] Space Telescope Science Institute, 3700 San Martin Drive, Baltimore, MD 21218, USA
[21] Leibniz-Institut für Astrophysik Potsdam (AIP), An der Sternwarte 16, 14482 Potsdam, Germany
[22] Dept. of Physics, University of Alberta, 4-183 CCIS, Edmonton, Alberta, T6G 2E1, Canada
[23] Department of Astrophysical Sciences, Princeton University, 4 Ivy Lane, Princeton, NJ 08544, USA
[24] Whitman College, 345 Boyer Avenue, Walla Walla, WA 99362, USA
Received 2025 February 7; revised 2025 June 6; accepted 2025 June 11; published 2025 July 25

Abstract

Recent JWST mid-infrared (mid-IR) images, tracing polycyclic aromatic hydrocarbons (PAHs) and dust continuum emission, provide detailed views of the interstellar medium (ISM) in nearby galaxies. Leveraging PHANGS-JWST Cycle 1 and PHANGS-MUSE data, we measure the PAH and dust continuum emission lifetimes of gas clouds across 17 nearby star-forming galaxies by analyzing the relative spatial distributions of mid-IR (7.7–11.3 μm) and Hα emission at various scales. We find that the mid-IR emitting timescale of gas clouds in galactic disks (excluding centers) ranges from 10–30 Myr. After star formation is detected in Hα, mid-IR emission persists for 3–7 Myr during the stellar feedback phase, covering 70%–80% of the Hα emission. This significant overlap is due to intense radiation from star-forming regions, illuminating the surrounding PAHs and dust grains. In most galaxies, the mid-IR time-scale closely matches the molecular cloud lifetime measured with CO. Although mid-IR emission is complex, as influenced by ISM distribution, radiation, and abundances of dust and PAHs, the similarity between the two timescales suggests that once gas clouds form with compact mid-IR emission, they quickly provide sufficient shielding for stable CO formation. This is likely due to our focus on molecular gas-rich regions of galaxies with near-solar metallicity. Finally, we find that the mid-IR emitting timescale is longer in galaxies with well-defined H II regions and less structured backgrounds, allowing photons to more efficiently heat the ambient ISM surrounding the H II regions, rather than contributing to diffuse emission. This suggests that the shape of the ISM also influences mid-IR emission.

Unified Astronomy Thesaurus concepts: Interstellar clouds (834); Interstellar medium (847); Extragalactic astronomy (506); Disk galaxies (391); Star formation (1569)

[25] NASA Hubble Fellow.
[26] https://coolresearch.io
[27] Kavli Postdoctoral Fellow.
[28] ARC DECRA Fellow.

1. Introduction

Star formation begins in the diffuse interstellar medium (ISM), where giant molecular clouds (GMCs) assemble. When these clouds collapse and form stars, young stars feed back energy and matter to their surroundings, creating H II regions and exploding as supernovae, revealing young stars within their parental clouds (R. S. Klessen & S. C. O. Glover 2016;

M. Chevance et al. 2023). Together, these processes drive the baryon cycle (J. Tumlinson et al. 2017; E. Schinnerer & A. K. Leroy 2024). On a galactic scale, observations have shown a tight correlation between molecular gas and star formation rate (SFR) surface densities, well-known as the "star formation relation" (J. Silk 1997; R. C. J. Kennicutt 1998; F. Bigiel et al. 2008; A. K. Leroy et al. 2013). However, high-resolution observations at scales of $\lesssim$500 pc illustrate a spatial decorrelation between molecular clouds and young stellar regions, often traced using CO and Hα (B. G. Elmegreen 2000; G. Engargiola et al. 2003; L. Blitz et al. 2007; F. Bigiel et al. 2008; A. Kawamura et al. 2009; S. Onodera et al. 2010; A. Schruba et al. 2010; R. E. Miura et al. 2012; S. E. Meidt et al. 2015; E. Corbelli et al. 2017; A. K. Leroy et al. 2017; A. Hirota et al. 2018; K. Kreckel et al. 2018; J. M. D. Kruijssen et al. 2019b; E. Schinnerer et al. 2019; A. T. Barnes et al. 2020; H.-A. Pan et al. 2022).

The spatial decorrelation observed between CO and Hα emission causes the global star formation relation to break down at scales of $\lesssim$500 pc and is a direct consequence of the gas and young stellar phases representing different stages in the lifespan of GMCs (A. Schruba et al. 2010; R. Feldmann et al. 2011; J. M. D. Kruijssen & S. N. Longmore 2014). Various studies have utilized the high-resolution ($\sim$10–200 pc) spatial distributions of CO and Hα flux to infer timescales associated with the evolution of GMCs (E. Corbelli et al. 2017; K. Grasha et al. 2018, 2019; J. M. D. Kruijssen et al. 2019b; M. Chevance et al. 2020a, 2020b, 2022; N. Zabel et al. 2020; J. Kim et al. 2022; J. A. Turner et al. 2022). These studies conclude that GMCs typically survive for about 10–30 Myr before being rapidly dispersed by stellar feedback within 1–5 Myr after massive star formation is detected in Hα. In simulations, the observed small-scale spatial offset is used as a diagnostic tool to test (Y. Fujimoto et al. 2019; S. M. R. Jeffreson et al. 2021; V. A. Semenov et al. 2021) and inform (B. W. Keller et al. 2022) subgrid physics for stellar feedback, as well as the assumptions regarding gas and SFR tracers commonly adopted in observations (Z. Hu et al. 2024).

J. M. D. Kruijssen & S. N. Longmore (2014) and J. M. D. Kruijssen et al. (2018) developed a rigorous method that translates the relative distributions of cold gas and SFR tracer emission into their underlying timescales. Initial applications to small samples of galaxies indicated that GMCs undergo vigorous, feedback-driven lifecycles (J. M. D. Kruijssen et al. 2019b; M. Chevance et al. 2020a, 2022; J. L. Ward et al. 2020, 2022; N. Zabel et al. 2020; J. Kim et al. 2021, 2023; A. Lu et al. 2022), and these findings have contributed to a comprehensive understanding of the necessary conditions for extending these analyses to larger, more systematic galaxy surveys. By applying this method to cloud-scale CO and narrowband Hα observations from PHANGS (A. K. Leroy et al. 2021a; A. Razza et al 2025, in preparation), J. Kim et al. (2022) systematically measured the evolutionary sequence of GMCs, from inert molecular gas phase to H II regions, across 54 main-sequence galaxies. The GMC lifetime varies from 5–30 Myr with an average and 1σ range of 16 $\pm$ 6 Myr, which is 1–3 times the GMC turbulence crossing timescale. The CO and Hα emission overlaps for 1–5 Myr, with an average and 1σ range of 3.2 $\pm$ 1.1 Myr. These intervals greatly exceed the uncertainties and thus represent physical variation. The CO emission is dispersed before the first supernova (SN) explodes, which typically takes place 4–20 Myr after massive star formation (M. Chevance et al. 2022). Even when the deeply embedded star-forming phase (missed in Hα) is considered with emission from dust in thermal equilibrium with very intense radiation fields using Spitzer 24 μm, the feedback timescale is still short, as this phase typically lasts <4 Myr (J. Kim et al. 2021, 2023; L. Ramambason et al. 2025, in preparation; with JWST 21 μm). The short overlapping phase indicates that the pre-SN feedback, such as the photoionization and stellar winds of massive stars, is important for molecular cloud dispersal. Supernovae then explode in a pre-processed environment and deposit their energy into the diffuse ISM, potentially contributing to large-scale turbulence (W. E. Lucas et al. 2020), as evidenced by the lack of supernova remnants associated with dense molecular gas (N. Mayker Chen et al. 2023, 2024).

The large sample of 54 main-sequence galaxies, together with Local Group galaxies from J. Kim et al. (2021), allowed J. Kim et al. (2022) to identify quantitative links between small-scale GMCs and large-scale host galaxy properties. In particular, GMC lifetime increases with increasing stellar mass, which can be explained by two physical arguments, where (1) a large fraction of molecular gas in low-mass and low-metallicity environment is not detected in CO emission, being CO-dark, resulting in apparently short-lived clouds, or (2) high-mass galaxies have a higher midplane pressure, creating conditions for longer-lived GMCs. To distinguish how much this trend is affected by the presence of CO-dark gas, high-resolution tracers of cold gas that are independent of their ability to emit in CO are crucially needed.

The main limitation in extending this GMC timeline to represent the multiphase picture of star formation, including the gas cloud phase dark in CO, has been the lack of cloud-scale observations tracing atomic and molecular gas dark in CO emission. While H I is the ideal tracer for the neutral ISM, existing H I observations by the Karl G. Jansky Very Large Array and MeerKAT have a physical resolution of $\sim$1 kpc (I.-D. Chiang et al. 2024; C. Eibensteiner et al. 2024), which is not sufficient to resolve the spatial offset between clouds and star-forming regions required for robust timescale measurements (J. M. D. Kruijssen et al. 2018). So far, such high-resolution observations have been limited to the Local Group galaxies. J. L. Ward et al. (2020, 2022) showed that in the Large Magellanic Cloud (LMC), the H I cloud lifetime is 48^{+13}_{-8} Myr and is driven by the gravitational collapse of the midplane ISM. In contrast, the measured GMC lifetime in the LMC is much shorter ($11.8^{+2.7}_{-2.2}$ Myr) and is similar to the GMC freefall timescale. The significant difference between the atomic gas and molecular gas cloud lifetimes indicates that GMCs are decoupled from the effects of galactic dynamics and have lifetimes set by internal processes. However, this was based on one galaxy, the LMC, and may be specific to its unique environment such as its low mass, low metallicity, and lack of strong spiral arms.

JWST imaging in the mid-infrared (mid-IR; λ = 7.7–21 μm) is transforming our understanding of the ISM, uncovering a detailed network of filamentary structures that are widespread within galactic disks (J. C. Lee et al. 2023; K. M. Sandstrom et al. 2023a; D. A. Thilker et al. 2023; T. G. Williams et al. 2024). The mid-IR emission, in particular at 7.7, 10, and 11.3 μm, originates from small dust grains and/

or polycyclic aromatic hydrocarbons (PAHs) that are excited by ultraviolet and optical radiation fields (B. T. Draine & A. Li 2007; F. Galliano et al. 2018; T. S. Y. Lai et al. 2020). R. Chown et al. (2025) have characterized the relation between CO and PAH emission across the full PHANGS-JWST Cycle 1 and 2 surveys. CO exhibits a strong and approximately linear relation with PAH emission at ∼100 pc scales. The scaling relationships between CO and PAH emission are similar in both H II and non–H II regions, but they exhibit a dependence on specific SFRs. K. M. Sandstrom et al. (2023a) used PAH emission to probe the ISM in the H I–dominated regime with a gas surface density below $\sim 7\,M_{\odot}\,\mathrm{pc}^{-2}$.

Using the first four PHANGS-JWST galaxies (J. C. Lee et al. 2023), A. K. Leroy et al. (2023) investigated correlations among mid-IR, CO, and Hα emission at ∼100 pc scale. Empirically, the mid-IR emission correlates strongly with both molecular gas and SFR, traced by CO and Hα emission, respectively. The CO and Hα relations with mid-IR are tighter with steeper slopes compared to the correlation between CO and Hα emission. A. K. Leroy et al. (2023) also demonstrated that mid-IR emission can be described as a linear combination of scaled CO and Hα fluxes. Across PHANGS-JWST Cycle 1 galaxies (T. G. Williams et al. 2024), D. Pathak et al. (2024) measured that, on average, 30% of the flux at 7.7–11.3 μm can be attributed to mid-IR emission powered by young massive stars and tend to be associated with a high mid-IR intensity. At lower intensities, mid-IR emission originates from relatively diffuse ISM (mostly molecular), which contributes 60%–70% of the total mid-IR flux.

These studies suggest that mid-IR (or PAH) emission traces multiple gas phases. Away from H II regions, where the diffuse interstellar radiation field dominates heating, mid-IR emission primarily traces the distribution of the neutral ISM, assuming that dust grains and PAHs are well mixed with the neutral gas phases (R. Chown et al. 2021; Y. Gao et al. 2022; B. S. Hensley & B. T. Draine 2023; K. M. Sandstrom et al. 2023a). In contrast, near H II regions, mid-IR emission is powered by radiation from young stars. The PAH emission is also sensitive to PAH abundances. For instance, PAH emission at 7.7 and 11.3 μm is typically suppressed in H II regions relative to the hot dust continuum at 21 μm, due to a lower PAH abundance in the ionized gas compared to the neutral ISM (K. D. Gordon et al. 2008; J. Chastenet et al. 2019, 2023; O. V. Egorov et al. 2023; J. Sutter et al. 2024).

The mid-IR emission from JWST offers a new, exciting, high-resolution, and high-sensitivity view of the gas distribution for galaxies outside the Local Group. In this work, we leverage PHANGS-JWST Cycle 1 observations to measure mid-IR emitting timescales, which is an extension of previous studies on GMC lifetimes. We capitalize on mid-IR observations in F770W, F1000W, and F1130W (7.7, 10, and 11.3 μm, respectively). While F770W and F1130W are regarded as more direct tracers of PAHs, we also include F1000W in our analysis because previous studies have indicated similarities between F1000W and both F770W and F1130W (A. K. Leroy et al. 2023; D. Pathak et al. 2024). The JWST observations allow us to characterize mid-IR (or PAH) emitting timescales during the star formation lifecycle and relate this to the successive phases of gas that participates in the star formation process, from neutral gas reservoir (from JWST) to compact molecular gas (from the Atacama Large Millimeter/submillimeter Array, ALMA) and finally to ionized H II regions (from the Multi Unit Spectroscopic Explorer, MUSE, Hα) that are free of cold gas.

The outline of the paper is as follows. In Section 2, we provide an overview of the observational data used in our analysis. In Section 3, we summarize the method and describe relevant input parameters. In Section 4, we present our measurements of the evolutionary lifecycle of neutral gas clouds and other derived physical quantities. In Section 5, we examine correlations between our measurements and galactic-scale properties. Finally, we summarize and conclude in Section 6.

2. Observational Data

The PHANGS-JWST Cycle 1 Treasury program (GO 2107, PI Lee; J. C. Lee et al. 2023; T. G. Williams et al. 2024) has constructed near- and mid-IR observations of 19 nearby star-forming galaxies. In this work, we focus on PHANGS-JWST Cycle 1 galaxies with GMC evolutionary timescale measurements from J. Kim et al. (2022). This excludes IC 5332 as the number of CO emission peaks was not enough to statistically sample clouds in various stages of the evolutionary sequence (see Appendix B). We further remove NGC 7496, as the resolution was not sufficient to resolve the spatial offset between mid-IR emission and star-forming regions for a robust timescale measurement. As a result, our sample is composed of 17 galaxies in total. Table 1 lists the physical and observational properties of these galaxies. As an example, Figure 1 shows three-color composite images of NGC 0628 made using JWST bands, CO, and Hα observations. We also show locations of identified mid-IR, CO, and Hα emission peaks used in our analysis (see Section 3). Three-color images and associated emission peaks of the full sample can be found in Appendix A.

2.1. Mid-IR bands

We use mid-IR emission at 7.7, 10, and 11.3 μm observed with F770W, F1000W, and F1130W filters on MIRI on board JWST.[29] The observations are obtained from the Mikulski Archive for Space Telescope at the Space Telescope Science Institute.[30] For comprehensive explanations of the survey and the data reduction process, we refer readers to J. C. Lee et al. (2023) and T. G. Williams et al. (2024). The F770W and F1130W filters capture strong emission from PAHs, while F1000W is expected to be dominated by dust continuum (C. M. Whitcomb et al. 2023) with its behavior similar to the PAH bands (A. K. Leroy et al. 2023).

These mid-IR bands are known to best correlate with the cold gas (R. Chown et al. 2021, 2025; Y. Gao et al. 2022; A. K. Leroy et al. 2023; C. M. Whitcomb et al. 2023) and currently provide the highest-resolution and highest-sensitivity view of the neutral gas distribution of the PHANGS-JWST galaxies. This makes them a valuable tool for tracing gas distribution that is missed in PHANGS-ALMA CO observations (A. K. Leroy et al. 2021a), which includes atomic gas,

[29] F770W band includes contributions from stellar continuum, especially the galaxy centers. Using the stellar continuum-subtracted F770W map from R. Chown et al. (2025) and J. Sutter et al. (2024), we confirm that the change in our results is negligible, mostly due to galaxy centers being excluded in our analysis.

[30] Data can be accessed via https://archive.stsci.edu/hlsp/phangs or T. Williams et al. (2023).

Table 1
Summary of Physical and Observed Properties

Galaxy	(a) $M_*^{\rm global}$ (log $M_\odot$)	(b) Z	(c) SFR$^{\rm global}$ (log $M_\odot$ yr^{-1})	(d) $M_{\rm HI}^{\rm global}$ (log $M_\odot$)	(e) $M_{\rm H_2}^{\rm global}$ (log $M_\odot$)	(f) $L_{\rm CO}^{\rm global}$ (log K km pc^2 s^{-1})	(g) ΔMS (dex)	(h) $R_{\rm eff}$ (kpc)	(i) Dist. (Mpc)	(j) Incl. (deg)	(k) P.A. (deg)	(l) Hubble T-type
NGC 0628	10.3	8.5	0.2	9.7	9.4	8.4	0.18	3.90	9.84	8.9	20.7	5.2
NGC 1087	9.9	8.4	0.1	9.1	9.2	8.3	0.33	3.23	15.85	42.9	359.1	5.2
NGC 1300	10.6	8.5	0.1	9.4	9.4	8.5	−0.18	6.53	18.99	31.8	278.0	4.0
NGC 1365	11.0	8.5	1.2	9.9	10.3	9.5	0.72	2.78	19.57	55.4	201.1	3.2
NGC 1385	10.0	8.4	0.3	9.2	9.2	8.4	0.50	3.37	17.22	44.0	181.3	5.9
NGC 1433	10.9	8.6	0.1	9.4	9.3	8.5	−0.36	4.30	18.63	28.6	199.7	1.5
NGC 1512	10.7	8.6	0.1	9.9	9.1	8.3	−0.21	4.76	18.83	42.5	261.9	1.2
NGC 1566	10.8	8.6	0.7	9.8	9.7	8.9	0.29	3.17	17.69	29.5	214.7	4.0
NGC 1672	10.7	8.6	0.9	10.2	9.9	9.1	0.56	3.39	19.4	42.6	134.3	3.3
NGC 2835	10.0	8.4	0.1	9.5	8.8	7.7	0.26	3.30	12.22	41.3	1.0	5.0
NGC 3351	10.4	8.6	0.1	8.9	9.1	8.2	0.05	3.04	9.96	45.1	193.2	3.1
NGC 3627	10.8	8.6	0.6	9.1	9.8	9.0	0.19	3.64	11.32	57.3	173.1	3.1
NGC 4254	10.4	8.6	0.5	9.5	9.9	8.9	0.37	2.41	13.1	34.4	68.1	5.2
NGC 4303	10.5	8.6	0.7	9.7	9.9	9.0	0.54	3.43	16.99	23.5	312.4	4.0
NGC 4321	10.7	8.6	0.6	9.4	9.9	9.0	0.21	5.50	15.21	38.5	156.2	4.0
NGC 4535	10.5	8.6	0.3	9.6	9.6	8.6	0.14	6.26	15.77	44.7	179.7	5.0
NGC 5068	9.4	8.3	−0.6	8.8	8.4	7.3	0.02	1.97	5.2	35.7	342.4	6.0

Note. (a), (c), (e), and (f)—Global stellar mass, SFR, molecular gas mass, and integrated CO luminosity from PHANGS-ALMA (A. K. Leroy et al. 2019, 2021a). (b)—Molecular gas mass-weighted average of gas phase metallicity [12+log(O/H)] from K. Kreckel et al. (2019) and T. G. Williams et al. (2022). (d)—Literature H I mass adopted from Hyper-LEDA (D. Makarov et al. 2014). (g) and (h)—Offset from the star-forming main sequence and effective radius from A. K. Leroy et al. (2021a). (i), (j), and (k)—Distance from G. S. Anand et al. (2021) and inclination and position angle from P. Lang et al. (2020). (l)—Hubble type from LEDA (G. Paturel et al. 1997).

CO-dark molecular gas or CO-bright molecular gas below the detection threshold.

However, the physical origin of these emissions is complex, as they are influenced by various factors like gas column density, heating, dust, and PAH abundances. We do not include the dust continuum at 21 μm (F2100W) in our analysis, as it includes emission from dust in thermal equilibrium with very high radiation fields and therefore is more associated with star-forming regions than cold gas (B. T. Draine et al. 2007; R. C. Kennicutt & N. J. Evans 2012; A. K. Leroy et al. 2013; F. Belfiore et al. 2023; O. V. Egorov et al. 2023; H. Hassani et al. 2023; A. K. Leroy et al. 2023; C. M. Whitcomb et al. 2023; D. Pathak et al. 2024). Indeed, this longer wavelength has been successfully used to trace the embedded star-forming period with Spitzer 24 μm observations (J. Kim et al. 2021) and with JWST F2100W (J. Kim et al. 2023; L. Ramambason et al. 2025, in preparation). The resolutions of F770W, F1000W, and F1130W are 0.″24, 0.″31, and 0.″36, respectively, which roughly translate into a physical resolution of 5–35 pc across the range of distances of our galaxy sample (5–20 Mpc).

2.2. MUSE Hα

As an SFR tracer, we use Hα observations from the PHANGS-MUSE survey (E. Emsellem et al. 2022). The full spectral fitting to MUSE observations allows us to properly measure Hα emission without contamination from the [N II] line. This is different from the SFR tracer maps adopted in J. Kim et al. (2022), which were narrowband Hα observations taken with the du Pont 2.5 m telescope at the Las Campanas Observatory and the Wide Field Imager instrument at the MPG-ESO 2.2 m telescope at the La Silla Observatory. We confirm that the results are consistent within error bars when the narrowband Hα observations are used. Detailed explanations of the PHANGS-MUSE survey and data reduction can be found in E. Emsellem et al. (2022). In brief, the observations have mapped spectra of 19 nearby star-forming galaxies with the MUSE integral field spectrograph on the ESO/Very Large Telescope (VLT), where the sample overlaps with PHANGS-JWST Cycle 1. From data cubes with homogenized point-spread functions (PSFs; "copt" version), we use Hα line maps obtained by a Gaussian fit to the Hα line, accounting for the stellar continuum and Balmer line absorption. The resolution ranges 0.″6 − 1.″3, which corresponds to 50–150 pc in physical scale for our galaxy sample. The typical 3σ Hα flux sensitivity is 4–7 $\times$ 10^{37} erg s^{-1} kpc^{-2} (E. Emsellem et al. 2022).

We note that to be consistent with our analysis in J. Kim et al. (2022), we do not use Hα maps that have been corrected for the dust extinction using the Balmer decrement (F. Belfiore et al. 2022). In order to assess the impact of extinction correction, we used Balmer decrement-corrected Hα observations for one of the nearest galaxies, NGC 0628 from F. Belfiore et al. (2023), and find that the changes in our derived timescale are within the 1σ uncertainties. However, we observe a slightly smaller average separation between independent star-forming regions after applying the extinction correction (52^{+8}_{-8} pc) compared to the value of 67^{+7}_{-8} pc reported in Section 4.4. The extinction correction would only have a significant effect if the decrement varied considerably within individual H II regions, which is unlikely since these regions are typically not well resolved.

2.3. Post-processing Images

To proceed with our analysis (see Section 3), we apply additional procedures to the data. We first convolve finer-resolution JWST observations to match the coarser resolution of the Hα observations, where Table 2 lists the matched

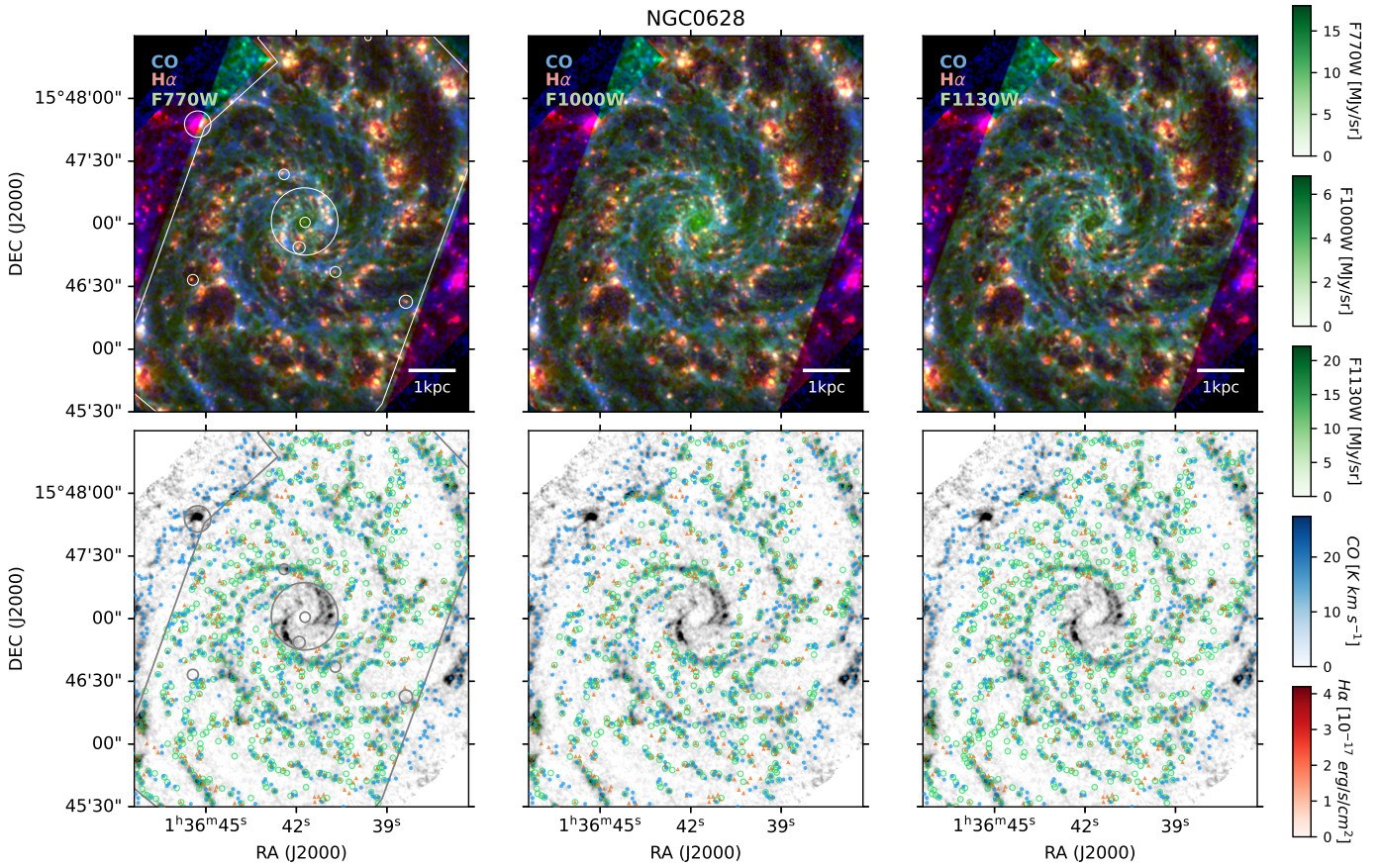

Figure 1. Top panels: composite three-color images created using CO (blue), Hα (red), and mid-IR (green) observations, where each panel from left to right uses mid-IR emission of F770W, F1000W, and F1130W, respectively. The mid-IR observations have been convolved and regridded to match the coarser resolution and pixel grid of Hα observations (see Section 2.3). For visualization purposes, a power-law brightness scale with gamma correction ($\gamma = 2$) has been applied in the top panels. The color bars on the right reflect the true flux ranges in each observation. The left panel shows the area included in our analysis as a polygon. Crowded galaxy center (ellipse in the center), as well as artifacts and extremely bright peaks (circles) are excluded. Bottom panels: locations of identified Hα (orange triangles), CO (blue filled circles), and mid-IR (green open circles) emission peaks (see Section 3) are overlaid on the CO map, which is shown in grayscale with a linear brightness scale. Again, from left to right, the mid-IR emission peaks correspond to peaks identified in F770W, F1000W, and F1130W maps, respectively. The CO grayscale image uses the same intensity range as the CO emission in the top panels shown in blue, with a range of flux indicated in the color bar on the right.

resolution ($l_{\rm ap,min}$). We then regrid these convolved maps to align with the pixel grid of the Hα maps. During the convolution, we use a kernel that transforms the JWST PSF to a circular Gaussian PSF, generated following G. Aniano et al. (2011).

As described in Section 3, our timescale measurements are based on gas-to-SFR tracer flux ratios. Therefore, exceedingly bright regions that are not likely to represent the overall cloud (or H II region) population but constitute a significant fraction in the total emission have the potential to bias our measurements (e.g., 30 Doradus in the LMC by J. L. Ward et al. 2022). Accordingly, in our previous analysis of the same galaxies using CO as a tracer for the molecular gas (J. Kim et al. 2022), we masked such bright regions (defined below) detected in CO and Hα emission. Most of the galactic centers that appeared crowded were also masked because they complicate the identification of star-forming regions and gas clouds within the environment.

In this work, to be consistent with previous studies, we use the same masks as J. Kim et al. (2022) and apply additional masks if extremely bright regions are present in mid-IR observations. We adopt the same criteria for detecting exceedingly bright regions as in J. Kim et al. (2022), which uses luminosity functions of the identified emission peaks (see Section 3). Specifically, we first sort the identified peaks in descending order of luminosity. Then, starting from the top, we search for gaps in the distribution, defined as a peak being at least twice as luminous as the next-brightest peak. Whenever such a gap is identified, we mask all peaks that surpass the brightness of the next-brightest peak. We check for extremely bright peaks in all three mid-IR bands and mask them in all of our analyses, even if the criterion is met in only one of the bands. As a result, we apply additional masking to bright peaks in several galaxies (NGC 1087, 1300, 1365, 1672, and 2835), with up to five extra peaks masked per galaxy. Appendix C shows that masking bright regions has a negligible impact on the derived properties, with results consistent within the 1σ uncertainty. Lastly, we limit our analysis to areas where both JWST and MUSE observations overlap (polygon in Figure 1). The analyzed region is similar to J. Kim et al. (2022), which was defined using ALMA and narrowband Hα observations.

3. Method

We characterize evolutionary timescales from mid-IR emitting gas phase to H II regions by applying a robust statistical method (J. M. D. Kruijssen & S. N. Longmore 2014; J. M. D. Kruijssen et al. 2018) to mid-IR and Hα observations.

Table 2
Main Input Parameters Adopted in Our Analysis

Galaxy	$r_{\rm min}$ (kpc)	$l_{\rm ap,min}$ (pc)	$l_{\rm ap,max}$ (pc)	$N_{\rm pix,min}$	$t_{\rm ref}$ (Myr)	$\Delta\log_{10}\mathcal{F}$, $\delta\log_{10}\mathcal{F}$, n_λ[a]										
						Hα			F770W			F1000W			F1130W	
NGC 0628	0.1	44	3000	50	$7.45^{+0.62}_{-0.64}$	2.8	0.05	2.4	0.05	13	2.4	0.05	13	2.4	0.05	13
NGC 1087	0.1	83	3000	40	$8.20^{+2.27}_{-1.37}$	3.2	0.05	2.5	0.05	14	2.5	0.05	14	2.5	0.05	14
NGC 1300	0.1	89	3000	15	$7.80^{+0.70}_{-0.88}$	2.8	0.05	2.5	0.05	13	2.5	0.05	13	2.5	0.05	13
NGC 1365	0.2	145	3000	10	$8.15^{+1.20}_{-1.09}$	3.5	0.05	1.7	0.05	15	1.7	0.05	15	1.7	0.05	15
NGC 1385	0.1	76	3000	20	$6.92^{+1.56}_{-0.92}$	3.0	0.05	2.2	0.05	14	2.2	0.05	14	2.2	0.05	14
NGC 1433	0.1	88	3000	30	$6.35^{+0.51}_{-0.50}$	2.0	0.05	1.9	0.10	13	1.9	0.10	13	1.9	0.10	13
NGC 1512	0.1	133	3000	20	$6.02^{+0.31}_{-0.51}$	2.0	0.03	1.8	0.03	11	1.8	0.03	14	1.8	0.03	14
NGC 1566	0.1	74	2000	20	$8.96^{+1.21}_{-1.07}$	2.6	0.07	2.8	0.07	14	2.8	0.07	14	2.8	0.07	14
NGC 1672	0.2	105	3000	50	$8.74^{+1.49}_{-1.59}$	2.0	0.05	2.0	0.05	13	2.0	0.05	13	2.0	0.05	13
NGC 2835	0.1	79	3000	20	$5.59^{+0.57}_{-0.47}$	3.0	0.05	2.2	0.05	14	2.2	0.05	11	2.2	0.05	13
NGC 3351	0.1	60	3000	20	$6.78^{+0.98}_{-0.66}$	2.0	0.05	2.8	0.05	13	2.8	0.05	13	2.8	0.05	13
NGC 3627	0.1	78	3000	30	<7.00[b]	3.1	0.05	3.2	0.05	13	3.2	0.05	13	3.2	0.05	13
NGC 4254	0.1	62	1500	15	$9.01^{+1.31}_{-1.03}$	3.5	0.05	2.5	0.05	13	2.5	0.05	13	2.5	0.05	13
NGC 4303	0.2	67	3000	40	$8.28^{+1.79}_{-1.23}$	2.5	0.05	2.6	0.05	13	2.6	0.05	14	2.6	0.05	13
NGC 4321	0.1	97	3000	10	$7.39^{+0.75}_{-0.68}$	2.2	0.05	2.2	0.05	15	2.2	0.05	15	2.2	0.05	15
NGC 4535	0.1	51	2500	20	$8.87^{+2.26}_{-1.08}$	3.0	0.05	3.0	0.05	12	3.0	0.05	11	3.0	0.05	12
NGC 5068	0.0	29	3000	70	$5.49^{+0.40}_{-0.33}$	3.4	0.05	2.6	0.05	13	2.6	0.05	11	2.6	0.05	13

Notes. For other parameters not listed here, related to error propagation and model fitting, we use the default values from J. M. D. Kruijssen et al. (2018).
[a] For a given galaxy, the same input parameters are used for all of the analysis adopting different mid-IR bands except parameters related to peak identification ($\Delta\log_{10}\mathcal{F}$) and diffuse emission filtering (n_λ), which are listed separately for each mid-IR band.
[b] Only an upper limit was constrained in J. Kim et al. (2022).

In this section, we briefly describe the method (formalized in the HEISENBERG code[31]) and list the main input parameters used. We direct readers to J. M. D. Kruijssen & S. N. Longmore (2014) for an in-depth explanation of the methodological framework and J. M. D. Kruijssen et al. (2018) for a demonstration and validation of the code using simulated galaxies, along with a comprehensive description of its input parameters. Including the galaxies in this paper, this method has been applied to ∼60 observed galaxies to measure GMC evolutionary timescales in diverse environments (stellar mass $M_* = 10^9$–$10^{11}\,M_\odot$; J. M. D. Kruijssen et al. 2019b; M. Chevance et al. 2020a, 2022; D. T. Haydon et al. 2020; A. P. S. Hygate 2020; J. L. Ward et al. 2020, 2022; N. Zabel et al. 2020; J. Kim et al. 2021, 2022, 2023; A. Lu et al. 2022). These studies mostly used CO and Hα as tracers for cold gas and young star-forming regions, respectively.

As first demonstrated by A. Schruba et al. (2010), we quantify the small-scale differences in the flux distributions of cold gas and SFR tracers by measuring the gas-to-SFR tracer flux ratios across various spatial scales, ranging from cloud scales (<100 pc) to global, kiloparsec scale. The small-scale decorrelation between gas and young stars is naturally explained by the transient nature of the cloud lifecycle, during which clouds assemble, form stars, and are subsequently dispersed by stellar feedback, only leaving young stars to be detected without associated cold gas. Therefore, the level of (de-)correlation on small scales compared to the galactic-scale is linked to the evolutionary timescales of clouds. For example, when measuring the gas-to-SFR tracer flux ratio of cold gas peaks on a cloud scale, the deviation from the galactic average value will depend on the flux of SFR tracer peaks included in these small apertures. This information allows us to constrain how long clouds remain inert and the duration required for stellar feedback to disperse them (J. M. D. Kruijssen & S. N. Longmore 2014).

To determine mid-IR-to-Hα flux ratios of emission peaks at various spatial scales, we first identify emission peaks in both mid-IR and Hα maps (at the highest PSF-matched resolution; $l_{\rm ap,min}$) using CLUMPFIND (J. P. Williams et al. 1994). This algorithm detects peaks by contouring the data at multiple flux levels. The contours are spaced apart by a step size of $\delta\log_{10}\mathcal{F}$, covering the entire range of $\Delta\log_{10}\mathcal{F}$ starting from the maximum flux. Peaks containing fewer than $N_{\rm pix,min}$ pixels are disregarded. Table 2 lists adopted values of $\delta\log_{10}\mathcal{F}$ and $\Delta\log_{10}\mathcal{F}$ for different mid-IR wavelengths. A single value for $N_{\rm pix,min}$ is used for each galaxy as the spatial resolutions are matched across wavelengths. As shown in Figure 1 and Appendix A, we have visually verified that all of the obvious emission peaks are identified.

Next, we center apertures of varying sizes, ranging from $l_{\rm ap,min} \approx 100$ pc to $l_{\rm ap,max} \approx 3$ kpc, on each peak of a given type. For each aperture size and peak type, we sum the total enclosed mid-IR and Hα flux across all apertures and compute their ratio. This gives the aperture-averaged mid-IR-to-Hα flux ratio as a function of aperture size. Because we integrate all of the flux within the apertures, our results are not highly sensitive to the specific peak identification parameters.

There could be a case where some apertures will overlap, especially when aperture sizes are big. To avoid double-counting pixels and ensure statistical independence, we generate Monte Carlo realizations of nonoverlapping aperture samples for each peak type and aperture size. For each realization, we randomly draw a subset of peaks such that no apertures overlap. We then compute the total fluxes enclosed within these independent samples and repeat this process 1000 times, following the description in J. M. D. Kruijssen et al. (2018). The final mid-IR-to-Hα flux ratio at a given aperture size is obtained by averaging over all realizations.

[31] https://github.com/mustang-project/Heisenberg

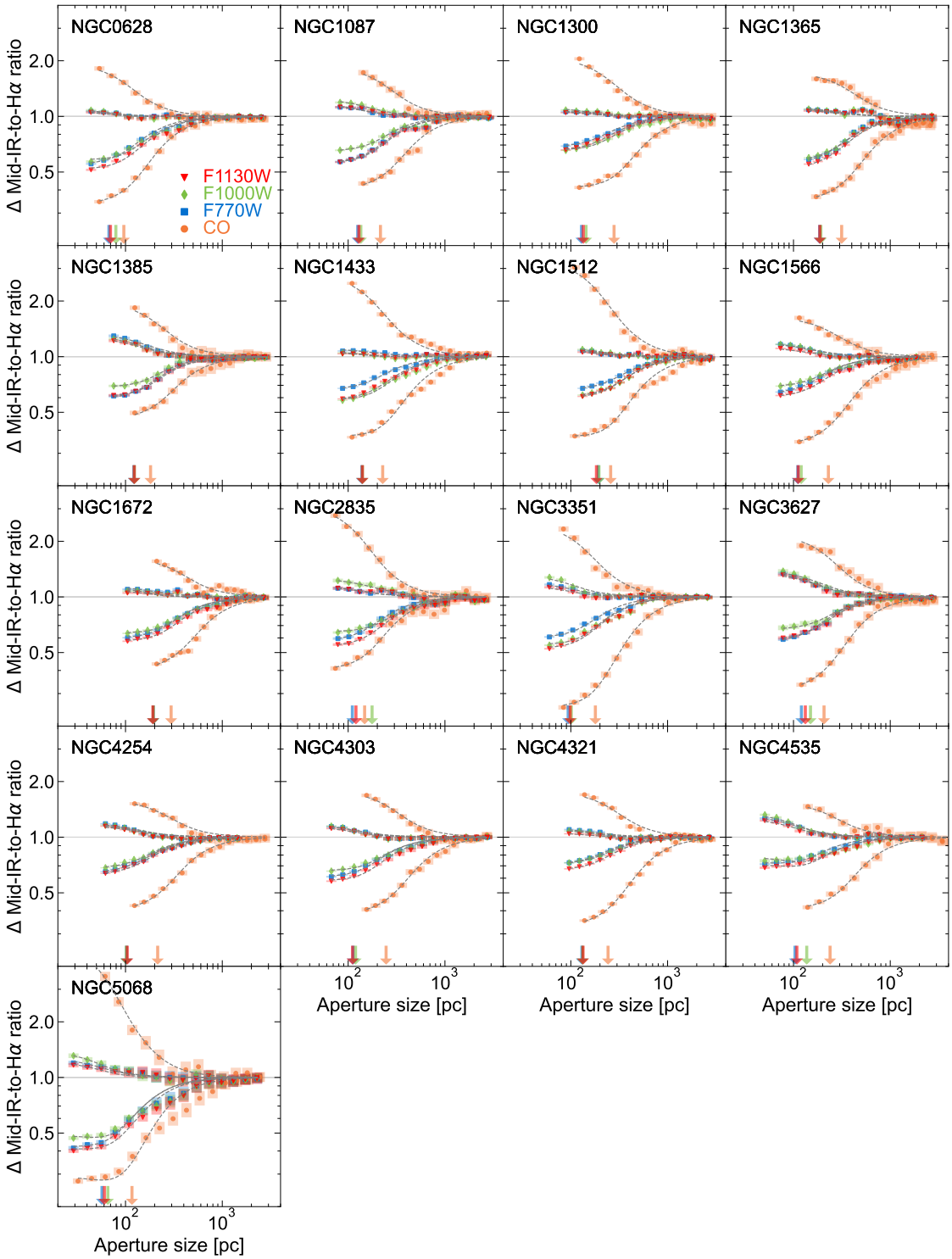

Figure 2. The measured deviations of mid-IR-to-Hα flux ratio compared to the galactic average value are shown as a function of size-scale. The top branch is when the apertures are focused on mid-IR peaks, and the bottom is when the apertures are focused on Hα peaks. The shaded region indicates the effective 1σ error, after the covariance between data points is taken into account. The same measurements but using CO as the gas tracer from J. Kim et al. (2022) are also shown for comparison. We also show the galactic average value, which equals 1 (solid line), as well as our best-fitting model (dashed line) to the measured flux ratios. The arrow indicates our best-fitting λ, with its value listed in Table 3 including other constrained parameters (t_g and t_{fb}).

This ensures that large-scale aperture statistics are not skewed by overlapping regions. Figure 2 shows mid-IR-to-Hα flux ratios normalized by the ratio on large scales as a function of aperture size.

To these observed flux ratios, we fit an analytical function that depends on the relative durations of successive phases in the timeline of cloud evolution (mid-IR bright, Hα bright, and overlap phase), as well as the typical distance between regions undergoing independent evolution (λ). The relative durations are converted into absolute values by using the duration of the Hα-bright phase (t_s) as a reference timescale (t_{ref}), which is measured in J. Kim et al. (2022). The analytical function is

then described by three independent quantities: the mid-IR bright phase (t_g^X), the mid-IR and Hα overlap phase (t_{fb}^X), and the region separation length (λ^X), where we use X to denote the mid-IR wavelength. We refer to the overlap phase, during which mid-IR and Hα emission is found coincident, as the feedback timescale, since it indicates the time for intense radiation from H II regions to illuminate the surrounding PAH and dust and the time for PAHs and/or dust dispersal at the scales of $\sim$100 pc.

Our analytical model assumes that the emission enclosed in an aperture originates solely from regions inside it. Diffuse emission on large spatial scales affects the measured cloud evolutionary timescales by contributing flux that is not physically associated with the compact emission peaks identified in the maps. For instance, substantial diffuse emission in the gas tracer map could lead to an elevated global gas-to-SFR tracer flux ratio compared to that measured locally centered on gas emission peaks (A. P. S. Hygate 2020). More importantly, the diffuse components in mid-IR and Hα maps often have a different physical origin from the compact star-forming structures we aim to trace. For example, large-scale mid-IR emission traces diffuse gas that is not likely to be dense enough to form massive stars (D. Calzetti et al. 2007; K. M. Sandstrom et al. 2023a). One of the major contributions to the diffuse ionized gas is ionizing photons leaking from H II regions that are no longer cospatial with their parent molecular clouds. We therefore filter out large-scale emission to avoid biasing the inferred timescales by emission that does not participate in the evolutionary cycle of compact star-forming regions and clouds we seek to characterize (see also J. M. D. Kruijssen et al. 2018; A. P. S. Hygate et al. 2019; M. Chevance et al. 2020a).

We remove emission on scales larger than n_λ times the region separation length λ using a Gaussian high-pass filter in Fourier space, where n_λ is the scaling factor. We adopt the lowest possible integer value of n_λ for which the flux loss from the compact emission remains $<$10%, as recommended by A. P. S. Hygate et al. (2019). This approach has been shown to achieve a balance between removing diffuse background emission and preserving the structure of compact regions, and has been adopted in all of our previous analyses (J. M. D. Kruijssen et al. 2019b; M. Chevance et al. 2020a; A. P. S. Hygate 2020; J. Kim et al. 2021, 2022, 2023).[32] This procedure is carried out iteratively until the convergence criterion is met, defined as when the change in λ is $<$5% for three consecutive runs.

As a result, we filter out 30%–80% of the flux from mid-IR observations with an average of 60%, which agrees well with the diffuse emission fraction measured in Spitzer 8 μm observations of M33 obtained by separating discrete sources (S. Verley et al. 2009). In Hα emission maps, we remove about 40%–60% of the total emission, with an average of 50%. This is in line with F. Belfiore et al. (2022), who found that the fraction of ionized gas emission located outside the compact H II regions ranges from 20%–60%, with an average of 40% using the same PHANGS-MUSE observations (E. Emsellem et al. 2022). We discuss this further in Section 4.5.

[32] We note that in the case of NGC 1512, where we measure the highest diffuse emission fraction in 7.7 μm, a filtering scale smaller than $n_\lambda \times \lambda = 4$ kpc is required to obtain a higher (lower) mid-IR-to-Hα flux ratio compared to the galactic average value on small scale, when focusing on mid-IR (Hα) peaks. The timescale measurements using $n_\lambda \times \lambda = 4$ kpc and our best-fitting model ($n_\lambda \times \lambda \approx 2$ kpc) are consistent within 1σ error, although the measured diffuse emission fraction at 7.7 μm decreases by 10% due to less emission being filtered out when $n_\lambda \times \lambda = 4$ kpc.

4. Timeline of Cloud Evolution from Mid-IR Emitting Phase to H II Regions

In this section, we present results from applying the method described in Section 3 to mid-IR (F770W, F1000W, and F1130W) and Hα observations across 17 galaxies in our sample.

4.1. Relative Spatial Distribution into Evolutionary Timescales

Figure 2 shows the measured deviation of mid-IR-to-Hα tracer flux ratios compared to the galactic average value at different spatial scales ranging from $\sim$100 pc to 3 kpc. We also show results using CO as the gas tracer for comparison from J. Kim et al. (2022). Our best-fit model is shown as a dashed line, allowing us to derive timescales associated with different phases of the star formation process. In all of our measurements using different gas tracers (CO and three mid-IR bands), we find that the measured flux ratio deviates from the galactic average value on small scales. A higher (lower) mid-IR-to-Hα flux ratio than the galactic average is measured when apertures are placed on mid-IR (Hα) peaks on small scales, resulting in a relative deviation at small scale, higher (lower) than 1, demonstrating a spatial offset between mid-IR and Hα emission. However, we find that the degree of divergence is much more significant when CO is used as the gas tracer compared to when mid-IR bands are used. This indicates that Hα spatially correlates better with compact mid-IR than CO, which is consistent with other empirical studies (R. Chown et al. 2021; Y. Gao et al. 2022; A. K. Leroy et al. 2023; C. M. Whitcomb et al. 2023).

In Table 3, we list our best-fit parameters: the mid-IR emitting phase (t_g; see Section 4.2), the feedback phase (t_{fb}; see Section 4.3), and the average separation length between independent star-forming regions (λ; see Section 4.4). We also present other derived quantities, such as the duration of the mid-IR emitting phase without associated CO and Hα emission (CO-dark mid-IR emitting phase, $t_{CO-dark}^{mid-IR}$; see Section 4.2), the fraction of the mid-IR emitting phase associated with the SFR tracer, the fraction of the SFR tracer emitting phase associated with the mid-IR (t_{fb}/t_g and t_{fb}/t_s; see Section 4.3), the difference in feedback timescales when using mid-IR versus CO ($\Delta t_{fb,CO}$; see Section 4.3), and the diffuse emission fractions measured in mid-IR and SFR tracer maps ($f_{diffuse}^{mid-IR}$ and $f_{diffuse}^{H\alpha}$; see Section 4.5). Figure 3 shows the distributions of these physical quantities, highlighting significant galaxy-to-galaxy variation. A more detailed discussion is provided in the subsequent sections.

Figure 4 shows the multitracer evolutionary timeline of regions transitioning from gas to stars, obtained by combining the mid-IR emitting phase measured in this work with GMC evolutionary timeline from J. Kim et al. (2022). Regions are initially inert and detected only in CO and mid-IR tracing the gaseous cloud phase. Later, Hα becomes visible as the newly formed stars partially emerge from the parental cloud. Finally, the cloud disperses, allowing Hα to be detected alone without associated CO and mid-IR emission. For most galaxies, the mid-IR emitting phase encompasses the CO-emitting phase and continues to be detected after the CO has disappeared, covering a significant fraction of the Hα-emitting phase.

Table 3
Physical Quantities Describing the Cloud Evolution from Mid-IR Emitting Gas Phase to Young Stellar H II Regions

Galaxy	Band (μm)	t_g (Myr)	t_{fb} (Myr)	t_s (Myr)	λ (pc)	$f_{diffuse}^{mid-IR}$ ⋯	$f_{diffuse}^{H\alpha}$ ⋯	t_{fb}/t_g ⋯	t_{fb}/t_s ⋯	$\Delta t_{fb,CO}$ (Myr)	$t_{CO-dark}$ (Myr)
NGC 0628	7.7	$25.7^{+3.4}_{-1.6}$	$6.0^{+1.0}_{-0.7}$	$7.4^{+0.5}_{-0.5}$	67^{+7}_{-8}	$0.60^{+0.03}_{-0.03}$	$0.50^{+0.04}_{-0.03}$	$0.23^{+0.05}_{-0.05}$	$0.80^{+0.16}_{-0.14}$	$2.8^{+1.1}_{-0.9}$	$-1.1^{+2.9}_{-4.2}$
	10	$25.6^{+2.1}_{-3.3}$	$6.8^{+0.5}_{-1.1}$	$7.4^{+0.4}_{-0.6}$	79^{+9}_{-9}	$0.59^{+0.03}_{-0.02}$	$0.45^{+0.04}_{-0.03}$	$0.27^{+0.05}_{-0.06}$	$0.92^{+0.14}_{-0.19}$	$3.7^{+0.7}_{-1.3}$	$-2.1^{+4.1}_{-3.2}$
	11.3	$34.6^{+2.5}_{-4.2}$	$7.2^{+0.3}_{-1.3}$	$7.4^{+0.4}_{-0.5}$	70^{+6}_{-7}	$0.57^{+0.03}_{-0.03}$	$0.47^{+0.04}_{-0.03}$	$0.21^{+0.04}_{-0.05}$	$0.97^{+0.13}_{-0.21}$	$4.1^{+0.6}_{-1.4}$	$6.5^{+4.8}_{-3.5}$
NGC 1087	7.7	$21.5^{+2.3}_{-3.4}$	$6.6^{+1.1}_{-1.1}$	$8.2^{+0.7}_{-1.3}$	125^{+23}_{-17}	$0.66^{+0.03}_{-0.02}$	$0.61^{+0.03}_{-0.03}$	$0.31^{+0.09}_{-0.08}$	$0.80^{+0.22}_{-0.19}$	$2.7^{+1.7}_{-2.5}$	$-0.9^{+7.1}_{-4.3}$
	10	$16.4^{+1.7}_{-3.2}$	$5.9^{+1.1}_{-1.0}$	$8.2^{+0.9}_{-1.4}$	135^{+36}_{-19}	$0.67^{+0.02}_{-0.03}$	$0.59^{+0.03}_{-0.04}$	$0.36^{+0.12}_{-0.10}$	$0.73^{+0.23}_{-0.21}$	$2.1^{+1.7}_{-2.5}$	$-5.4^{+7.0}_{-4.0}$
	11.3	$22.4^{+1.9}_{-3.8}$	$6.5^{+1.0}_{-1.1}$	$8.2^{+0.6}_{-1.3}$	129^{+21}_{-14}	$0.67^{+0.03}_{-0.03}$	$0.61^{+0.03}_{-0.03}$	$0.29^{+0.08}_{-0.07}$	$0.79^{+0.21}_{-0.19}$	$2.6^{+1.7}_{-2.5}$	$0.2^{+7.3}_{-4.1}$
NGC 1300	7.7	$19.7^{+1.8}_{-1.7}$	<7.4	<8.3	<150	$0.66^{+0.04}_{-0.02}$	$0.54^{+0.04}_{-0.03}$	<0.41	⋯	<4.2	-2.5 - 8.4
	10	$22.3^{+2.2}_{-1.7}$	$6.5^{+0.9}_{-0.8}$	$7.8^{+0.5}_{-0.6}$	144^{+16}_{-16}	$0.63^{+0.03}_{-0.02}$	$0.51^{+0.04}_{-0.02}$	$0.29^{+0.06}_{-0.06}$	$0.83^{+0.16}_{-0.15}$	$2.9^{+1.2}_{-1.1}$	$2.8^{+2.5}_{-3.3}$
	11.3	$21.3^{+2.2}_{-1.6}$	$6.6^{+0.9}_{-0.7}$	$7.8^{+0.5}_{-0.6}$	135^{+17}_{-19}	$0.66^{+0.03}_{-0.02}$	$0.53^{+0.04}_{-0.02}$	$0.31^{+0.06}_{-0.06}$	$0.85^{+0.16}_{-0.15}$	$3.1^{+1.2}_{-1.0}$	$1.6^{+2.5}_{-3.3}$
NGC 1365	7.7	$18.2^{+4.1}_{-2.7}$	<6.9	<9.0	<237	$0.79^{+0.03}_{-0.03}$	$0.65^{+0.04}_{-0.04}$	<0.45	⋯	<3.4	-8.8 - 4.9
	10	$19.3^{+4.0}_{-2.5}$	<6.9	<9.0	<234	$0.81^{+0.02}_{-0.02}$	$0.64^{+0.03}_{-0.03}$	<0.41	⋯	<3.4	-7.4 - 5.9
	11.3	$21.4^{+4.6}_{-2.5}$	<7.1	<8.9	<225	$0.80^{+0.02}_{-0.02}$	$0.64^{+0.03}_{-0.03}$	<0.38	⋯	<3.6	-5.6 - 8.6
NGC 1385	7.7	$11.3^{+1.9}_{-1.5}$	$4.2^{+0.7}_{-0.8}$	$6.9^{+1.1}_{-0.9}$	122^{+34}_{-27}	$0.61^{+0.05}_{-0.05}$	$0.58^{+0.07}_{-0.06}$	$0.37^{+0.10}_{-0.12}$	$0.61^{+0.17}_{-0.19}$	$1.6^{+1.1}_{-1.7}$	$-3.7^{+5.3}_{-3.2}$
	10	$11.0^{+1.5}_{-1.7}$	$4.4^{+1.2}_{-1.1}$	$6.9^{+0.9}_{-1.0}$	124^{+37}_{-23}	$0.58^{+0.07}_{-0.09}$	$0.57^{+0.09}_{-0.09}$	$0.40^{+0.16}_{-0.14}$	$0.63^{+0.25}_{-0.23}$	$1.7^{+1.5}_{-1.8}$	$-4.2^{+5.3}_{-3.0}$
	11.3	$13.6^{+1.9}_{-1.7}$	$4.5^{+1.2}_{-0.9}$	$6.9^{+0.8}_{-0.9}$	123^{+22}_{-16}	$0.62^{+0.05}_{-0.05}$	$0.58^{+0.06}_{-0.06}$	$0.33^{+0.12}_{-0.11}$	$0.65^{+0.23}_{-0.20}$	$1.9^{+1.5}_{-1.8}$	$-1.8^{+5.3}_{-3.2}$
NGC 1433	7.7	$12.0^{+1.4}_{-1.3}$	$4.8^{+0.6}_{-0.5}$	$6.3^{+0.4}_{-0.5}$	139^{+35}_{-26}	$0.76^{+0.02}_{-0.02}$	$0.52^{+0.03}_{-0.02}$	$0.40^{+0.08}_{-0.08}$	$0.76^{+0.14}_{-0.12}$	$2.7^{+0.7}_{-0.6}$	$-5.3^{+2.1}_{-2.2}$
	10	$21.7^{+1.2}_{-2.7}$	$6.2^{+0.2}_{-1.0}$	$6.3^{+0.3}_{-0.4}$	141^{+19}_{-16}	$0.61^{+0.03}_{-0.02}$	$0.52^{+0.03}_{-0.02}$	$0.28^{+0.05}_{-0.06}$	$0.97^{+0.11}_{-0.19}$	$4.0^{+0.5}_{-1.1}$	$3.1^{+3.1}_{-2.1}$
	11.3	$19.1^{+1.5}_{-1.6}$	$5.8^{+0.4}_{-0.8}$	$6.3^{+0.3}_{-0.4}$	140^{+13}_{-18}	$0.71^{+0.02}_{-0.01}$	$0.51^{+0.02}_{-0.01}$	$0.31^{+0.05}_{-0.06}$	$0.92^{+0.12}_{-0.16}$	$3.7^{+0.6}_{-0.9}$	$0.8^{+2.3}_{-2.3}$
NGC 1512	7.7	$11.7^{+1.8}_{-1.2}$	<5.5	<6.4	<238	$0.79^{+0.02}_{-0.02}$	$0.56^{+0.03}_{-0.03}$	<0.52	⋯	<3.8	-5.1 - 3.3
	10	$14.8^{+1.7}_{-1.3}$	<5.4	<6.3	<225	$0.71^{+0.02}_{-0.02}$	$0.53^{+0.03}_{-0.02}$	<0.40	⋯	<3.8	-2.2 - 6.3
	11.3	$16.9^{+1.2}_{-2.2}$	<5.8	<6.3	<209	$0.74^{+0.02}_{-0.02}$	$0.54^{+0.03}_{-0.02}$	<0.40	⋯	<4.3	-1.3 - 8.0
NGC 1566	7.7	$17.5^{+2.3}_{-1.7}$	$6.0^{+0.9}_{-0.7}$	$9.0^{+0.9}_{-0.9}$	111^{+22}_{-16}	$0.62^{+0.03}_{-0.03}$	$0.56^{+0.03}_{-0.04}$	$0.34^{+0.08}_{-0.08}$	$0.67^{+0.15}_{-0.14}$	$1.3^{+1.4}_{-1.4}$	$-7.6^{+3.9}_{-4.0}$
	10	$16.8^{+1.6}_{-1.8}$	$6.0^{+0.9}_{-0.9}$	$9.0^{+0.9}_{-0.8}$	120^{+24}_{-19}	$0.69^{+0.03}_{-0.03}$	$0.55^{+0.04}_{-0.06}$	$0.36^{+0.09}_{-0.08}$	$0.68^{+0.16}_{-0.16}$	$1.3^{+1.4}_{-1.5}$	$-8.4^{+3.9}_{-3.6}$
	11.3	$25.0^{+2.3}_{-2.2}$	$7.0^{+1.2}_{-1.1}$	$9.0^{+0.7}_{-0.7}$	112^{+21}_{-15}	$0.63^{+0.03}_{-0.04}$	$0.56^{+0.04}_{-0.05}$	$0.28^{+0.07}_{-0.07}$	$0.78^{+0.18}_{-0.17}$	$2.3^{+1.6}_{-1.6}$	$-1.1^{+4.1}_{-4.0}$
NGC 1672	7.7	$19.0^{+2.2}_{-3.3}$	$7.0^{+1.1}_{-0.9}$	$8.7^{+0.9}_{-1.0}$	194^{+104}_{-30}	$0.53^{+0.06}_{-0.10}$	$0.50^{+0.05}_{-0.08}$	$0.37^{+0.10}_{-0.08}$	$0.80^{+0.19}_{-0.17}$	$2.5^{+1.9}_{-1.7}$	$-6.8^{+5.3}_{-5.3}$
	10	$21.0^{+3.0}_{-3.3}$	$7.6^{+1.1}_{-1.2}$	$8.7^{+0.9}_{-1.1}$	194^{+70}_{-26}	$0.59^{+0.05}_{-0.06}$	$0.50^{+0.05}_{-0.06}$	$0.36^{+0.10}_{-0.10}$	$0.87^{+0.23}_{-0.23}$	$3.1^{+1.9}_{-1.9}$	$-5.5^{+5.3}_{-5.7}$
	11.3	$25.6^{+3.0}_{-4.0}$	$8.0^{+0.7}_{-1.3}$	$8.7^{+0.8}_{-0.9}$	192^{+61}_{-26}	$0.57^{+0.05}_{-0.07}$	$0.50^{+0.05}_{-0.06}$	$0.31^{+0.08}_{-0.08}$	$0.91^{+0.19}_{-0.22}$	$3.5^{+1.7}_{-1.9}$	$-1.3^{+5.8}_{-5.7}$
NGC 2835	7.7	$15.7^{+2.1}_{-2.1}$	<4.9	<6.0	<148	$0.64^{+0.03}_{-0.04}$	$0.57^{+0.04}_{-0.04}$	<0.36	⋯	< 3.8	1.6 - 10.8
	10	$10.3^{+1.2}_{-1.5}$	$3.9^{+0.6}_{-0.5}$	$5.6^{+0.5}_{-0.5}$	177^{+74}_{-40}	$0.61^{+0.03}_{-0.04}$	$0.51^{+0.04}_{-0.05}$	$0.38^{+0.10}_{-0.09}$	$0.69^{+0.16}_{-0.14}$	$2.6^{+0.7}_{-0.7}$	$-0.7^{+2.1}_{-1.8}$
	11.3	$19.1^{+1.8}_{-2.7}$	$4.4^{+0.6}_{-0.6}$	$5.6^{+0.4}_{-0.5}$	120^{+39}_{-20}	$0.58^{+0.03}_{-0.04}$	$0.57^{+0.04}_{-0.04}$	$0.23^{+0.06}_{-0.05}$	$0.79^{+0.17}_{-0.15}$	$3.1^{+0.8}_{-0.8}$	$7.6^{+3.1}_{-2.2}$
NGC 3351	7.7	$17.7^{+1.7}_{-1.8}$	$5.0^{+0.8}_{-0.6}$	$6.8^{+0.6}_{-0.6}$	94^{+16}_{-12}	$0.74^{+0.02}_{-0.02}$	$0.57^{+0.02}_{-0.02}$	$0.28^{+0.07}_{-0.06}$	$0.74^{+0.17}_{-0.14}$	$2.5^{+1.0}_{-1.1}$	$-7.5^{+5.3}_{-3.2}$
	10	$20.6^{+2.3}_{-1.7}$	$4.7^{+1.0}_{-0.6}$	$6.8^{+0.6}_{-0.6}$	101^{+10}_{-8}	$0.72^{+0.01}_{-0.01}$	$0.55^{+0.02}_{-0.02}$	$0.23^{+0.06}_{-0.05}$	$0.69^{+0.19}_{-0.15}$	$2.2^{+1.1}_{-1.1}$	$-4.3^{+5.2}_{-3.5}$
	11.3	$24.3^{+2.7}_{-1.6}$	$5.5^{+0.8}_{-0.6}$	$6.8^{+0.4}_{-0.5}$	98^{+9}_{-10}	$0.70^{+0.02}_{-0.01}$	$0.56^{+0.02}_{-0.01}$	$0.23^{+0.05}_{-0.05}$	$0.81^{+0.16}_{-0.14}$	$3.0^{+1.0}_{-1.1}$	$-1.4^{+5.2}_{-3.8}$
NGC 3627	7.7	<14.7	<4.5	<7.0	121^{+32}_{-23}	$0.63^{+0.04}_{-0.05}$	$0.60^{+0.04}_{-0.04}$	⋯	⋯	⋯	⋯
	10	<11.8	<4.6	<7.0	150^{+66}_{-46}	$0.64^{+0.06}_{-0.05}$	$0.55^{+0.07}_{-0.06}$	⋯	⋯	⋯	⋯
	11.3	<15.3	<4.7	<7.0	133^{+44}_{-31}	$0.68^{+0.04}_{-0.05}$	$0.59^{+0.05}_{-0.05}$	⋯	⋯	⋯	⋯
NGC 4254	7.7	$17.1^{+1.8}_{-1.3}$	$6.5^{+0.6}_{-0.6}$	$9.0^{+0.9}_{-0.7}$	102^{+16}_{-18}	$0.62^{+0.03}_{-0.02}$	$0.58^{+0.04}_{-0.02}$	$0.38^{+0.06}_{-0.07}$	$0.72^{+0.11}_{-0.12}$	$1.8^{+1.1}_{-1.4}$	$-2.4^{+3.2}_{-2.6}$
	10	$17.4^{+1.4}_{-1.2}$	$6.4^{+0.7}_{-0.6}$	$9.0^{+0.7}_{-0.6}$	102^{+16}_{-16}	$0.68^{+0.03}_{-0.02}$	$0.57^{+0.04}_{-0.03}$	$0.37^{+0.06}_{-0.06}$	$0.72^{+0.12}_{-0.11}$	$1.7^{+1.2}_{-1.4}$	$-2.0^{+3.2}_{-2.4}$
	11.3	$19.5^{+1.9}_{-1.2}$	$6.8^{+0.7}_{-0.5}$	$9.0^{+0.7}_{-0.6}$	104^{+19}_{-16}	$0.66^{+0.02}_{-0.02}$	$0.57^{+0.03}_{-0.03}$	$0.35^{+0.05}_{-0.05}$	$0.75^{+0.12}_{-0.11}$	$2.0^{+1.2}_{-1.3}$	$-0.2^{+3.2}_{-2.7}$
NGC 4303	7.7	$21.3^{+1.8}_{-1.8}$	$6.8^{+0.9}_{-0.8}$	$8.3^{+0.6}_{-0.8}$	112^{+18}_{-14}	$0.60^{+0.04}_{-0.03}$	$0.55^{+0.04}_{-0.04}$	$0.32^{+0.06}_{-0.06}$	$0.82^{+0.17}_{-0.16}$	$2.8^{+1.5}_{-1.9}$	$-2.2^{+5.0}_{-3.7}$
	10	$21.0^{+1.8}_{-1.7}$	$6.6^{+1.1}_{-0.9}$	$8.3^{+0.6}_{-0.7}$	119^{+16}_{-13}	$0.61^{+0.04}_{-0.03}$	$0.52^{+0.05}_{-0.04}$	$0.31^{+0.07}_{-0.07}$	$0.79^{+0.18}_{-0.17}$	$2.5^{+1.6}_{-2.0}$	$-2.3^{+5.0}_{-3.7}$
	11.3	$28.3^{+1.8}_{-2.1}$	$7.1^{+0.8}_{-0.9}$	$8.3^{+0.5}_{-0.6}$	111^{+15}_{-12}	$0.61^{+0.03}_{-0.03}$	$0.56^{+0.04}_{-0.03}$	$0.25^{+0.04}_{-0.05}$	$0.86^{+0.15}_{-0.15}$	$3.1^{+1.4}_{-2.0}$	$4.6^{+5.1}_{-3.6}$
NGC 4321	7.7	$12.2^{+1.2}_{-1.1}$	<6.2	<8.0	<156	$0.67^{+0.03}_{-0.03}$	$0.55^{+0.04}_{-0.03}$	<0.56	⋯	<3.2	-11.9 - -3.4
	10	$15.4^{+1.5}_{-1.1}$	<6.8	<7.9	<151	$0.72^{+0.02}_{-0.02}$	$0.53^{+0.04}_{-0.03}$	<0.47	⋯	<3.8	-9.3 - 0.1
	11.3	$18.4^{+1.3}_{-1.5}$	<7.1	<7.7	<150	$0.67^{+0.02}_{-0.02}$	$0.53^{+0.03}_{-0.02}$	<0.42	⋯	<4.2	-7.0 - 2.9
NGC 4535	7.7	$18.2^{+2.5}_{-2.3}$	$6.2^{+1.4}_{-1.2}$	$8.9^{+1.1}_{-1.1}$	104^{+12}_{-12}	$0.54^{+0.07}_{-0.05}$	$0.49^{+0.09}_{-0.04}$	$0.34^{+0.11}_{-0.10}$	$0.70^{+0.23}_{-0.21}$	$1.5^{+1.8}_{-2.5}$	$-7.8^{+8.8}_{-4.4}$
	10	$17.6^{+3.0}_{-2.1}$	$6.6^{+1.4}_{-1.4}$	$8.9^{+0.9}_{-1.2}$	137^{+17}_{-19}	$0.49^{+0.08}_{-0.11}$	$0.43^{+0.11}_{-0.12}$	$0.38^{+0.12}_{-0.13}$	$0.75^{+0.24}_{-0.22}$	$2.0^{+1.8}_{-2.6}$	$-8.9^{+8.7}_{-4.7}$
	11.3	$27.0^{+2.5}_{-3.1}$	$6.7^{+1.2}_{-1.0}$	$8.9^{+0.8}_{-0.9}$	108^{+12}_{-10}	$0.52^{+0.06}_{-0.05}$	$0.48^{+0.07}_{-0.04}$	$0.25^{+0.06}_{-0.06}$	$0.75^{+0.19}_{-0.17}$	$2.1^{+1.6}_{-2.4}$	$0.5^{+9.0}_{-4.4}$

Table 3
(Continued)

Galaxy	Band (μm)	t_g (Myr)	t_{fb} (Myr)	t_s (Myr)	λ (pc)	$f_{diffuse}^{mid-IR}$ ...	$f_{diffuse}^{H\alpha}$ ...	t_{fb}/t_g ...	t_{fb}/t_s ...	$\Delta t_{fb,CO}$ (Myr)	$t_{CO-dark}$ (Myr)
NGC 5068	7.7	$27.9^{+3.8}_{-3.7}$	$3.8^{+0.7}_{-0.4}$	$5.5^{+0.3}_{-0.4}$	57^{+25}_{-7}	$0.32^{+0.08}_{-0.14}$	$0.44^{+0.05}_{-0.09}$	$0.14^{+0.04}_{-0.03}$	$0.69^{+0.16}_{-0.11}$	$2.7^{+0.8}_{-0.5}$	$13.7^{+4.4}_{-4.2}$
	10	$21.8^{+4.2}_{-2.4}$	$3.5^{+0.8}_{-0.5}$	$5.5^{+0.3}_{-0.4}$	66^{+16}_{-10}	$0.34^{+0.08}_{-0.12}$	$0.42^{+0.05}_{-0.08}$	$0.16^{+0.05}_{-0.05}$	$0.64^{+0.17}_{-0.13}$	$2.5^{+0.9}_{-0.6}$	$7.9^{+3.3}_{-4.6}$
	11.3	$32.2^{+5.4}_{-3.4}$	$4.2^{+0.9}_{-0.5}$	$5.5^{+0.3}_{-0.4}$	60^{+10}_{-8}	$0.28^{+0.09}_{-0.11}$	$0.36^{+0.06}_{-0.07}$	$0.13^{+0.04}_{-0.04}$	$0.77^{+0.19}_{-0.14}$	$3.2^{+0.9}_{-0.6}$	$17.7^{+4.1}_{-5.7}$

Note. Columns are mid-IR wavelengths (Band), mid-IR emitting timescale (t_g), feedback timescale (t_{fb}), Hα emitting timescale (t_s), average region separation length (λ), diffuse emission fractions of mid-IR and Hα maps ($f_{diffuse}^{mid-IR}$ and $f_{diffuse}^{H\alpha}$), fraction of the mid-IR emitting phase associated with Hα emission (t_{fb}/t_g), fraction of the Hα emitting phase associated with mid-IR emission (t_{fb}/t_s), difference in feedback timescales when using mid-IR and CO as the gas tracer ($\Delta t_{fb,CO}$), and the duration of gaseous mid-IR emitting phase dark in CO ($t_{CO-dark}$). For galaxies affected by blending of sources (see Section Appendix B), we show lower and/or upper limits when possible.

4.2. Mid-IR Emitting Timescale

Across our sample of galaxies, the mid-IR emitting timescale of gas clouds in the galactic disk is measured to range $t_g^{7.7\,\mu m} = 11 - 28$ Myr, $t_g^{10\,\mu m} = 10 - 26$ Myr, and $t_g^{11.3\,\mu m} = 14 - 35$ Myr when 7.7, 10, and 11.3 μm are used, respectively. The average and 16–84% range for each mid-IR band are 18 ± 5 Myr, 18 ± 4 Myr, and 23 ± 5 Myr, for 7.7 μm, 10 μm, and 11.3 μm, respectively. Figure 5 compares mid-IR emitting timescales across different mid-IR bands and shows that $t_g^{7.7\,\mu m}$ are longer than $t_g^{10\,\mu m}$ for relatively metal-poor galaxies. The $t_g^{11.3\,\mu m}$ is somewhat longer than the mid-IR emitting timescale measured with the other two bands. The F1130W band, while dominated by the 11.3 μm PAH feature, likely contains a higher level of dust continuum emission in thermal equilibrium with the radiation field in and around H II regions, compared to the dust continuum in the two shorter-wavelength bands (J. D. T. Smith et al. 2007; T. S. Y. Lai et al. 2022). This will increase the overlap between mid-IR and Hα, as shown in Figures 3 and 4, and therefore the total 11.3 μm emitting timescale.

As described in Section 2.1, the mid-IR emission traces multiple gas phases and is influenced by a combination of gas column density, radiation, and abundances of dust and PAHs. Therefore, the physical interpretation of the mid-IR emitting timescale is not trivial. The strong correlation between mid-IR (or PAH) bands and cold gas (R. Chown et al. 2021, 2025; Y. Gao et al. 2022; A. K. Leroy et al. 2023; C. M. Whitcomb et al. 2023) suggests that the measured mid-IR emitting timescale likely reflects the neutral gas phase, particularly the compact neutral gas structures (K. M. Sandstrom et al. 2023a) with our diffuse emission filtering process. However, this assumes that dust and PAHs are mainly illuminated by the diffuse interstellar radiation field, which may not hold true, especially for bright mid-IR peaks often associated with star-forming regions (A. K. Leroy et al. 2023; D. Pathak et al. 2024). In addition, we also note that our method is flux weighted, which naturally biases our measurements toward bright mid-IR emission peaks, which could make the mid-IR emitting timescale more related to gas near H II regions and not fully capture the entire neutral gas cloud phase.

With these caveats in mind, in Figure 6 we have compared our measurements of the mid-IR emitting timescale and GMC lifetimes from J. Kim et al. (2022). We find that the mid-IR emitting timescale is similar to the CO-emitting timescale (molecular cloud lifetime t_g^{CO} from J. Kim et al. 2022) with averages and 1σ distributions of their ratio (t_g^{mid-IR}/t_g^{CO}) being 1.1 ± 0.4, 1.1 ± 0.3, and 1.3 ± 0.5, for 7.7 μm, 10 μm, and 11.3 μm, respectively. Compared to the characteristic timescales of GMCs (E. Rosolowsky et al. 2021; J. Sun et al. 2022; A. Hughes 2025, in preparation), the mid-IR emitting timescale is, on average, 2–3 times longer than the average GMC freefall timescale and GMC turbulence crossing timescales (see Section 5.3).

The similarity between the mid-IR and CO-emitting timescales might seem surprising, as Figure 2 shows significant differences in the flux ratio deviations, where branches diverge more significantly when CO is used compared to when mid-IR bands are used. The top branch with mid-IR, where flux ratios are measured by focusing apertures on mid-IR peaks, is close to the galactic average value being almost flat in some galaxies even on small scales. The main reason for the much narrower branches with mid-IR compared to CO is because of the longer overlapping timescale between mid-IR and Hα (see Section 4.3) than that measured between CO and Hα, which makes the deviation of flux ratios smaller. We also note that, while the small deviation of the top branch with mid-IR might indicate that all of the mid-IR peaks have associated Hα emission, we still measure a long, isolated mid-IR emitting phase (see Figure 4). This is related to the flux evolution of independent star-forming regions considered within our model. We make use of the ratios of timescales (t_{fb}/t_g and t_{fb}/t_s) to constrain the flux ratios of mid-IR and Hα peaks in their overlap phase relative to their isolated phases (β_{mid-IR} and $\beta_{H\alpha}$, respectively; J. M. D. Kruijssen et al. 2018). We find that, for most of our galaxies, $\beta_{H\alpha}$ is quite high (3 on average), implying that Hα peaks are brighter in their initial phase when overlapping with mid-IR compared to when they are in an isolated Hα emitting phase later on. This makes sense given that the overlap phase lasts 6 Myr, covering the period where Hα emission is the brightest during the H II region evolution (C. Leitherer et al. 1999). As a result, even though there are many mid-IR peaks not overlapping with Hα (and therefore a long isolated mid-IR emitting phase; see also Figure 1), Hα peaks in the overlapping phase with mid-IR are much brighter, and this makes the top branch appear flatter on small scales and deviate less from the galactic average ratio. In contrast, when CO is adopted, we find $\beta_{H\alpha}$ is 1 on average and a shorter $t_{fb} \approx 3$ Myr.

Before star formation is detected in Hα, we define the mid-IR emitting phase without associated CO (and Hα) emission as the CO-dark mid-IR emitting cloud phase ($t_{CO-dark}^{mid-IR}$ or $t_{CO-dark}^{X}$ for a specific mid-IR band X), which can be obtained as $t_{CO-dark}^{X} = t_g^X - t_{fb}^X - (t_g^{CO} - t_{fb}^{CO})$, where t_{fb}^{CO} is the feedback timescale measured with CO. We find that the average and 1σ

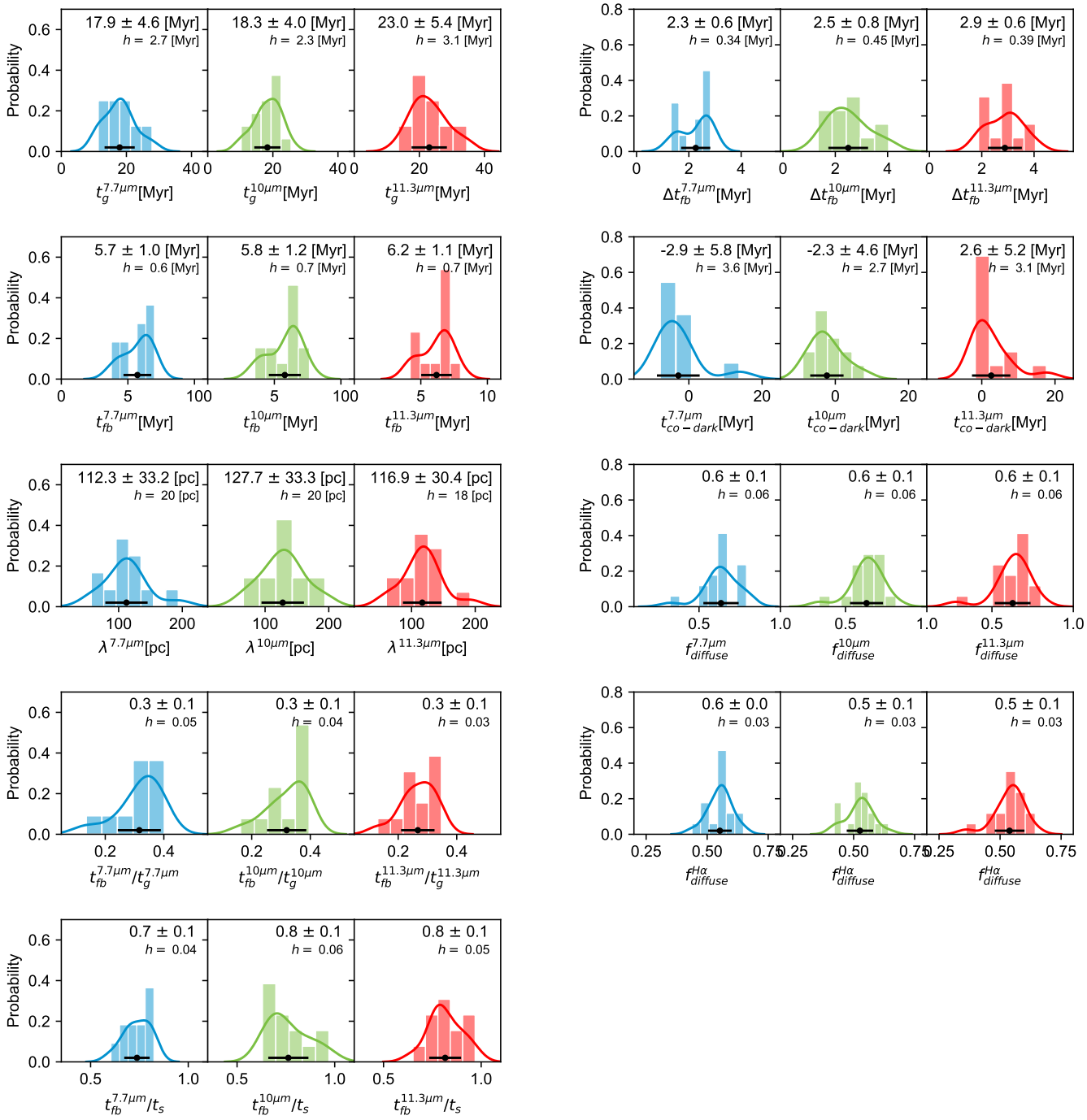

Figure 3. Distributions of physical quantities listed in Table 3, which are from the application of the method described in Section 3 to mid-IR and Hα observations of 17 galaxies. For each physical quantity, results with 7.7, 10, and 11.3 μm are shown in blue, green, and red, respectively. The solid line shows the smoothed distribution based on a Gaussian kernel density estimate, with the bandwidth (h; shown in each panel) selected according to Scott's rule (D. W. Scott 1992). Table 3 lists actual values and galaxies with only upper or lower limit constraints being excluded (see Section Appendix B). In each histogram, the mean (black dot) and 16%–84% range (horizontal line) are shown, as well as in the upper-right corner.

range of $t_{\rm CO-dark}^{\rm mid-IR}$ are -3 ± 6 Myr, -2 ± 5 Myr, and 3 ± 5 Myr, respectively, for 7.7, 10, and 11.3 μm. In most galaxies in our sample, regardless of the mid-IR bands, the measured $t_{\rm CO-dark}^{\rm mid-IR}$ is consistent with being zero, indicating that the distributions of CO and compact mid-IR emission are similar before star formation commences. This implies that once gas clouds assemble, being associated with compact mid-IR peaks, they immediately provide sufficient shielding for CO to become stable. The conversion from neutral gas clouds (traced by compact mid-IR emission) to CO-emitting GMCs occurs very rapidly, which is likely given that our observations are focused on the molecular gas-rich central regions of galaxies with high gas surface density and near-solar metallicity. In the case of lower density and diffuse ISM regime, simulations suggest that there may be a few Myr when compact gas clouds are present, but the conditions are insufficient to provide the shielding required for CO formation during the molecular gas cloud assembly (P. C. Clark et al. 2012; R. J. Smith et al. 2014). We also found exceptions (NGC 1566 and NGC 4321), where we measure strongly

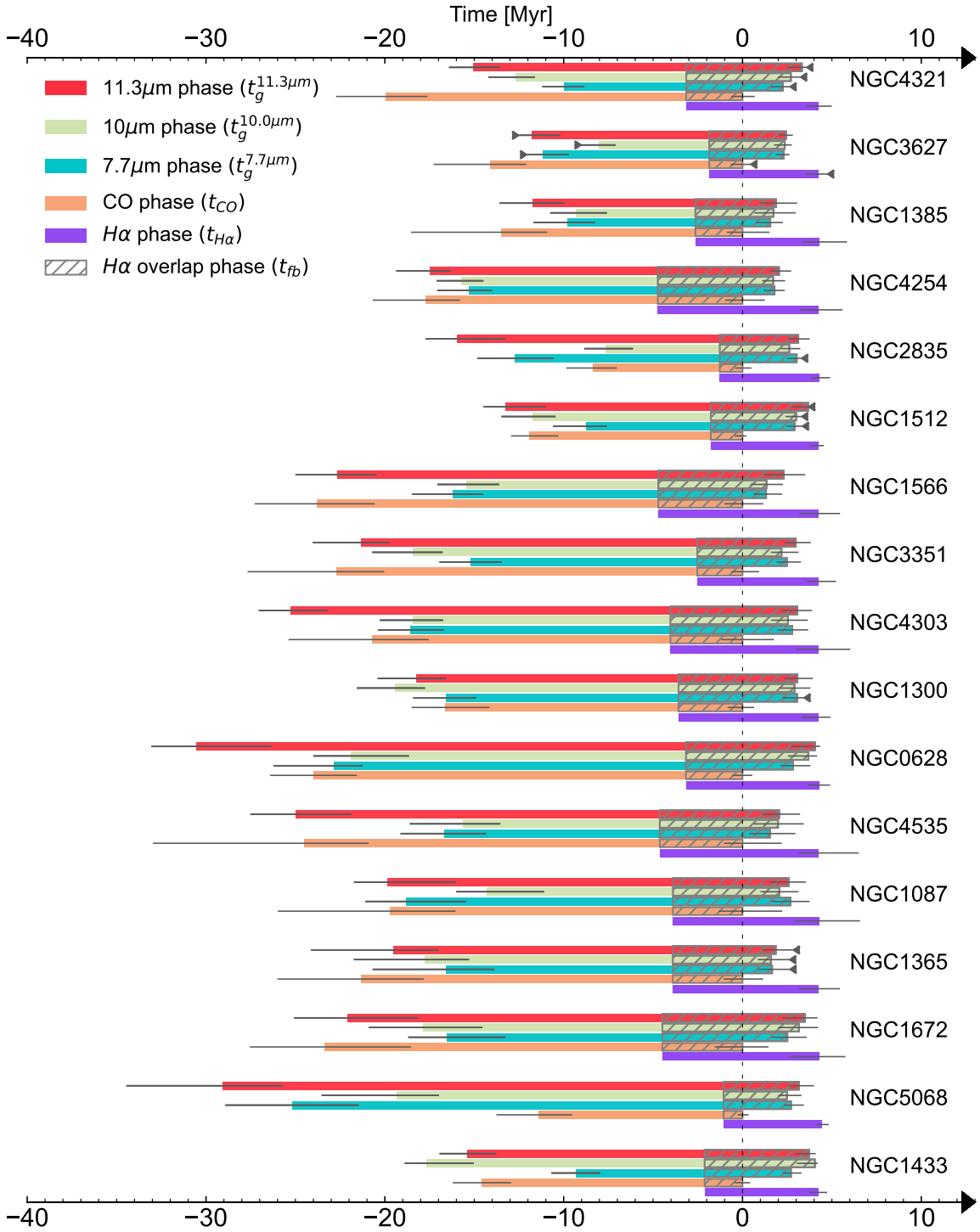

Figure 4. The multitracer timeline of cloud evolution in PHANGS-JWST galaxies. From left to right, clouds are initially inert, being detected only in CO and mid-IR, tracing the cold gaseous phase. Star formation then takes place, causing gas tracers to become coincident with Hα emission (dashed region). In most galaxies, mid-IR bands (7.7, 10, and 11.3 μm) fully cover the molecular gas phase traced with CO. The dashed line at Time = 0 Myr indicates the moment when the CO emission disperses. The mid-IR emission persists for a longer period after the CO emission has been dispersed by stellar feedback (dashed line) and remains detectable for 2–3 Myr, on average, covering a significant fraction of the Hα emitting phase. Galaxies are ordered by the increasing Hα flux density contrast measured between the Hα peak and galactic average ($\epsilon_{\rm H\alpha}$), which shows a strong correlation with 10 μm emitting timescales (see Figure 7 and Section 5.1.3). Galaxies with only upper-limit constraints are indicated with left- or right-pointing triangles.

negative $t_{\rm CO-dark}^{\rm mid-IR}$. This is likely due to the breakdown of the mid-IR and CO flux correlation and is discussed in more detail in Section 5.2.

We have also compared our measurements to the neutral gas cloud lifetime measured with H I in the LMC (J. L. Ward et al. 2020, 2022). We find that our measurements of a very short $t_{\rm CO-dark}^{\rm mid-IR}$ contrast the results of the LMC, where the neutral gas cloud lifetime is ∼5 times longer than the molecular gas cloud lifetime. The neutral gas cloud phase traced with H I but dark in CO ($t_{\rm CO-dark}^{\rm HI}$) is found to be ≈35 Myr. Using [C II] and [C I]

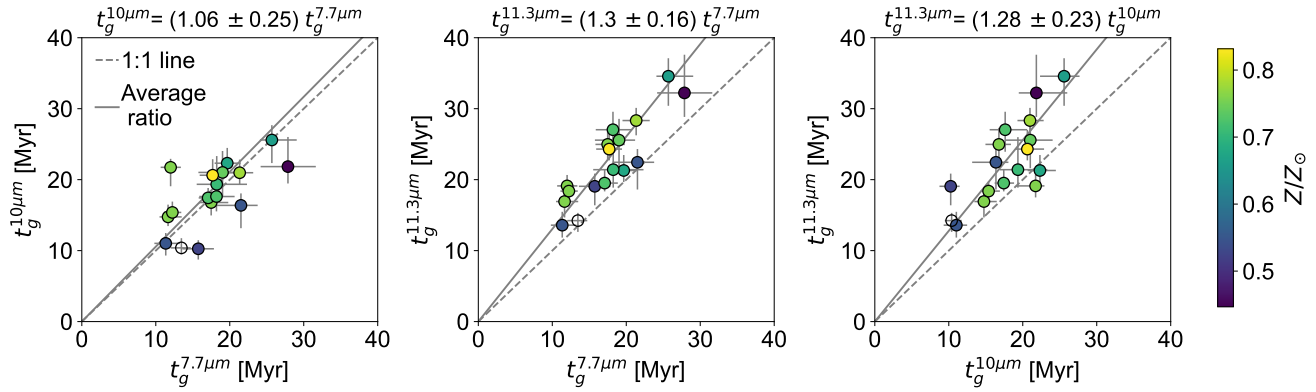

Figure 5. Comparisons of mid-IR emitting timescales obtained using different bands ($t_g^{7.7,\mu m}$, $t_g^{10,\mu m}$, and $t_g^{11.3,\mu m}$). The average ratio between two timescales and the 1σ distributions are indicated in each panel. The solid line indicates the relation using the average ratio, whereas the dashed line shows a one-to-one correlation. Data points are color-coded by metallicity relative to the solar value ($Z/Z_\odot$), whereas the empty circle indicates NGC 3627 where our measurements are upper limits. While the three mid-IR emitting timescales generally agree regardless of the wavelength, the left panel shows that $t_g^{7.7,\mu m}$ is longer than $t_g^{10,\mu m}$ for metal-poor galaxies. Additionally, $t_g^{11.3,\mu m}$ is slightly longer than both $t_g^{7.7,\mu m}$ and $t_g^{10,\mu m}$.

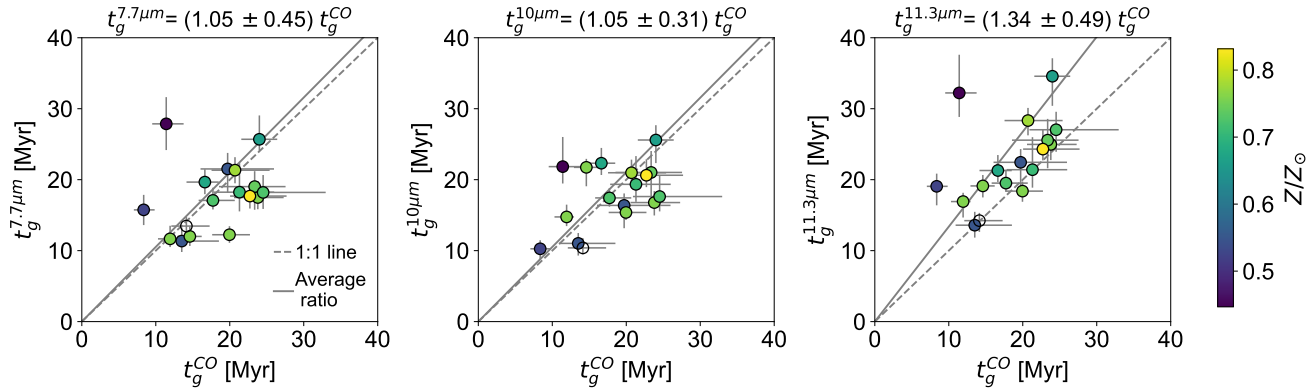

Figure 6. Similar to Figure 5, GMC lifetimes compared to mid-IR emitting timescales obtained using different bands ($t_g^{7.7,\mu m}$, $t_g^{10,\mu m}$, and $t_g^{11.3,\mu m}$) are shown. We find that the two timescales agree well, suggesting that once gas clouds form, being associated with compact mid-IR emission, they quickly provide enough shielding for stable CO formation. This is likely due to our focus on molecular gas-rich, central regions of galaxies with near-solar metallicity.

lines in the far-infrared, J. L. Pineda et al. (2017) found that 70%–80% of the molecular gas in the LMC and Small Magellanic Cloud is dark in CO.

While it is difficult to make a direct comparison as our measurements are biased toward bright mid-IR peaks that are associated with star-forming regions rather than the neutral gas distribution, we suspect that the significant difference in $t_{\rm CO-dark}^{\rm HI}$ and $t_{\rm CO-dark}^{\rm mid-IR}$, between the LMC (J. L. Ward et al. 2020, 2022) and our galaxy sample, is mainly due to the fact that our JWST observations are focused on the central part of the galaxy, where the majority of the ISM mass is in the form of molecular gas and has a high gas surface density. The average molecular gas fraction ($f_{\rm H_2}$) of our galaxy sample is 0.5 ± 0.2, whereas in the LMC, the fraction is quite low ($f_{\rm H_2}$ = 0.09; A. Schruba et al. 2019). The high molecular gas fraction enhances the stability of CO, making it a more reliable tracer of cold molecular gas (P. C. Clark et al. 2012). In an atomic-gas-dominated environment, CO is only emitted from the central region of the HI clumps, causing the timescales between the two gas phases to be significantly different. Furthermore, our sample of galaxies has almost solar metallicity ($Z/Z_\odot = 0.7 \pm 0.1$), unlike the LMC, which has a lower metallicity of ($Z/Z_\odot = 0.5$). This allows CO to be photodissociated more easily in the LMC due to the lack of shielding, resulting in a large reservoir of neutral gas clouds that are dark in CO emission in a metal-poor environment (A. D. Bolatto et al. 2013; J. L. Pineda et al. 2017). Indeed, $t_{\rm CO-dark}^{\rm mid-IR}$ shows negative trends with metallicity (see Figures 7 and Section 5.1.1). For the lowest metallicity and the lowest-metallicity galaxy in our sample, NGC 5068, we measure $t_{\rm CO-dark}^{\rm mid-IR}$ to be the longest, ranging from 10–20 Myr depending on the mid-IR bands. This is discussed in more detail in Section 5.1.1.

4.3. Mid-IR and Hα Overlapping Timescale

The duration for which the mid-IR emission overlaps with Hα ranges from 3.8–7.0 Myr, 3.5–7.6 Myr, and 4.2–8.0 Myr, with an average and 16%–84% range of 5.7 ± 1.0 Myr, 5.8 ± 1.2 Myr, and 6.2 ± 1.1 Myr, for 7.7, 10, and 11.3 μm, denoted as $t_{\rm fb}^{7.7\,\mu m}$, $t_{\rm fb}^{10\,\mu m}$, and $t_{\rm fb}^{11.3\,\mu m}$, respectively. The majority of the Hα emitting phase has associated mid-IR emission, with an average ratio $t_{\rm fb}^{\rm mid-IR}/t_{\rm s}$ of 70%–80%.

While there is evidence of PAH destruction within H II regions (J. Chastenet et al. 2019, 2023; O. V. Egorov et al. 2023; J. Sutter et al. 2024), we are not likely resolving the ISM shells and bubbles created by young stars on scales of 100 pc. Therefore, the significant overlap between mid-IR and Hα emission is because H II regions are major contributors to ultraviolet and optical radiations, which illuminate the PAHs and dust grains near H II regions and thus allow mid-IR emission to continue during the Hα emitting phase. Our

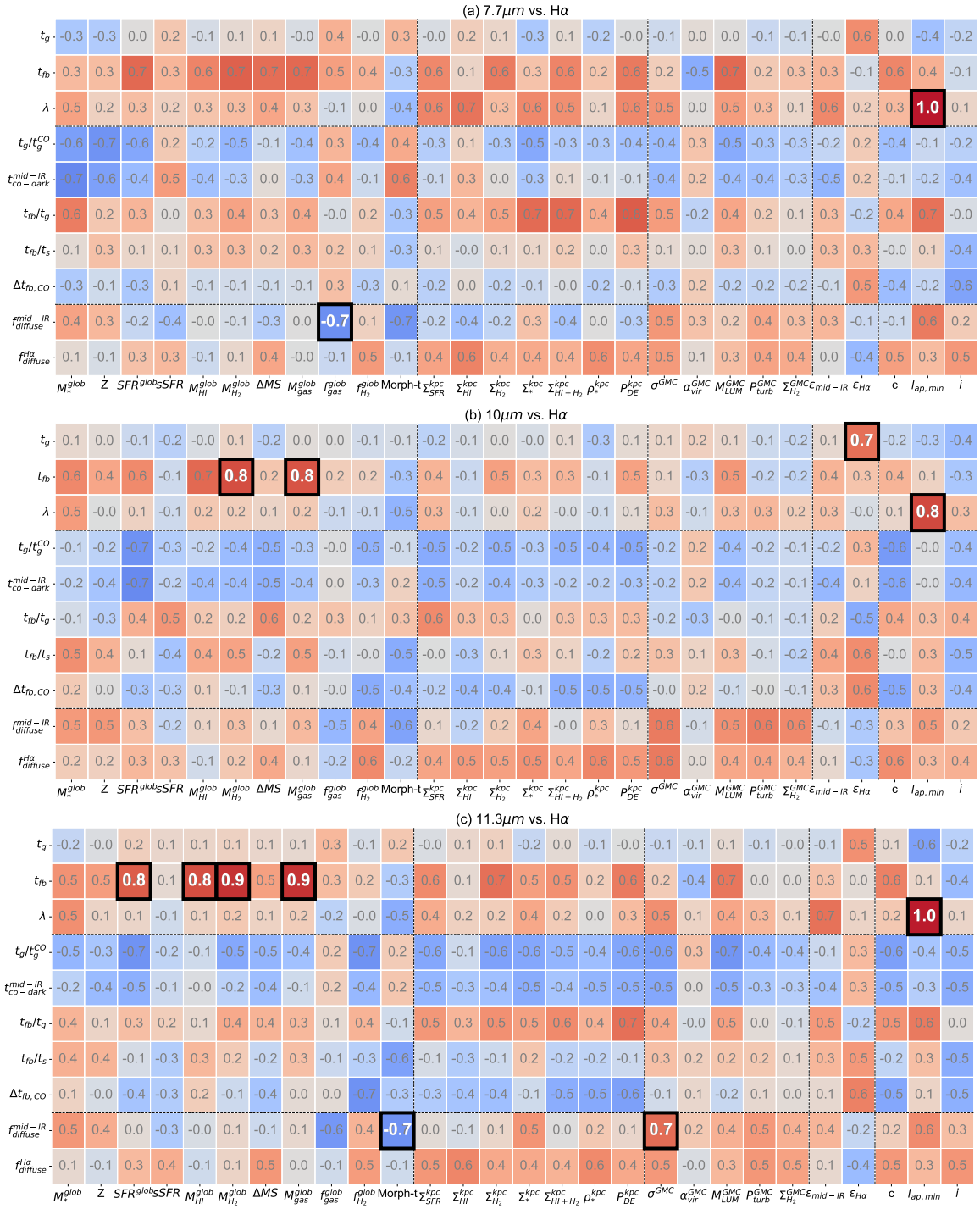

Figure 7. Spearman's rank correlation coefficients measured between galaxy properties (columns; Section 5.1) and our measurements (rows; Section 4). From (a)–(c), correlations obtained using different mid-IR bands (7.7, 10, and 11.3 μm) are shown, respectively. Statistically strong correlations are highlighted as black squares, with red indicating a positive correlation and blue indicating a negative one. Our measurements are the mid-IR emitting timescale (t_g), feedback timescale (t_{fb}), region separation length (λ), ratios between timescales (t_g/t_g^{CO}, t_{fb}/t_g, t_{fb}/t_s), duration of the mid-IR emitting phase dark in CO and Hα ($t_{CO-dark}$), difference between the overlap timescales measured with mid-IR vs. CO ($\Delta t_{fb,CO}$), and diffuse emission fractions ($f_{diffuse}^{mid-IR}$ and $f_{diffuse}^{H\alpha}$). We correlate these measurements with global galaxy properties, average kiloparsec-scale galaxy properties, average GMC properties, average surface flux density contrasts between emission peaks and galactic average measured in mid-IR and Hα maps, and systematic biases described in Section 5.1.

measurements also show that the mid-IR emitting phase ends before Hα, implying that the overlapping timescale can be referred to as the feedback timescales at scales of $\sim$100 pc for PAHs (and dust grains) dispersal. If we were to resolve the PAH suppression at a smaller scale, the feedback timescale would likely be shorter. The range of the overlap timescale is similar to the ages of clusters associated with compact PAH and H II region morphologies, which have an age span of 1–6 Myr, with an average of 4 Myr (A. Pedrini et al. 2024).

As shown in Figure 4, we find that the overlapping or feedback timescale obtained with mid-IR is always longer than 3 Myr and is also longer than that obtained with CO as a cold

gas tracer ($t_{\rm fb}^{\rm CO}$). We measure the difference in the feedback timescales between mid-IR bands and CO as $\Delta t_{\rm fb,CO}^{X} = t_{\rm fb}^{X} - t_{\rm fb}^{\rm CO}$, where X denotes mid-IR bands. We find the difference to range 1.3–2.8 Myr, 1.3–4.0 Myr, and 1.9–4.1 Myr, for $\Delta t_{\rm fb,CO}^{7.7\,\mu{\rm m}}$, $\Delta t_{\rm fb,CO}^{10\,\mu{\rm m}}$, and $\Delta t_{\rm fb,CO}^{11.3\,\mu{\rm m}}$, respectively. The longer feedback timescale with mid-IR compared to CO is likely because PAH or dust emission is enhanced by the presence of nearby intense radiation from young stars. This leads to enhanced mid-IR emission near (but not inside) H II regions, whereas CO is expected to be dispersed quickly. Assuming that our detection of emission peaks is symmetric in terms of mass traced across different tracers, our measurements imply that in and near H II regions, 30%–70% of the compact mid-IR emission is dark in CO, with an average of ∼45%. This is somewhat smaller than the mass fraction of CO-dark molecular gas (∼75%) measured in a star bursting region in the LMC (30 Doradus M. Chevance et al. 2020c), possibly due to the lower metallicity and sparser ISM density of the LMC. However, we also note that limited sensitivity of CO emission could also contribute to the differences. It is possible that when the cloud is dispersed, CO emission falls below the detection limit earlier on compared to the deeper JWST observations.

4.4. Average Separation Length between Regions

Figure 1 demonstrates that gas and SFR tracers show distinct distributions, reflecting the fact that they trace different phases of region evolution from gas to stars. Our method constrains the average separation length between these regions ($\lambda^{\rm mid-IR}$), which is measured to range 60–190 pc across our analysis with different mid-IR bands, with their average and 16%–84% range of 112 ± 33, 128 ± 33, and 117 ± 30 pc for $\lambda^{7.7\ \mu{\rm m}}$, $\lambda^{10\ \mu{\rm m}}$, and $\lambda^{11.3\ \mu{\rm m}}$, respectively.

As indicated by the arrow in each panel of Figure 2, the measured λ with mid-IR as the neutral gas tracer is smaller than that measured with CO as the molecular gas tracer ($\lambda^{\rm CO}$ = 100–310 pc, with an average of 230 ± 60 pc). In J. Kim et al. (2022), we pointed out that the λ is the most sensitive to the resolution while other constrained parameters such as the cloud lifetime and the feedback timescale do not show strong correlations with the resolution. This is also illustrated in Figure 7, where λ strongly correlates with resolution $l_{\rm ap,min}$, while the correlations with mid-IR emitting and overlapping timescales are weak. The difference in λ between mid-IR and CO is most likely due to the difference in resolution and sensitivity between the two observations. The minimum aperture sizes in Figure 2 indicate the resolutions adopted in runs with different gas tracers. It shows that CO observations have the coarsest resolution, possibly leading to a larger region separation length.

4.5. Diffuse Emission Fractions

As our method is based on the measurements of the deviation of the local flux ratio compared to the global flux ratio, it is important that flux ratios are not biased by the existence of large-scale diffuse emission that is not associated with identified emission peaks. We therefore filter out large-scale diffuse emission with a scale larger than $n_\lambda\lambda \approx 1.5$ kpc using a Gaussian high-pass filter in Fourier space (see Section 3 for the justification of n_λ). The adopted filtering scale is similar to the size of the most extended coherent, primarily atomic HI filament identified in the Milky Way (the "Maggie" Filament with a total length of 1.2 kpc; J. Syed et al. 2022), confirming that our chosen scale effectively removes large-scale diffuse emission while preserving emission from compact structures. This allows us to measure diffuse emission fractions in mid-IR and Hα tracer maps, which are derived solely from the morphological features. We find diffuse emission fractions in mid-IR emission maps ($f_{\rm diffuse}^{\rm mid-IR}$ or $f_{\rm diffuse}^{X}$ when referring to a specific band) to range 32%–79%, 34%–81%, and, 28%–80% for 7.7, 10, and 11.3 μm, respectively. The average and 1σ range of diffuse mid-IR emission fraction are very similar among different wavelengths (60% ± 10%). As for the diffuse emission fraction in the Hα map, $f_{\rm diffuse}^{\rm H\alpha}$, we find it to range from 40%–60%, with an average of 50%–60%.

Using the Spitzer 8 μm emission map of M33, S. Verley et al. (2009) measured a similar diffuse mid-IR emission fraction, which ranges fro 40%–60% with the fraction increasing at larger radii (see also Y. Li et al. 2013). Our measurements of $f_{\rm diff}^{\rm H\alpha}$ also agree well with estimates from F. Belfiore et al. (2022), who found the diffuse ionized gas fraction to range from 20%–55%, using the same PHANGS-MUSE observations. H.-A. Pan et al. (2022) employed an unsharp masking technique to estimate the Hα diffuse emission fraction in PHANGS galaxies using narrowband Hα observations (A. Razza et al. 2025, in preparation), which ranges from 40%–90%.

Using the locations and sizes of H II regions from B. Groves et al. (2023) for PHANGS-JWST Cycle 1 galaxies, D. Pathak et al. (2024) found that mid-IR emission is brighter and more compact when associated with H II regions. In contrast, mid-IR emission in non–H II regions is generally fainter and more extended. Excluding galaxy centers, D. Pathak et al. (2024) reported that around 50%–80% of the mid-IR emission in galactic disks originates from outside of H II regions and is therefore likely to be diffuse. We find good agreement between the fraction of mid-IR emission in non–H II regions and the diffuse emission fraction measured using Fourier filtering. This suggests that the timescales derived from this method trace the evolutionary cycle of gas clouds involved in star formation, while excluding the more diffuse gas that likely does not participate in star formation.

5. Discussion

5.1. Correlations between Global Galaxy Properties and Cloud Evolutionary Timescales

In order to understand the effects of environment on the cloud evolution, we have correlated our measurements listed in Table 3 with galaxy and average GMC properties. Galaxy properties include globally observed properties listed in Table 1 ($M_*^{\rm glob}$, ${\rm SFR}^{\rm glob}$, $M_{\rm HI}^{\rm glob}$, $M_{\rm H_2}^{\rm glob}$, ΔMS, Z, and Hubble T-type), as well as other derived properties such as specific SFR (${\rm sSFR} = {\rm SFR}^{\rm glob}/M_*^{\rm glob}$), total gas mass ($M_{\rm gas}^{\rm glob} = M_{\rm HI}^{\rm glob} + M_{\rm H_2}^{\rm glob}$), gas fraction ($f_{\rm gas}^{\rm glob} = M_{\rm gas}^{\rm glob}/(M_{\rm gas}^{\rm glob} + M_*^{\rm glob})$), and molecular gas fraction ($f_{\rm H_2}^{\rm glob} = M_{\rm H_2}^{\rm glob}/M_{\rm gas}^{\rm glob}$).

We include mass-weighted averages of kiloparsec-scale galaxy properties measured by J. Sun et al. (2022). These are surface densities of the SFR, atomic gas, molecular gas, and neutral gas ($\Sigma_{\rm SFR}^{\rm kpc}$, $\Sigma_{\rm HI}^{\rm kpc}$, $\Sigma_{\rm H_2}^{\rm kpc}$, and $\Sigma_{\rm HI+H_2}^{\rm kpc}$), the density of the stellar mass volume near the midplane of the disk ($\rho_*^{\rm kpc}$), and

the dynamical equilibrium pressure ($P_{\rm DE}^{\rm kpc}$), which is the pressure required to support ISM within the gravitational potential of a galaxy (e.g., J. Sun et al. 2020).

For the average GMC properties, we obtain mass-weighted averages of the velocity dispersion ($\sigma^{\rm GMC}$), virial parameter ($\alpha_{\rm vir}^{\rm GMC}$), GMC mass ($M^{\rm GMC}$), internal turbulent pressure ($P_{\rm turb}^{\rm GMC}$), and molecular gas surface density ($\Sigma_{\rm H_2}^{\rm GMC}$), using the GMC catalog generated using the CPROPS algorithm (E. Rosolowsky et al. 2021; A. Hughes et al. 2025, in preparation) for PHANGS-ALMA (A. K. Leroy et al. 2021a) galaxies. When calculating the averages, we exclude GMCs located in the central regions of the galaxy, which have been masked from our analysis (Table 2).

We also explore correlations with environmental metrics constrained within the method, $\epsilon_{\rm mid-IR}$ ($\epsilon_{\rm H\alpha}$), which represents the surface flux density contrast measured between the average emission peak of mid-IR (Hα) and the galactic average value, on a diffuse emission filtered map. The higher-density contrast implies that the emission peak is sharper with less crowding and less background. Finally, we test the effects of systematic biases by examining correlations with the minimum aperture size ($l_{\rm ap,min}$; see Table 2), the inclination (i; see Table 1), and the mass-weighted average of CO flux completeness on the kiloparsec scale (c; from A. K. Leroy et al. 2021b; J. Sun et al. 2022). The latter c is measured as the ratio between the total flux in the moment-0 map when strict signal identification criteria are adopted ("strict" moment-0 map) compared to that when a more generous criteria is used to include all regions of the cube that are likely to contain signal ("broad" moment-0 map), $c = \Sigma{\rm strict\,mom0}/\Sigma{\rm broad\,mom0}$.[33] Therefore, the completeness (c) compares the total CO flux recovered using high-confidence emission regions to that using the full, inclusive mask. Deeper observations, with higher signal-to-noise ratio (S/N), would allow for more of the true CO emission to satisfy the strict mask criteria, making c closer to 1. In shallower data, much of the real emission is only captured by the broad mask, resulting in lower c. Therefore, c serves as a proxy for the depth and flux recovery efficiency of the CO data (A. K. Leroy et al. 2021a, 2021b; J. Sun et al. 2022). In Figure 7, we illustrate Spearman's rank correlation coefficients computed between our measurements and the galaxy environmental properties described above. In the following subsections, we discuss the significance and physical implications of the observed correlations.

5.1.1. Theoretical Expectations

In theory, the H I and H_2 equilibrium timescale ($t_{\rm eq}$), which is the time required to reach a balance between formation and destruction rates of H_2, is described as

$$t_{\rm eq} = \frac{1}{2Rn + D + \zeta}, \quad (1)$$

where R is the H_2 formation rate, n is the mean H nucleon number density or the rms density in the presence of turbulence, D is the local photodissociation rate including H_2 self-shielding, and ζ is the cosmic-ray ionization rate. Assuming the case of a well-shielded region ($D \ll Rn$) with a negligible H_2 dissociation by cosmic rays (A. Sternberg et al. 2024),

$$t_{\rm eq} = \frac{1}{2Rn} \approx \frac{10^9}{Z_d' n}\ {\rm yr}, \quad (2)$$

where R is assumed to be $3 \times 10^{-17} Z_d'\ {\rm cm^3 s^{-1}}$ and Z_d' is the dust-to-gas ratio relative to the solar neighborhood value (M. Chevance et al. 2023; S. Bialy et al. 2025). This implies that when the dust-to-gas ratio and gas density are higher, $t_{\rm eq}$ becomes shorter and the conversion from atomic gas to molecular gas is rapid, allowing the equilibrium between H I and H_2 to be reached faster. In the case of photodissociation-dominated regions, related to the mid-IR and Hα overlap phases, theories suggest that the fraction of CO-dark gas should increase at lower metallicities due to reduced shielding of CO (M. G. Wolfire et al. 2010; M. Chevance et al. 2020c; S. C. Madden et al. 2020; M. G. Wolfire et al. 2022).

We therefore expect the mid-IR and CO-emitting timescales to be more similar with their ratio ($t_{\rm g}^{\rm mid-IR}/t_{\rm g}^{\rm CO}$) close to one at higher metallicity and gas surface density environments. However, we note that our analysis here with mid-IR and J. Kim et al. (2022) with CO have differences in the spatial resolution and sensitivity. The difference in resolution is not expected to significantly bias the trends observed with $t_{\rm g}^{\rm mid-IR}/t_{\rm g}^{\rm CO}$, as shown in Figure 7, with Spearman's rank correlation coefficients between $t_{\rm g}^{\rm mid-IR}/t_{\rm g}^{\rm CO}$ and resolution ($l_{\rm ap,min}$) being almost zero for 7.7 and 10 μm and -0.4 with 11.3 μm. On the other hand, $t_{\rm g}^{\rm mid-IR}/t_{\rm g}^{\rm CO}$ and CO flux completeness (c), indicating how deep the CO observation is, shows stronger trends with coefficients ranging from -0.4 to -0.6. This suggests that trends observed with $t_{\rm g}^{\rm mid-IR}/t_{\rm g}^{\rm CO}$ could be influenced by the differences in CO sensitivity. This is discussed in more detail below.

Figure 7 shows that $t_{\rm g}^{\rm mid-IR}/t_{\rm g}^{\rm CO}$ exhibits negative trends with Z and gas surface densities ($\Sigma_{\rm H_2}^{\rm kpc}$ and $\Sigma_{\rm HI+H_2}^{\rm kpc}$). However, they were not characterized as statistically significant (see Section 5.1.2). In Figure 8, we show how the $t_{\rm g}^{\rm mid-IR}/t_{\rm g}^{\rm CO}$ varies as a function of metallicity and molecular gas surface density. Among mid-IR bands, $t_{\rm g}^{7.7\,\mu{\rm m}}/t_{\rm g}^{\rm CO}$ shows the tightest relation with metallicity with a correlation coefficient (ρ) of -0.7, while $t_{\rm g}^{11.3\,\mu{\rm m}}/t_{\rm g}^{\rm CO}$ best correlates with molecular gas surface density with $\rho = -0.6$. These observed relations appear to agree with theoretical expectations, where the ratio decreases with increasing metallicity and molecular gas surface density. In high-metallicity and high-density environments, the compact mid-IR emitting phase is similar to the molecular gas cloud lifetime traced with CO, with their ratio close to 1. This suggests that, in these environments, the compact mid-IR emission primarily comes from molecular gas clouds, with their entire extent being bright in CO. It implies that the conversion from cold neutral medium (traced only with compact mid-IR) to molecular gas clouds with stable CO (traced with mid-IR and CO) is rapid. However, in low-metallicity and sparse ISM environments, which are likely to be atomic-gas-dominated, the assembly of clouds can take a while and, similarly, it takes a while for the column density to reach sufficient values for CO to be stable against photodissociation (see P. C. Clark et al. 2012), leading to a greater

[33] While we refer readers to A. K. Leroy et al. (2021b) for full details on how these masks are generated, in brief, the strict mask includes regions with S/N > 2 over two consecutive velocity channels, but only retains those that are spatially and spectrally connected to a core mask defined by S/N > 4 over two channels. The broad mask is defined as the union of all strict masks across resolutions, capturing extended and faint emission and encompassing all emission from the galaxy.

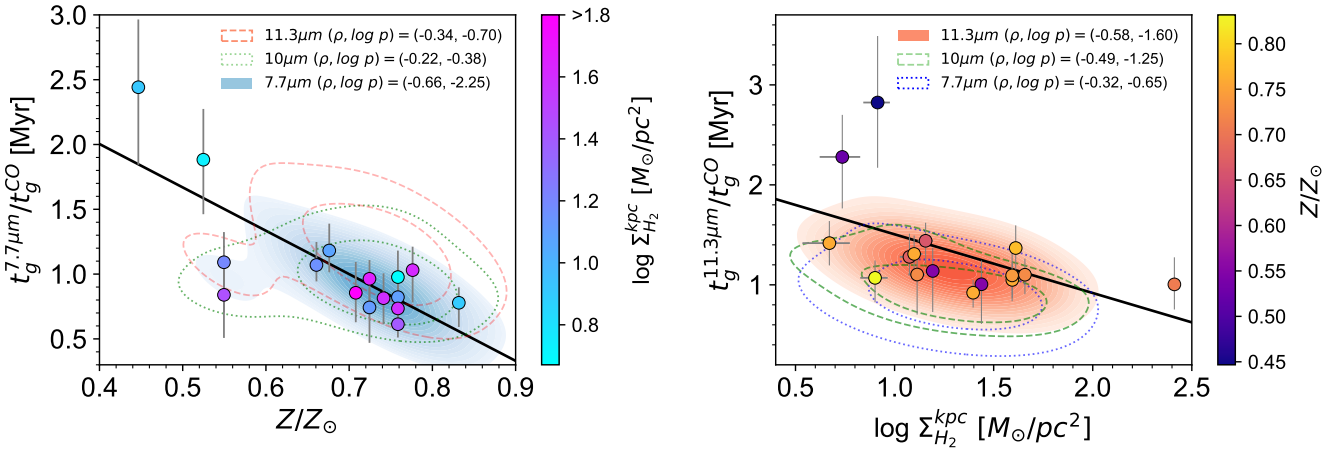

Figure 8. The ratio between the compact mid-IR emitting timescale ($t_g^{\rm mid-IR}$) and molecular gas cloud lifetime ($t_g^{\rm CO}$) shows negative trends with metallicity and molecular gas surface density, which are in line with theoretical expectations. Data points (circles) in the left panel, color-coded by molecular gas surface density, show the trend between $t_g^{7.7\,\mu m}/t_g^{\rm CO}$ and metallicity ($Z/Z_\odot$, relative to solar), which is the tightest among mid-IR bands. The solid line represents the best-fitting linear regression. The 1σ distributions of our measurements in all three mid-IR bands are shown for comparison as blue, green, and red contours for 7.7, 10, and 11.3 μm, respectively. The tightest relation is emphasized using filled contours. We also report the Spearman's correlation coefficients (ρ) and p-values in the upper-right corner. The right panel is similar to the left but instead shows the negative trend between $t_g^{11.3\,\mu m}/t_g^{\rm CO}$ and kiloparsec-scale average molecular gas surface density ($\Sigma_{\rm H_2}^{\rm kpc}$), where the data points (circles) are color-coded by $Z/Z_\odot$.

difference between the compact mid-IR and CO-bright molecular gas cloud phases. The ratio $t_g^{11.3\,\mu m}/t_g^{\rm CO}$ exceeds 2 in the two most metal-poor galaxies (NGC 5068 and NGC 2835). However, we again note that CO flux completeness is also lower for lower-metallicity and low-mass galaxies. This raises the possibility that the observed trends may be biased by the shallow CO observations, potentially missing small and faint CO clouds in these galaxies. Such incompleteness would lead to an underestimation of the CO-emitting timescale and therefore an overestimation of $t_g^{11.3\,\mu m}/t_g^{\rm CO}$.

To assess the impact of CO sensitivity, we first performed a linear regression between $t_g^{\rm mid-IR}/t_g^{\rm CO}$ and CO completeness (c). We then used the residuals to represent the timescale ratio after removing the dependence on completeness. We find that the correlation between the residuals of $t_g^{7.7\,\mu m}/t_g^{\rm CO}$ and metallicity remains intact with $\rho = -0.6$ and $\log p = -1.8$. In contrast, the trend between $t_g^{11.3\,\mu m}/t_g^{\rm CO}$ and $\Sigma_{\rm H_2}^{\rm kpc}$ disappears after accounting for the effect of completeness, which tends to be higher in galaxies with higher molecular gas surface densities. However, this approach assumes a linear dependence between $t_g^{\rm mid-IR}/t_g^{\rm CO}$ and CO flux completeness, and is limited by a small sample. As such, the result should be interpreted with caution. When the same linear-regression-based correction is applied to the correlation between $t_g^{\rm mid-IR}/t_g^{\rm CO}$ and spatial resolution, the correlation between the residuals of $t_g^{7.7\,\mu m}/t_g^{\rm CO}$ and metallicity remains comparably tight with $\rho = -0.5$. The trend between $t_g^{11.3\,\mu m}/t_g^{\rm CO}$ and $\Sigma_{\rm H_2}^{\rm kpc}$ also persists but becomes weaker with $\rho = -0.3$.

If the conversion from atomic or CO-dark molecular gas clouds to CO-bright molecular gas clouds is faster in higher-density and -metallicity environments, we also expect to observe similar trends with $t_{\rm CO-dark}^{\rm mid-IR}$. This $t_{\rm CO-dark}^{\rm mid-IR}$ is different from $t_g^{\rm mid-IR}/t_g^{\rm CO}$ in that $t_{\rm CO-dark}^{\rm mid-IR}$ only considers the duration of the compact mid-IR emitting phase that is not associated with both CO emission and Hα, while $t_g^{\rm mid-IR}/t_g^{\rm CO}$ includes the phase coincident with Hα emission (feedback phase). In Figure 9, we show the two tightest correlations observed with $t_{\rm CO-dark}^{\rm mid-IR}$. We find that $t_{\rm CO-dark}^{7.7\,\mu m}$ shows an anticorrelation with stellar mass ($M_*^{\rm glob}$) with $\rho = -0.7$, which agrees with our expectation as stellar mass correlates with metallicity. We also find that $t_{\rm CO-dark}^{10\,\mu m}$ decreases with increasing global SFR with $\rho = -0.7$. A higher SFR on global-scale indicates that there is more molecular gas with higher densities, possibly resulting in a shorter mid-IR neutral gas phase without associated CO emission. Biases in CO observation also affect $t_{\rm CO-dark}^{10\,\mu m}$, where we measure a shorter duration of isolated mid-IR phase, dark in CO for galaxies with higher CO flux completeness, as indicated by the color of the data points. The duration of the CO-dark phase obtained using other mid-IR bands shows similar trends with $M_*^{\rm glob}$ and SFR$^{\rm glob}$; however, they are weaker. Similar to $t_g^{\rm mid-IR}/t_g^{\rm CO}$ above, we obtained residuals of $t_{\rm CO-dark}^{7.7\,\mu m}$ after the dependence on CO flux completeness has been removed. The correlation between the residuals of $t_{\rm CO-dark}^{7.7\,\mu m}$ and $M_*^{\rm glob}$ remains tight with $\rho = -0.6$, while the relation between the residuals of $t_{\rm CO-dark}^{10\,\mu m}$ and SFR$^{\rm glob}$ disappears. The spatial resolution, on the other hand, more strongly affects the relation between the residuals of $t_{\rm CO-dark}^{7.7\,\mu m}$ and $M_*^{\rm glob}$ with $\rho = -0.3$. The relation between $t_{\rm CO-dark}^{10\,\mu m}$ and SFR$^{\rm glob}$ remains comparably tight with $\rho = -0.5$.

As discussed in Section 4.2, the LMC has a very low molecular gas fraction of $f_{\rm H_2} = 0.09$, sparse ISM with molecular gas surface density of $2\,M_\odot$ pc^{-2}, log SFR $= -0.7$ (K. E. Jameson et al. 2016; A. Schruba et al. 2019), and 50% of solar metallicity (L. Toribio San Cipriano et al. 2017). Using H I and CO observations, the ratio between the neutral gas cloud and molecular gas cloud lifetimes is measured to be 5, whereas $t_{\rm CO-dark}^{\rm HI}$ is $\approx$35 Myr (J. L. Ward et al. 2020, 2022). These measurements would place the LMC in the upper-left corners of Figures 8 and 9, further supporting the trends observed here. We however note that the neutral gas cloud lifetime measured in J. L. Ward et al. (2020) uses H I observations, while mid-IR emission used here does not fully capture all of the neutral ISM distribution. Indeed, when using 8 μm observations of the LMC from Spitzer (M. Meixner et al. 2006), we find the mid-IR emitting phase to be 15 Myr, resulting in a ratio of 1.5 between the mid-

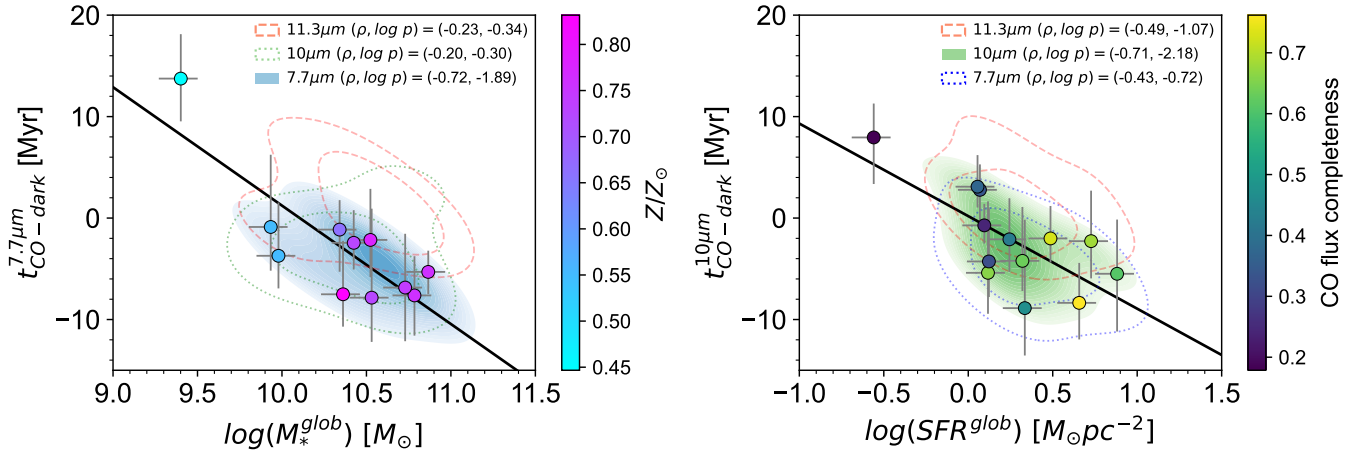

Figure 9. Similar to Figure 8, we show the trends between the duration of the mid-IR emitting phase dark in CO (and Hα) emission ($t^{\rm mid-IR}_{\rm CO-dark}$) and the galaxy stellar mass ($M^{\rm glob}_{*}$ left) and total SFR (SFR$^{\rm glob}$; right). Data points are $t^{7.7\,\mu m}_{\rm CO-dark}$ and $t^{10\,\mu m}_{\rm CO-dark}$ in the left and right panels, which are colored by the metallicity ($Z/Z_\odot$) and the completeness of CO flux observations (c), respectively. The correlation indicates that galaxies with higher metallicity and higher SFR have a negligible mid-IR emitting gas cloud phase (before the onset of star formation) that is not traced by CO, with $t^{\rm mid-IR}_{\rm CO-dark}$ being close to zero. For each mid-IR band, Spearman's correlation coefficient (ρ) and p-value are shown in the upper-right corner.

IR emitting timescale and molecular cloud lifetime, whereas the CO-dark mid-IR emitting cloud phase lasts ≈5 Myr (J. Kim et al. 2025, in preparation). These values are smaller compared to when H I is used; however, this still places the LMC along the observed trend.

5.1.2. Identification of Statistically Significant Correlations

We search for statistically strong correlations, which are determined by their associated p-values smaller than an effective p-value ($p_{\rm eff}$), defined using the Holm–Bonferroni method (S. Holm 1979; see also J. M. D. Kruijssen et al. 2019a; J. Kim et al. 2022 for astrophysical applications). This method is used when conducting a large number of hypothesis tests simultaneously, such as correlations between multiple variables, as there is an increased risk of finding spurious significant results purely by chance. The procedure is as follows. We begin by examining whether each of our measurements (row in Figure 7) correlates with any of the galaxy properties (columns in Figure 7). The correlations are ranked based on increasing p-values. For each sorted p-value with a rank i, we compare it with an effective p-value ($p_{\rm eff}$). If the p-value is smaller than $p_{\rm eff}$, we consider the correlation to be significant. The $p_{\rm eff}$ is defined as $p_{\rm ref}/(N_{\rm corr}+1-i)$, where $p_{\rm ref}$ is the desired significance level (0.05) and $N_{\rm corr}$ is the number of independent variables being compared. In order to evaluate $N_{\rm corr}$, we have correlated galaxy properties with each other and treat properties with a correlation coefficient higher than 0.7 as one metric. We found strong correlations between SFR$^{\rm glob}$ and $M^{\rm glob}_{\rm H_2}$, $M^{\rm glob}_{\rm gas}$, ΔMS, $\Sigma^{\rm kpc}_{\rm HI+H_2}$, $\Sigma^{\rm kpc}_{\rm SFR}$, $\Sigma^{\rm kpc}_{\rm H_2}$, $\Sigma^{\rm kpc}_{*}$, $P_{\rm DE}$, c, $M^{\rm GMC}$, and $\alpha^{\rm GMC}_{\rm vir}$. The galaxy stellar mass M_* also strongly correlates with Hubble T-type and $\sigma^{\rm GMC}$, resulting in $N_{\rm corr}\approx 15$. We note that if we assume all of the variables are independent with $N_{\rm corr}=28$, the correlations with $t^{\rm mid-IR}_{\rm g}$ and $f^{\rm mid-IR}_{\rm diffuse}$ are no longer defined as statistically significant.

All of the significant correlations identified according to our definition are highlighted in Figure 7. We note that these include strong correlations caused by systematic biases. For example, we find that our measurements of λ are dependent on the resolution of the data ($l_{\rm ap,min}$) regardless of the wavelength used. These biases have already been pointed out by our previous work (J. Kim et al. 2022) and imply that λ are overestimated in galaxies with a poor resolution. In the following section, we discuss strong correlations that are likely to have physical meaning behind them.

5.1.3. Interpreting the Strong Correlations

For the mid-IR emitting phase, as shown in the left panel of Figure 10, we found a strong positive correlation between $t^{10\,\mu m}_{\rm g}$ and $\epsilon_{\rm H\alpha}$. The $\epsilon_{\rm H\alpha}$ represents the flux density contrast of Hα emission peaks relative to the average flux density on a galactic scale, measured on the diffuse emission filtered map. Therefore, higher-density contrast implies that the flux distribution is sharper and that the H II regions are better defined (M. S. Oey et al. 2017) with less crowding and less structured background. Figure 10 also shows durations of mid-IR emitting phases obtained with other mid-IR bands ($t^{7.7\,\mu m}_{\rm g}$ and $t^{11.3\,\mu m}_{\rm g}$). They exhibit similar trends with log $p\approx -1.5$, which was not small enough to be considered statistically significant.

Given that a higher-density contrast in Hα emission peak implies better defined and clean H II regions, we speculate that the correlation is driven by the environments with greater density contrasts, allowing for a more efficient absorption of nonionizing far-ultraviolet photons and thus heating in the ambient PAHs and dust grains surrounding the H II regions. This will, in turn, allow the mid-IR emitting phase to continue more brightly near H II regions in the ambient medium, resulting in a longer mid-IR emitting period (e.g., A. G. Jones et al. 2015). Our interpretation is also in line with observations of M. S. Oey et al. (2017), suggesting that H II regions with a clear stratified ionization structure are associated with brighter 8μm emission compared to H II regions with structured ISM and a weak transition zone between ionized and neutral gas. Better-defined H II regions also imply a higher spatial correspondence between dust and gas to the heating source, which would lead to hotter dust and thus brighter mid-IR emission near H II regions (D. A. Dale et al. 2007). The data points in Figure 10 are color-coded by the ratio of feedback phase over Hα emitting phase ($t^{10\,\mu m}_{\rm fb}/t_{\rm s}$), suggesting that galaxies with a higher-density contrast and a longer mid-IR

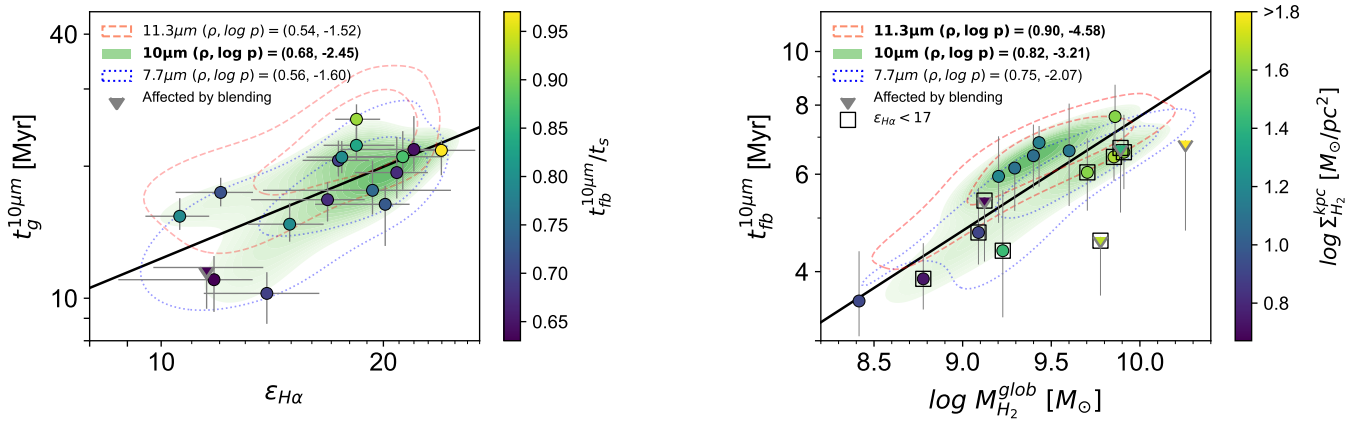

Figure 10. Strong correlations identified between our measurements of timescales and galaxy properties. The data points (circles) in the left panel shows a correlation between the 10 μm emitting timescale ($t_g^{10\,\mu m}$) as function of the flux density contrast measured between peaks and galactic average in Hα emission map ($\epsilon_{H\alpha}$). The solid line represents the best-fitting linear regression. The higher the density contrast with better-defined H II regions, the more efficient the heating of the ambient gas, allowing the mid-IR emitting phase to continue for a longer period during the Hα bright phase. This is also indicated by the color of the circles, which show higher ratios of $t_{fb}^{10\,\mu m}/t_s$ for galaxies with longer mid-IR emitting phases. The outermost contours represent the 1σ distributions of our measurements across the three mid-IR bands, shown in blue, green, and red for the 7.7, 10, and 11.3 μm bands, respectively, with the tightest relation highlighted using filled contours. Spearman's correlation coefficient and associated p-value are indicated in each panel for all mid-IR bands, where significant correlations are in boldface. Triangles represent upper limits for some galaxies that are affected by source blending (Appendix B). They are excluded in the correlation analysis. The right panel is similar to the left panel but shows the correlation between the feedback timescale ($t_{fb}^{10\,\mu m}$) and molecular gas mass ($M_{H_2}^{glob}$). Galaxies with a shorter feedback timescale have sparser ISM, as indicated by the color of data points (kiloparsec-average molecular gas surface density, $\Sigma_{H_2}^{kpc}$), which facilitates the PAH and/or dust dispersal. Galaxies with $\epsilon_{H\alpha} < 17$ (squares) also show shorter feedback timescales, which can be explained if PAHs disperse more quickly when H II regions are not well defined with structured ISM, enabling an easier escape of ionizing photons and PAH destruction near H II regions.

emission phase tend to have a higher $t_{fb}^{10\,\mu m}/t_s$ ratio. For all of the mid-IR bands, the relations between t_{fb}/t_s and $\epsilon_{H\alpha}$ reveal suggestive positive correlations with their coefficients ranging from 0.5–0.7 (see Figure 7).

In the right panel of Figure 10, we show a strong positive correlation between $t_{fb}^{10\,\mu m}$ and $M_{H_2}^{glob}$. The correlation with M_{gas}^{glob} is also found to be significant; however, we show only the relation with $M_{H_2}^{glob}$ here to avoid redundancy. In our analysis with 11.3 μm, the same correlations with M_{HI}^{glob} and M_{gas}^{glob} were found to be significant (see Figure 7) with their distributions similar to 10 μm. The $t_{fb}^{11.3\,\mu m}$ also shows strong correlations with SFR^{glob} and M_{HI}^{glob}. For 7.7 μm, the same correlations were not characterized as significant with log $p = -2.1$.

The strong correlation between $t_{fb}^{10\,\mu m}$ and $M_{H_2}^{glob}$ suggests that low-mass galaxies have a shorter feedback timescale. This can be attributed to the low gas surface density and therefore lower midplane pressure of low-mass galaxies, which allows gas to be dispersed more quickly by stellar feedback. Low-mass galaxies also have low gravitational potentials, enabling a faster gas ejection from the galactic disk (O. Agertz et al. 2020). In addition, similar to the relationship between $t_g^{10\,\mu m}$ and $\epsilon_{H\alpha}$, galaxies with smaller density contrast in H II regions $\epsilon_{H\alpha} < 17$ appear to have shorter feedback timescales. In an environment with lower-density contrasts and thus not well-defined H II regions with structured ISM distribution, it would be easier for ionizing photons to escape, leading to a faster PAH (or dust) dispersal and shorter feedback timescales. However, in a high-density contrast environment with clean H II regions, photons more efficiently illuminate the surrounding shells of material in mid-IR, resulting in a longer overlap between Hα and mid-IR at scales of 50–150 pc. As discussed in Section 4.3, at this scale, the spatial offset between Hα peak and the surrounding shells of ISM emitting in mid-IR emission is not spatially resolved, resulting in a long overlap timescale between the two phases. If the spatial offset can be resolved, we expect to measure a shorter overlapping timescale.

Finally, as shown in Figure 11, we found correlations with diffuse emission fraction, where $f_{diffuse}^{7.7\,\mu m}$ shows a strong anticorrelation with the galaxy gas fraction (f_{gas}^{glob}) and $f_{diffuse}^{11.3\,\mu m}$ correlates with the average velocity dispersion of GMCs (σ^{GMC}). The anticorrelation with f_{gas}^{glob} indicates that galaxies with higher gas fraction, which tend to have a more irregular galaxy morphology (color of data points), have a lower diffuse emission fraction measured in 7.7 μm. Other mid-IR bands also exhibit similar trends, where $f_{diffuse}^{11.3\,\mu m}$ is strongly anticorrelated with morphology T-type (see Figure 7). This trend may arise because mid-IR emission from spurs within spiral arms are filtered out and excluded from our analysis, except for the bright knots located within them. This results in a higher diffuse emission fraction for galaxies with a distinct spiral arm structure. The correlation between $f_{diffuse}^{11.3\,\mu m}$ and σ^{GMC} can be explained if more turbulent clouds allow photons to travel farther outside the star-forming region, resulting in a larger fraction of diffuse emission. We, however, note that a higher diffuse emission fraction is measured for some galaxies with a coarser resolution, as indicated by the color, potentially biasing the correlation.

5.1.4. Trends with the Difference in the Feedback Timescale Measured with Mid-IR versus CO

As discussed in Section 4.3, across all of the galaxies and mid-IR bands, we find that the Hα overlap timescale measured with mid-IR is longer than that obtained using CO emission as the gas tracer. While not characterized as statistically significant according to our definition, in Figure 12, we show the two strongest correlations obtained with the difference between the two feedback timescales ($\Delta t_{fb,CO}^{mid-IR}$). We find that $\Delta t_{fb,CO}^{11.3\,\mu m}$ shows a suggestive trend with the molecular gas

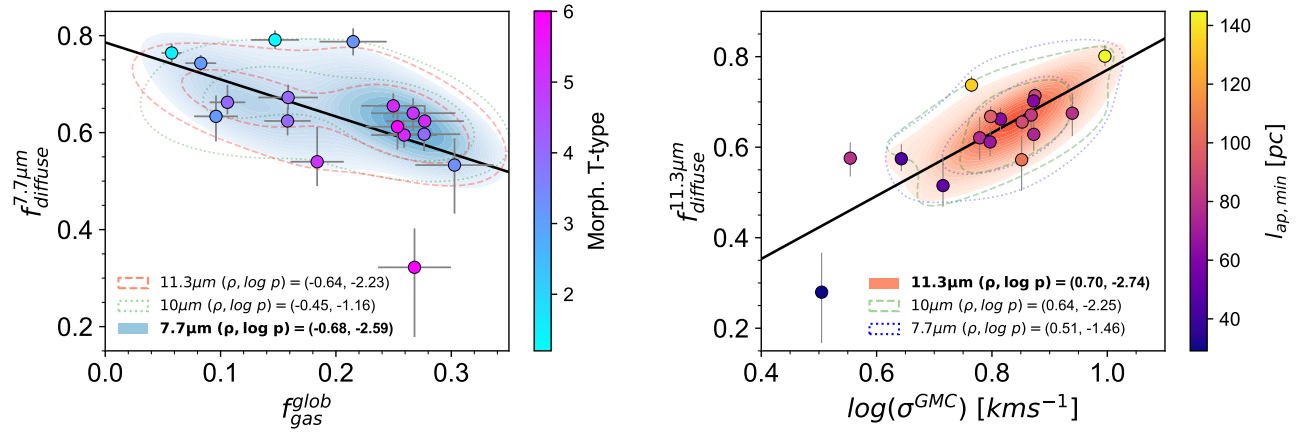

Figure 11. Similar to Figure 10, we show strong correlations found with diffuse emission fractions. The left panel shows the anticorrelation between $f_{\rm diffuse}^{7.7\,\mu{\rm m}}$ and gas fraction ($f_{\rm gas}^{\rm glob}$), where the data points are color-coded by the Hubble morphology T-type. The correlation suggests that diffuse emission in mid-IR increases for galaxies with a low gas fraction and well-defined spiral arm structure. The right panel shows the correlation between $f_{\rm diffuse}^{11.3\,\mu{\rm m}}$ and the average velocity dispersion of GMCs ($\sigma^{\rm GMC}$), implying that more turbulent clouds lead to higher diffuse emission fraction in mid-IR. However, we note the possibility of resolution biasing the correlation as indicated by the color of the data point, demonstrating that diffuse emission fraction is higher for galaxies with a coarser resolution.

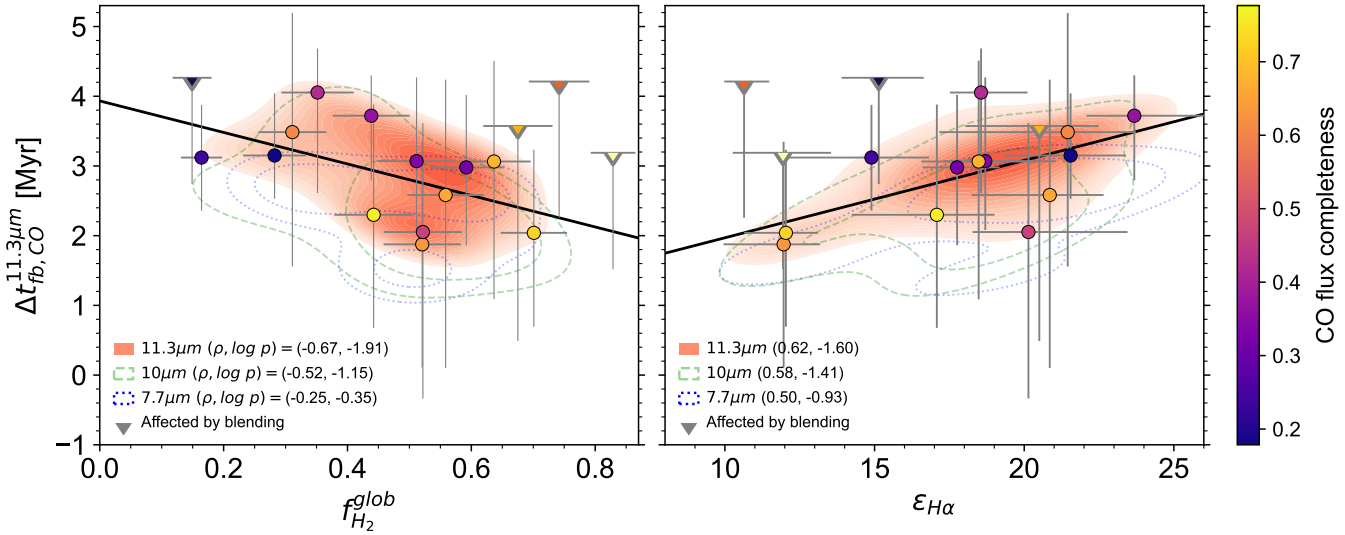

Figure 12. Similar to Figure 10, we show suggestive trends of the difference in feedback timescales obtained with mid-IR and CO emission ($\Delta t_{\rm fb,CO}^{11.3\,\mu{\rm m}}$), as a function of the molecular gas fraction ($f_{\rm H_2}^{\rm glob}$; left panel) and the density contrast measured in Hα emission map ($\epsilon_{\rm H\alpha}$; right panel). The data points are colored based on the CO flux completeness.

fraction ($f_{\rm H_2}^{\rm glob}$) and flux density contrast measured in Hα map ($\epsilon_{\rm H\alpha}$) with $\log p < -1.5$. In other mid-IR bands, both relations become weaker.

The $\Delta t_{\rm fb,CO}^{11.3\,\mu{\rm m}}$ is longer in galaxies with a lower molecular gas fraction, which can be explained if, in atomic-gas-dominated galaxies, CO emission goes under the detection limit faster during the cloud dispersal compared to the mid-IR emission. The CO flux completeness is also low in these galaxies, as indicated by the color of the points. Interestingly, we find a longer $\Delta t_{\rm fb,CO}^{11.3\,\mu{\rm m}}$ for galaxies with a higher $\epsilon_{\rm H\alpha}$. This is similar to the trend in the left panel of Figure 10, suggesting that photons coming from well-defined H II regions are more efficient in illuminating the surrounding neutral ISM material, while the CO emission has already dispersed. This implies that mid-IR emission persists in star-forming regions and is related to the ISM distribution around H II regions. We note that after removing the dependence of CO flux completeness on $\Delta t_{\rm fb,CO}^{11.3\,\mu{\rm m}}$ via linear regression, the correlation of $\Delta t_{\rm fb,CO}^{11.3\,\mu{\rm m}}$ with molecular gas fraction weakens from $\rho = -0.7$ to $\rho = -0.3$ and the correlation with $\epsilon_{\rm H\alpha}$ weakens from $\rho = 0.6$ to $\rho = 0.4$. The $\Delta t_{\rm fb,CO}^{11.3\,\mu{\rm m}}$ does not show trends with resolution (Figure 7), and the observed trends remain unchanged after removing any potential resolution dependence using the same linear-regression-based approach.

5.2. Galaxies with Decorrelation between CO and Mid-IR Emission

As shown in Figure 4, the mid-IR emitting phase typically spans the entire CO-emitting phase in most galaxies. This is consistent with expectations, as molecular gas forms from compact neutral ISM structures (e.g., P. C. Clark et al. 2012), before star formation takes place. However, we found some exceptions that contradict physical expectations, NGC 1566 and NGC 4321, where the CO-emitting phase begins earlier than the mid-IR emitting phase, particularly when 7.7 μm is used. This implies that there is a substantial decorrelation

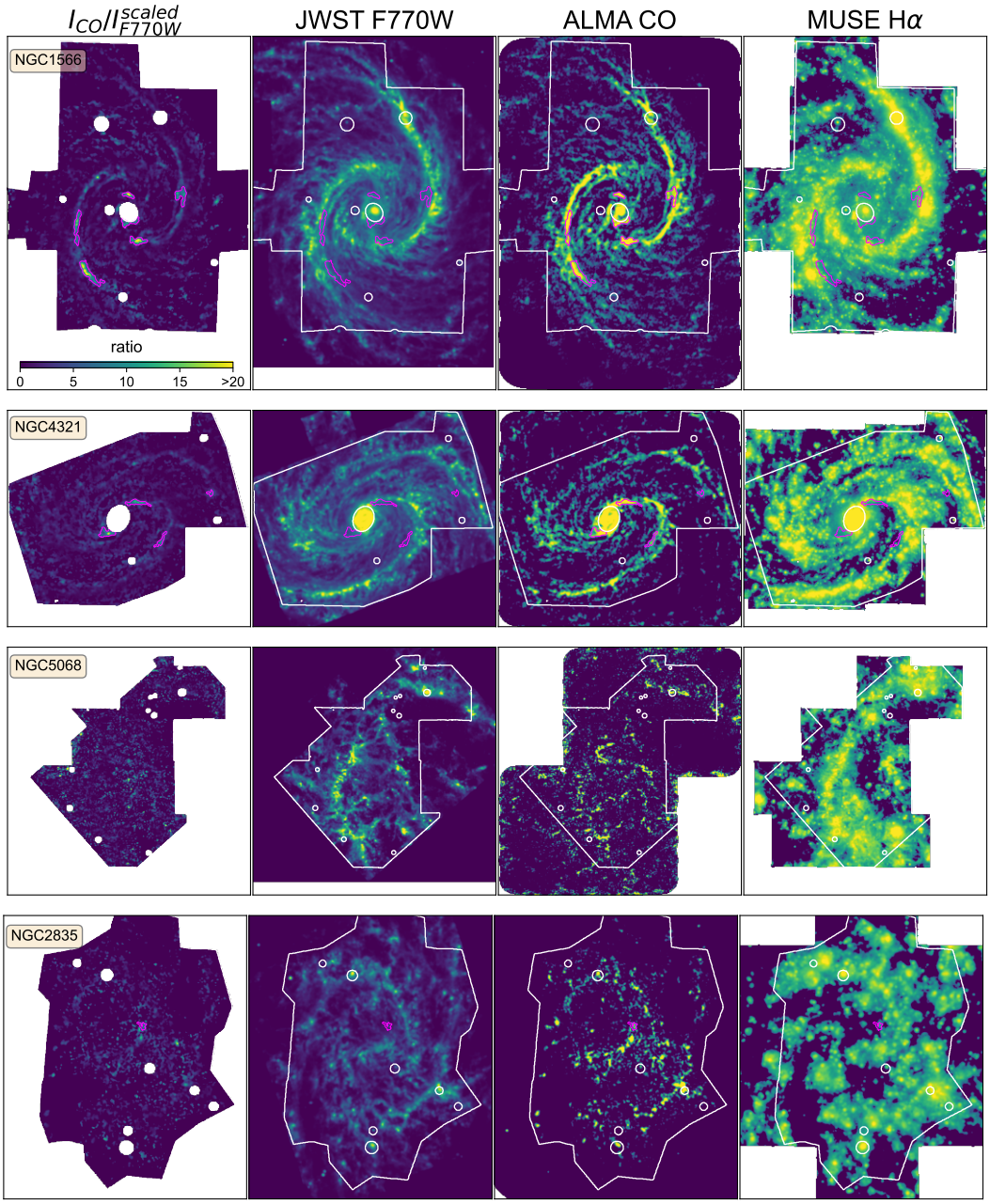

Figure 13. Galaxies with the most negative $t_{\mathrm{CO-dark}}^{7.7\,\mu\mathrm{m}}$ have molecular gas ridges with unusually high CO-to-PAH flux ratios (magenta in top two rows; NGC 1566 and NGC 4321), indicating that the tight correlation between F770W and CO flux is broken. This leads to an isolated CO-emitting phase before the onset of mid-IR emitting phase. The first column shows the ratio of CO flux (I_{CO}) to that expected from F770W flux ($I_{\mathrm{F770W}}^{\mathrm{scaled}}$), using the correlation from R. Chown et al. (2025). The ridges with flux ratio higher than 5 and bigger than 10 times the N_{pix} are highlighted in magenta. The solid white polygon indicates our analysis region, and the circle shows the masked emission peaks (see Section 3). We also show F770W, CO, and Hα observations in each column. For comparison, galaxies with the most positive $t_{\mathrm{CO-dark}}^{7.7\,\mu\mathrm{m}}$ are shown in the two bottom rows, where we do not identify significant ridges with unusual flux ratios.

between CO and mid-IR emission in these galaxies, resulting in a negative $t_{\mathrm{CO-dark}}^{\mathrm{mid-IR}}$.

Figure 13 shows the ratio of CO flux (I_{CO}) and that expected from F770W emission ($I_{\mathrm{F770W}}^{\mathrm{scaled}}$), based on the correlation from R. Chown et al. (2025). Mid-IR observations used in Figure 13 are described in Section 2, whereas the CO data is from PHANGS-ALMA (A. K. Leroy et al. 2021a). We note that these are not diffuse emission filtered. Contours highlight ridges with flux ratios ($I_{\mathrm{CO}}/I_{\mathrm{F770W}}^{\mathrm{scaled}}$) higher than 5 and with their size at least 10 times larger than the minimum emission peak size, $N_{\mathrm{pix,min}}$ (see Table 2). Notably, NGC 1566 and NGC 4321, which have the most negative $t_{\mathrm{CO-dark}}^{7.7\,\mu\mathrm{m}}$ ($-7.6^{+3.9}_{-4.0}$ and a range from -11.9 to -3.4, respectively) show long ridges that deviate from the tight correlation observed between F770W and CO flux (R. Chown et al. 2025). These regions, with unusually high CO-to-PAH flux ratios, do not coincide with H II regions, indicating that the lack of PAH emission is not due to massive stars dissociating PAHs (O. V. Egorov et al. 2023; J. Sutter et al. 2024). They are also preferentially located in dynamically complex areas, like concave parts of spiral arms, bar ends, and central rings. These two galaxies (NGC 1566 and NGC 4321) and NGC 1365 are the only galaxies in our sample that exhibit these long ridges with unusual flux ratios, while other galaxies show none or only one

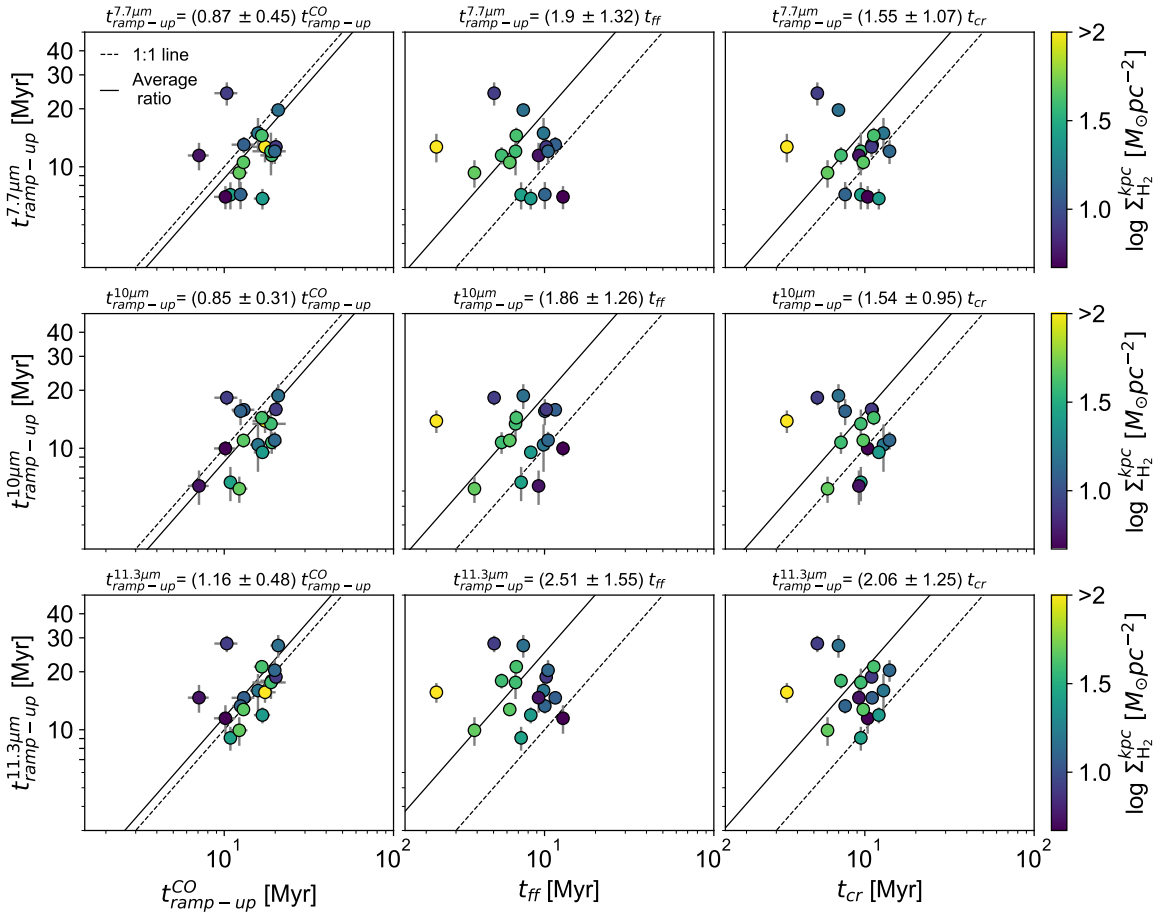

Figure 14. The time from neutral gas cloud formation to the onset of star formation traced with mid-IR (ramp-up timescale; $t^{\rm mid-IR}_{\rm rampup}$) is compared to that measured with CO ($t^{\rm CO}_{\rm rampup}$), as well as to analytical predictions from J. Sun et al. (2022), which are related to the dynamics within clouds (GMC freefall and turbulence crossing timescales; $t_{\rm ff}$ and $t_{\rm cr}$, respectively). Data points are color-coded by molecular gas surface density ($\Sigma^{\rm kpc}_{\rm H_2}$). The average and 1σ range of the ratio of two timescales are shown in each panel. The solid line shows the average ratio between the timescales, and a one-to-one relation is shown as the dashed line. We find the best agreement between $t^{\rm mid-IR}_{\rm rampup}$ and $t^{\rm CO}_{\rm rampup}$, whereas the ramp-up timescale measured with mid-IR is somewhat longer than $t_{\rm ff}$ and $t_{\rm cr}$.

or two small regions. For comparison, we also show NGC 5068 and NGC 2835, which are two galaxies with the longest $t^{\rm mid-IR}_{\rm CO-dark}$ and follow the observed correlation between CO and mid-IR well without significant outliers.

There are multiple potential explanations for the long ridges with anomalous CO-to-PAH ratios. One possibility is a very low UV radiation field, which could suppress PAH excitation. However, given their location, it seems unlikely that these ridges are particularly in well-shielded regions. Another explanation could be that CO emissivity is substantially higher in these ridges, possibly due to large-scale streaming motions changing the opacity (Y.-H. Teng et al. 2023), as these ridges are situated along the bar ends and edges of spiral arms. Lastly, it could be that PAH emission in the 7.7–11.3 μm bands has been suppressed, potentially due to PAH dissociation from large-scale shocks, or because PAHs are growing in size or even sticking onto other dust grains via accretion and coagulation (B. T. Draine et al. 2021; B. S. Hensley & B. T. Draine 2023). To investigate this, we have used stellar continuum-subtracted 3.3 μm imaging from H. Koziol et al. (2025, in preparation) and K. M. Sandstrom et al. (2023b) to measure the 3.3 μm/11.3 μm and 11.3 μm/7.7 μm flux ratios. We found that PAHs in these ridges appear to be larger (lower 3.3 μm/11.3 μm ratio) and more neutral (higher 11.3 μm/7.7 μm ratio), which supports the idea of coagulation. However, these ratios are degenerate with PAH properties, and further spectroscopic observations such as those covering H_2 rotational and rovibrational lines, shock tracers like [Fe II], and various PAH features are needed to confirm these speculations.

5.3. Comparison with Characteristic Timescales

The measured mid-IR emitting phase can be divided into two stages: the quiescent ramp-up phase, associated with mid-IR emission before the onset of massive star formation detected in Hα ($t^{\rm mid-IR}_{\rm ramp-up} = t^{\rm mid-IR}_{\rm g} - t^{\rm mid-IR}_{\rm fb}$) and the mid-IR and H$\alpha$ emission overlapping phase ($t^{\rm mid-IR}_{\rm fb}$). Using CO observations, the ramp-up period has been measured to be ~5–20 Myr and is comparable to the gravitational freefall or turbulence crossing timescales of GMCs (E. Corbelli et al. 2017; J. Kim et al. 2021, 2023; E. Schinnerer & A. K. Leroy 2024). In Figure 14, we compare the duration of the ramp-up phase measured with mid-IR to that constrained with CO ($t^{\rm CO}_{\rm ramp-up}$), as well as analytical predictions of GMC freefall and turbulence crossing times ($t_{\rm ff}$ and $t_{\rm cr}$), which are mass-weighted harmonic averages from J. Sun et al. (2022). The compact mid-IR emitting gas clouds experience a ramp-up period of 5–30 Myr, showing the best agreement with $t^{\rm CO}_{\rm ramp-up}$ measured in J. Kim et al. (2022). Gas

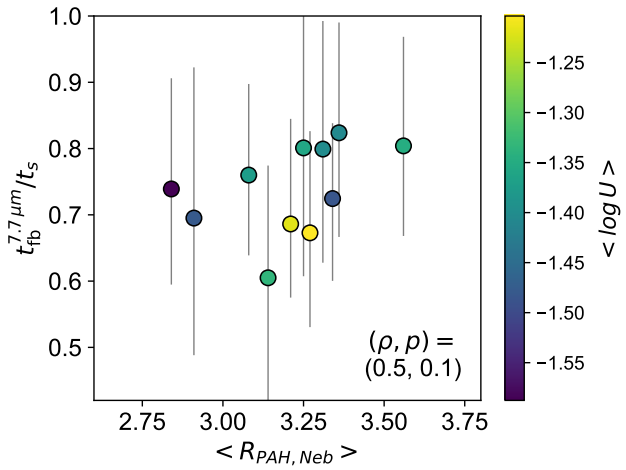

Figure 15. The fraction of the Hα emitting phase associated with 7.7 μm emission ($t_{\rm fb}^{7.7\,\mu{\rm m}}/t_s$) as a function of the average PAH abundance in H II regions ($<R_{\rm PAH,Neb}>$ J. Sutter et al. 2024). Data points are color-coded by the average ionization parameter ($<\log U>$), which is the ratio between ionizing photon flux and the hydrogen density in H II regions from B. Groves et al. (2023). Spearman's correlation coefficient and the associated p-value are also indicated. The 7.7 μm shows the strongest correlations, while other bands show weaker relations.

clouds with lower molecular gas surface densities, indicated by the color of the data points, show a good agreement between $t_{\rm ramp-up}^{\rm mid-IR}$ and the GMC freefall timescale. However, the overall agreement between $t_{\rm ramp-up}^{\rm mid-IR}$ and $t_{\rm cr}$ is better than with $t_{\rm ff}$.

5.4. PAH Abundance and Feedback Duration

For the feedback timescale, we find that mid-IR emission remains strongly associated with Hα emission, with its duration covering 60%–90% of the total Hα emitting phase. This overlap period is likely to be dependent on various factors, including PAH destruction by ionizing photons, ISM heating, and reshaping of the surrounding dust reservoir. While PAH destruction within H II regions would shorten the feedback phase, PAHs would glow more brightly near areas where massive stars have recently formed, prolonging the measured timescale.

In Figure 15, we show a relationship between the fraction of Hα emitting phase associated with 7.7 μm emission ($t_{\rm fb}^{7.7\,\mu{\rm m}}/t_s$) and the average PAH abundance of H II regions ($R_{\rm PAH,Neb}$) from J. Sutter et al. (2024). Among other mid-IR bands, 7.7 μm shows the strongest relation. The $R_{\rm PAH,Neb}$ is estimated using a combination of JWST filters ([F770W+F1130W]/F2100W), which are known to trace the fraction of dust in the form of PAHs by mass (J. Chastenet et al. 2023; O. V. Egorov et al. 2023). We find a moderate positive relationship between $t_{\rm fb}^{7.7\,\mu{\rm m}}/t_s$ and $R_{\rm PAH,Neb}$, indicating that a lack of PAHs leads to a shorter overlap between mid-IR and Hα. The data points are color-coded according to the ionization parameter, which is estimated in B. Groves et al. (2023) using the prescription of A. I. Diaz et al. (1991). This ionization parameter is related to the ratio of the density of ionizing photons to the number density of hydrogen atoms in the gas. We use Hα luminosity weighted averages. For the two galaxies with higher ionization parameters, the overlap period appears to be shorter. This could be due to the more intense ionizing radiation field destroying PAHs, rather than exciting them and allowing PAHs to illuminate more brightly near H II regions. However, we note that we are only comparing a single average value for each galaxy, while there are likely wide variations in both PAH abundance and the radiation field within each galaxy. For example, O. V. Egorov et al. (2023, in preparation) found a strong anticorrelation between PAH abundances and ionization parameter for individual H II regions. In future studies, it would be valuable to explore the distribution of these parameters, rather than relying on single average values. By considering the full range of parameter values, such as the variation in PAH abundances and ionization parameters across different regions within each galaxy, we would gain a more comprehensive understanding of the processes at play.

6. Conclusions

Leveraging PHANGS-JWST Cycle 1 and PHANGS-MUSE observations, we present timescales of PAH (7.7 and 11.3 μm) and dust continuum (10 μm) emission of gas clouds for 17 galactic disks (excluding centers), by applying the statistical method developed by J. M. D. Kruijssen & S. N. Longmore (2014) and J. M. D. Kruijssen et al. (2018). Assuming that mid-IR emission (7.7–11.3 μm) traces the gas column density, this enables us to translate relative spatial distributions of mid-IR and Hα emission into their underlying timescales, evolving from the mid-IR emitting gas cloud phase to exposed young stellar H II regions. For each mid-IR band, we provide constraints on the mid-IR emitting timescale ($t_{\rm g}^{\rm mid-IR}$), the PAH and/or dust feedback timescale (the period during which mid-IR and Hα are coincident; $t_{\rm fb}^{\rm mid-IR}$), and the average distance between independent star-forming regions ($\lambda^{\rm mid-IR}$). We also determine additional physical quantities such as the fraction of mid-IR emitting phase with associated Hα ($t_{\rm fb}^{\rm mid-IR}/t_{\rm g}^{\rm mid-IR}$), fraction of the H$\alpha$ emitting phase with associated mid-IR emission ($t_{\rm fb}^{\rm mid-IR}/t_{\rm s}$), feedback timescale difference between mid-IR versus CO ($\Delta t_{\rm fb,CO}^{\rm mid-IR}$), duration of the mid-IR emitting gas cloud phase dark in CO (and Hα) emission ($t_{\rm CO-dark}^{\rm mid-IR}$), and diffuse emission fractions ($f_{\rm diffuse}^{\rm mid-IR}$ and $f_{\rm diffuse}^{\rm H\alpha}$). We have correlated these measurements with global galaxy and average GMC properties, as well as observational biases. We found several statistically significant correlations, allowing us to infer physical mechanisms that are responsible for the mid-IR emission.

Our key findings are as follows:

1. Across our sample, we find that the mid-IR emitting timescale ranges from 10–30 Myr across all of the mid-IR bands. The average and 1σ range are 18 $\pm$ 5, 18 $\pm$ 4, and 23 $\pm$ 5 Myr for the 7.7, 10, and 11.3 μm, respectively. On average, the mid-IR emitting timescales of gas clouds are 1–1.3 times the GMC lifetime measured in J. Kim et al. (2022), encompassing the CO-emitting phase in most galaxies. The duration of the mid-IR emitting gas cloud phase not detected in CO (and Hα) emission is nearly nonexistent with an average and 1σ range of $t_{\rm CO-dark}^{\rm mid-IR}$ being -3 ± 6, -2 ± 5, and 3 ± 5 Myr for the 7.7 μm, 10 μm, and 11.3 μm, respectively. This very short duration is most likely due to the fact that our observations are focused on the central part of the galaxy, where most of the gas is already in the molecular gas phase showing a tight correlation between mid-IR and CO emission (R. Chown et al. 2025).

2. For all of the mid-IR bands, the Hα overlap phase or feedback timescales for PAH and/or dust grain dispersal ranges from 3–7 Myr across our sample, with an average and 1σ range of 6 $\pm$ 1 Myr. This constitutes, on average, 30% of the mid-IR emitting timescale. The feedback timescale covers a significant fraction of the Hα emitting phase with an average of $t_{\rm fb}/t_{\rm s} = 70\%$–$80\%$ across mid-IR bands. We find that the feedback timescale with mid-IR is always longer than the timescale obtained with CO, with an average difference of $\Delta t_{\rm fb,CO} = 2$–3 Myr, across all mid-IR bands. The difference between mid-IR and CO is likely due to the fact that PAH and dust continuum emission is enhanced near H II regions by the intense radiation from young stars, while CO is dispersed quickly. Star-forming regions undergoing independent evolution from gas to stars are separated by 110–130 pc on average.
3. The diffuse emission fraction in mid-IR observations ranges from 30%–70%, with an average and a standard deviation of 60% $\pm$ 10%. As for the Hα maps, we measure diffuse emission fraction to range from 40%–60%. These fractions show a good agreement with the fraction of mid-IR and ionized gas emission outside H II regions (F. Belfiore et al. 2022; D. Pathak et al. 2024).
4. We find that the ratio between mid-IR emitting timescale and molecular gas cloud lifetime ($t_{\rm g}^{\rm mid-IR}/t_{\rm g}^{\rm CO}$) decreases with increasing metallicity and molecular gas surface density, in agreement with theoretical expectations where the conversion from atomic to molecular gas is expected to be faster in such environments. Similarly, the CO-dark mid-IR emitting gas cloud phase ($t_{\rm CO-dark}^{\rm mid-IR}$) shows the tightest correlations with stellar mass ($M_*^{\rm glob}$) and global SFR (SFR$^{\rm glob}$).
5. We identify several statistically significant correlations between our measurements and galaxy environmental properties. For the mid-IR emitting timescale (particularly $t_{\rm g}^{10\,\mu{\rm m}}$), we find a strong positive correlation with $\epsilon_{\rm H\alpha}$, which is the average flux density contrast measured in the Hα map, between the peak and galactic average. The correlation can be explained if cleanly defined H II regions without structured ISM (larger $\epsilon_{\rm H\alpha}$) allow photons to heat the surrounding ISM more efficiently, enabling the mid-IR emitting phase to continue for a longer period.
6. The Hα overlap timescales obtained with 10 μm and 11.3 μm ($t_{\rm fb}^{10\,\mu{\rm m}}$ and $t_{\rm fb}^{11.3\,\mu{\rm m}}$, respectively) show a strong correlation with galaxy atomic gas mass ($M_{\rm HI}^{\rm glob}$) and the total neutral gas mass ($M_{\rm gas}^{\rm glob}$). This can be understood if the sparser ISM of low-mass galaxies and their low gravitational potential facilitate a faster dispersal of PAHs and/or dust grains.
7. We find that the diffuse emission fraction measured in 7.7 μm ($f_{\rm diffuse}^{7.7\,\mu{\rm m}}$) is higher in galaxies with a low gas fraction ($f_{\rm gas}^{\rm glob}$) and with well-defined spiral arm structures. We suspect this is due to the diffuse emission located between the arms (known as spurs), as only the star-forming knots and gas clumps within the structure are considered compact. For $f_{\rm diffuse}^{11.3\,\mu{\rm m}}$, we find that galaxies with more turbulent molecular clouds, characterized by a high velocity dispersion ($\sigma^{\rm GMC}$), exhibit a higher diffuse emission fraction.
8. While not statistically significant, we note two tentative correlations detected with $\Delta t_{\rm fb,CO}^{11.3\,\mu{\rm m}}$. The $\Delta t_{\rm fb,CO}^{11.3\,\mu{\rm m}}$ becomes longer in galaxies with a low molecular gas fraction (and therefore a low CO flux completeness). This occurs because CO emission falls below the detection limit faster than the mid-IR during the feedback phase. However, another suggestive trend with $\epsilon_{\rm H\alpha}$ suggests that $\Delta t_{\rm fb,CO}^{11.3\,\mu{\rm m}}$ may have physical implications as well. Specifically, $\Delta t_{\rm fb,CO}^{11.3\,\mu{\rm m}}$ increases with higher $\epsilon_{\rm H\alpha}$. This may be interpreted as photons from star-forming regions continuing to illuminate the surrounding ISM even after CO has dissociated in regions with a high $\epsilon_{\rm H\alpha}$.
9. We identified galaxies (such as NGC 1566 and NGC 4321) with long CO-bright ridges where CO and mid-IR emission decorrelates with unusually high CO-to-PAH flux ratios. In these galaxies, there is an isolated CO-emitting phase before the mid-IR emission phase begins, leading to a negative $t_{\rm CO-dark}^{\rm mid-IR}$.
10. Finally, the mid-IR emitting phase is divided into two stages: the quiescent ramp-up phase before massive star formation, and the overlapping phase with mid-IR and Hα emission. The ramp-up period, measured with mid-IR, is found to be $\sim$5–30 Myr, comparable to the ramp-up period measured with CO (J. Kim et al. 2022). For gas clouds in a low-density environment, ramp-up periods, measured with mid-IR, show a good agreement with GMC freefall timescale (J. Sun et al. 2022).

Building on our previous measurements of the GMC lifecycle across 54 galaxies, we have extended the timeline for a subsample of 17 galaxies by incorporating mid-IR (PAH and dust continuum) emission as a probe for gas distribution. In the future, we aim to expand this analysis to the full 54 galaxies using PHANGS-JWST Cycle 2 data. The small difference observed between the mid-IR emitting timescale of gas clouds and the molecular gas cloud lifetimes is likely due to the fact that most of the gas in our sample is in the CO-bright molecular phase. Additionally, we find that radiation from star-forming regions as well as the shape of the ISM around the H II regions plays a key role in mid-IR emission. Extending this analysis to a wider range of environments with low metallicity and low gas surface density would help determine whether the timescales measured with mid-IR and CO differ.

Acknowledgments

We thank the anonymous referee for providing helpful comments, which improved the quality of the manuscript. This work was carried out as part of the PHANGS collaboration. This work is based on observations made with the NASA/ESA/CSA JWST. Support for program No. 2107 was provided by NASA through a grant from the Space Telescope Science Institute, which is operated by the Association of Universities for Research in Astronomy, Inc., under NASA contract NAS 5-03127.

J.K. is supported by a Kavli Fellowship at the Kavli Institute for Particle Astrophysics and Cosmology (KIPAC).

M.C. and L.R. gratefully acknowledge funding from the DFG through an Emmy Noether Research Group (grant No. CH2137/1-1). COOL Research DAO (M. Chevance et al. 2025) is a Decentralized Autonomous Organization supporting

research in astrophysics aimed at uncovering our cosmic origins.

K.K. gratefully acknowledges funding from the Deutsche Forschungsgemeinschaft (DFG, German Research Foundation) in the form of an Emmy Noether Research Group (grant No. KR4598/2-1, PI Kreckel) and the European Research Council's starting grant ERC StG-101077573 ("ISM-METALS").

R.S.K. and S.C.O.G. acknowledge financial support from the European Research Council via the ERC Synergy grant "ECOGAL" (project ID 855130), from the German Excellence Strategy via the Heidelberg Cluster of Excellence (EXC 2181 - 390900948) "STRUCTURES," and from the German Ministry for Economic Affairs and Climate Action in project "MAINN" (funding ID 50OO2206). R.S.K. also thanks the 2024/25 Class of Radcliffe Fellows for highly interesting and stimulating discussions.

O.E. acknowledges funding from the Deutsche Forschungsgemeinschaft (DFG, German Research Foundation)—project-ID 541068876.

K.G. is supported by the Australian Research Council through the Discovery Early Career Researcher Award (DECRA) Fellowship (project No. DE220100766) funded by the Australian Government.

I.P. acknowledges funding by the European Research Council through ERC-AdG SPECMAP-CGM, GA 101020943.

J.S. acknowledges support by the National Aeronautics and Space Administration (NASA) through the NASA Hubble Fellowship grant HST-HF2-51544 awarded by the Space Telescope Science Institute (STScI), which is operated by the Association of Universities for Research in Astronomy, Inc., under contract NAS 5-26555.

E.W.R. acknowledges the support of the Natural Sciences and Engineering Research Council of Canada (NSERC), funding reference No. RGPIN-2022-03499 and the support of the Canadian Space Agency (23JWGO2A07).

This paper makes use of the following ALMA data, which have been processed as part of the PHANGS-ALMA survey: ADS/JAO.ALMA#2012.1.00650.S, ADS/JAO.ALMA#2013.1.01161.S, ADS/JAO.ALMA#2015.1.00925.S, ADS/JAO.ALMA#2015.1.00956.S, ADS/JAO.ALMA#2017.1.00392.S, ADS/JAO.ALMA#2017.1.00886.L, ADS/JAO.ALMA#2018.1.01651.S. ALMA is a partnership of ESO (representing its member states), NSF (USA), and NINS (Japan), together with NRC (Canada), NSC and ASIAA (Taiwan), and KASI (Republic of Korea), in cooperation with the Republic of Chile. The Joint ALMA Observatory is operated by ESO, AUI/NRAO, and NAOJ. The National Radio Astronomy Observatory is a facility of the National Science Foundation operated under cooperative agreement by Associated Universities, Inc.

Facilities: JWST, VLT:Yepun, ALMA.

Software: Astropy (Astropy Collaboration et al. 2013, 2018, 2022), Clumpfind (J. P. Williams et al. 1994), Heisenberg (J. M. D. Kruijssen et al. 2018), Matplotlib (J. D. Hunter 2007), SciPy (P. Virtanen et al. 2020), seaborn (M. L. Waskom 2021), pandas (W. McKinney 2010).

Appendix A
Full Sample Three-color Images

In Figures 16–31, we show three-color composite images as well as distributions of identified emission peaks across our galaxy sample. We exclude NGC 0628 here, which is shown in Figure 1.

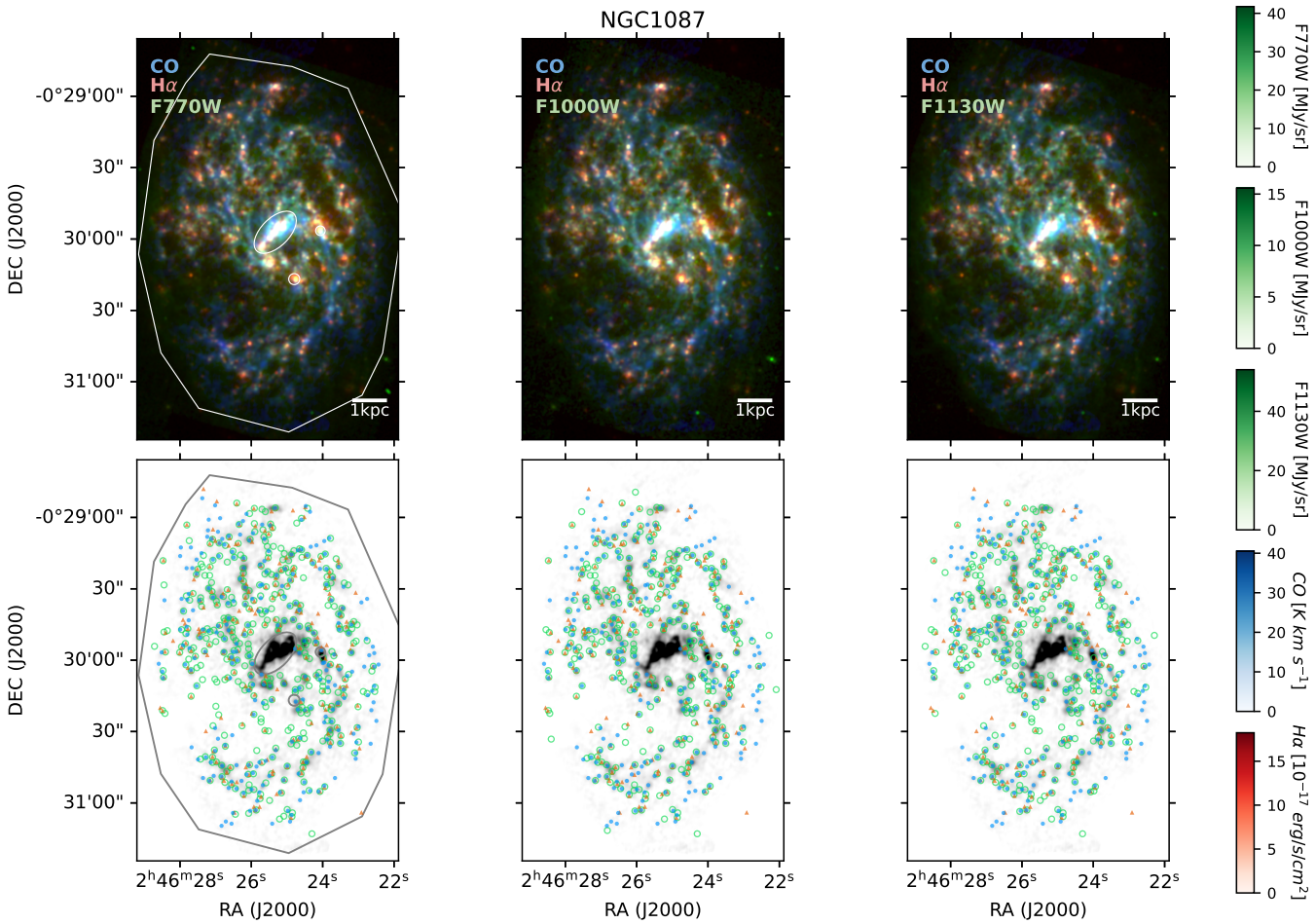

Figure 16. Top panels: composite three-color images of NGC 1087 created using CO (blue), Hα (red), and mid-IR (green) observations. Each panel, from left to right, represents mid-IR emission of F770W, F1000W, and F1130W, respectively. The mid-IR observations have been convolved and regridded to match the coarser resolution and pixel grid of Hα observations (see Section 2.3). For visualization purposes, a power-law brightness scale with gamma correction ($\gamma = 2$) has been applied in the top panels. The color bars on the right reflect the true flux ranges in each observation. The left panel highlights the area analyzed, outlined by a polygon. It excludes the crowded galactic center (ellipse) as well as artifacts and exceptionally bright peaks (circles). Bottom panels: locations of identified Hα (orange triangles), CO (blue filled circles), and mid-IR (green open circles) emission peaks (see Section 3) are overlaid on the CO map, shown in grayscale with a linear brightness scale. Again, from left to right, the mid-IR emission peaks correspond to peaks identified in F770W, F1000W, and F1130W maps, respectively. The CO grayscale image uses the same intensity range as the CO emission in the top panels shown in blue, with a range of flux indicated in the color bar on the right.

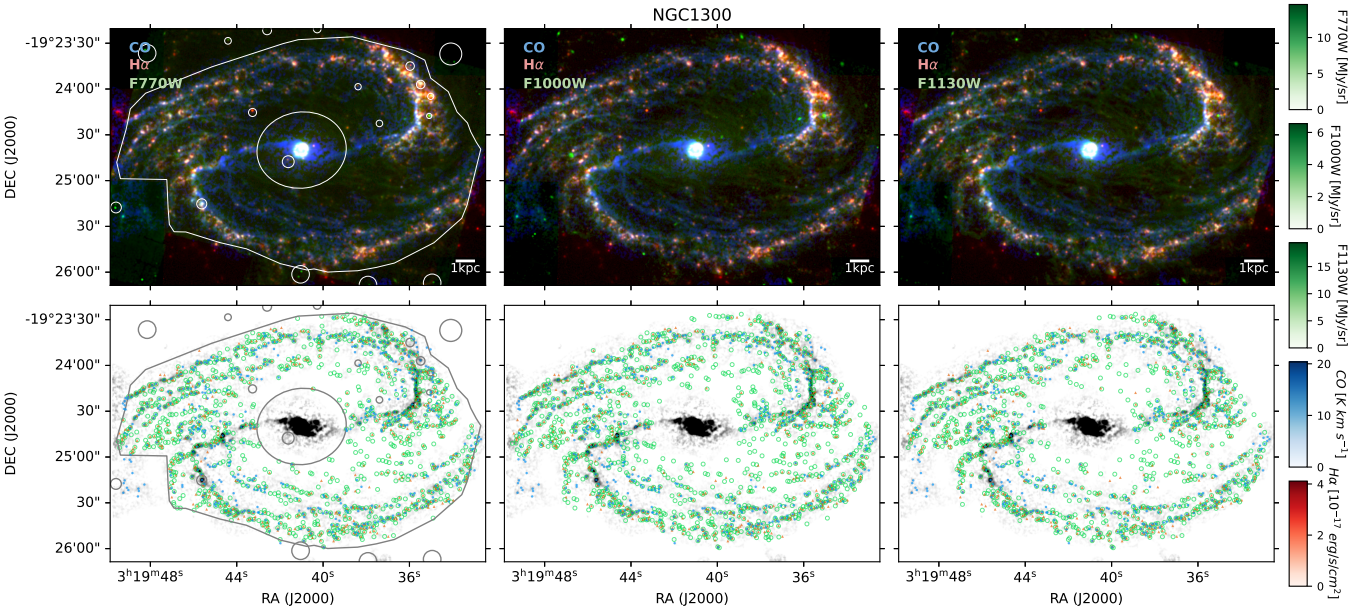

Figure 17. Similar to Figure 16, showing observations and identified emission peaks of NGC 1300.

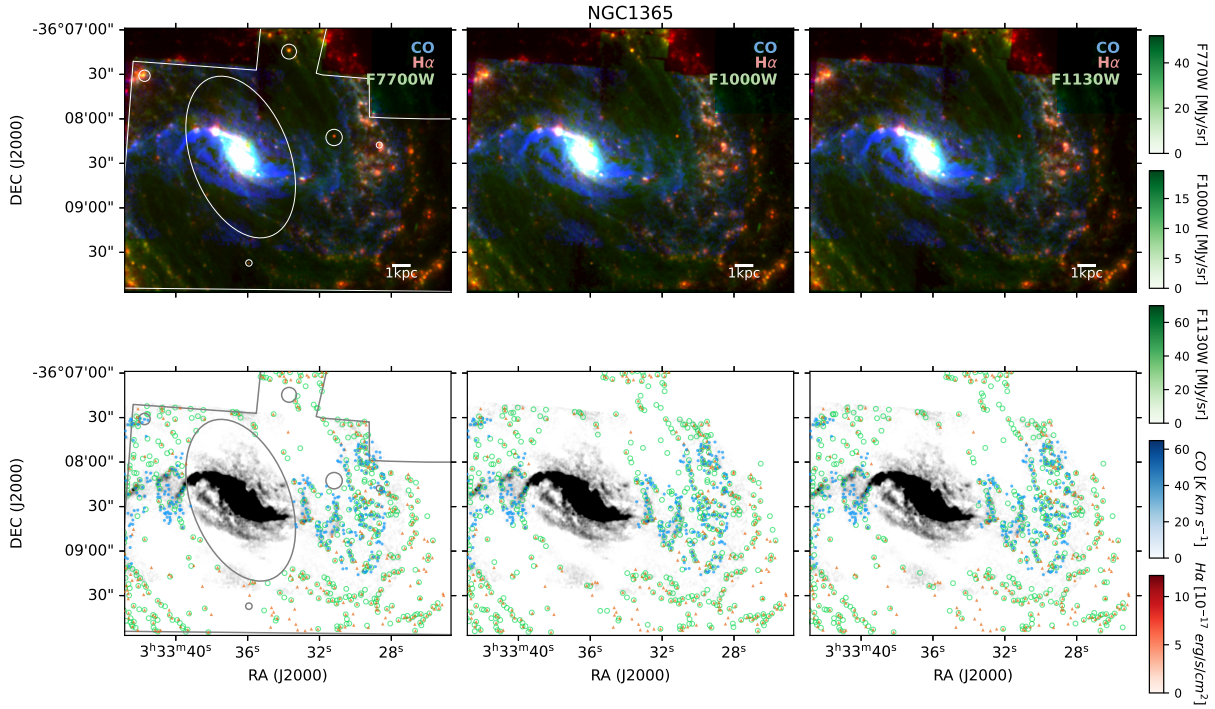

Figure 18. Similar to Figure 16, showing observations and identified emission peaks of NGC 1365. We note that for this galaxy, the CO observation has a smaller field of view.

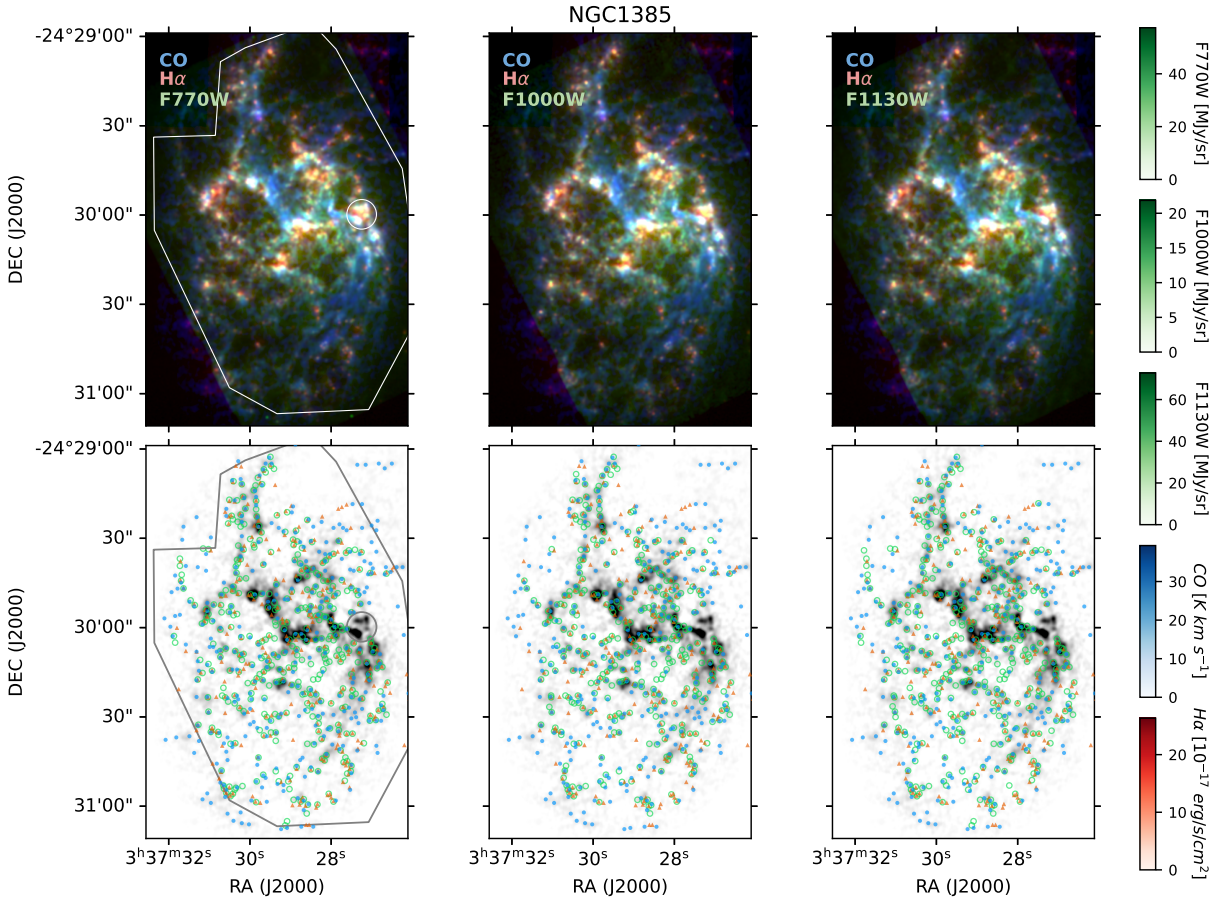

Figure 19. Similar to Figure 16, showing observations and identified emission peaks of NGC 1385.

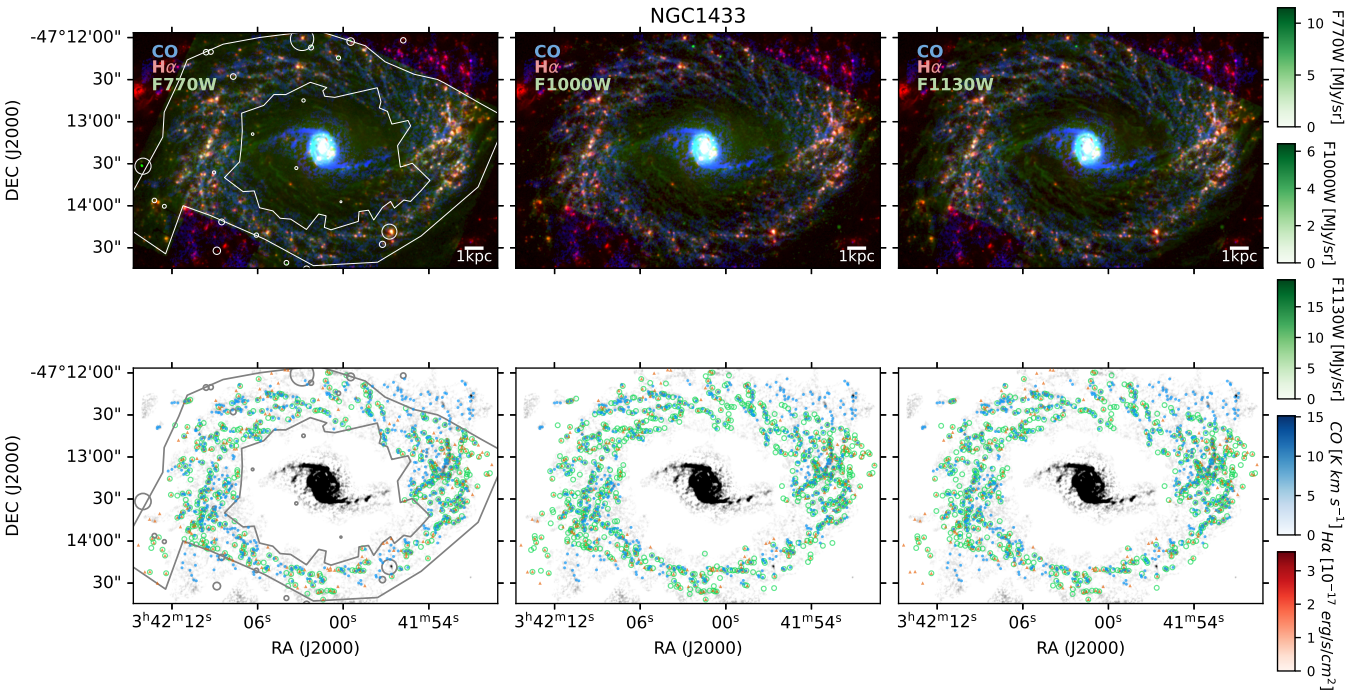

Figure 20. Similar to Figure 16, showing observations and identified emission peaks of NGC 1433.

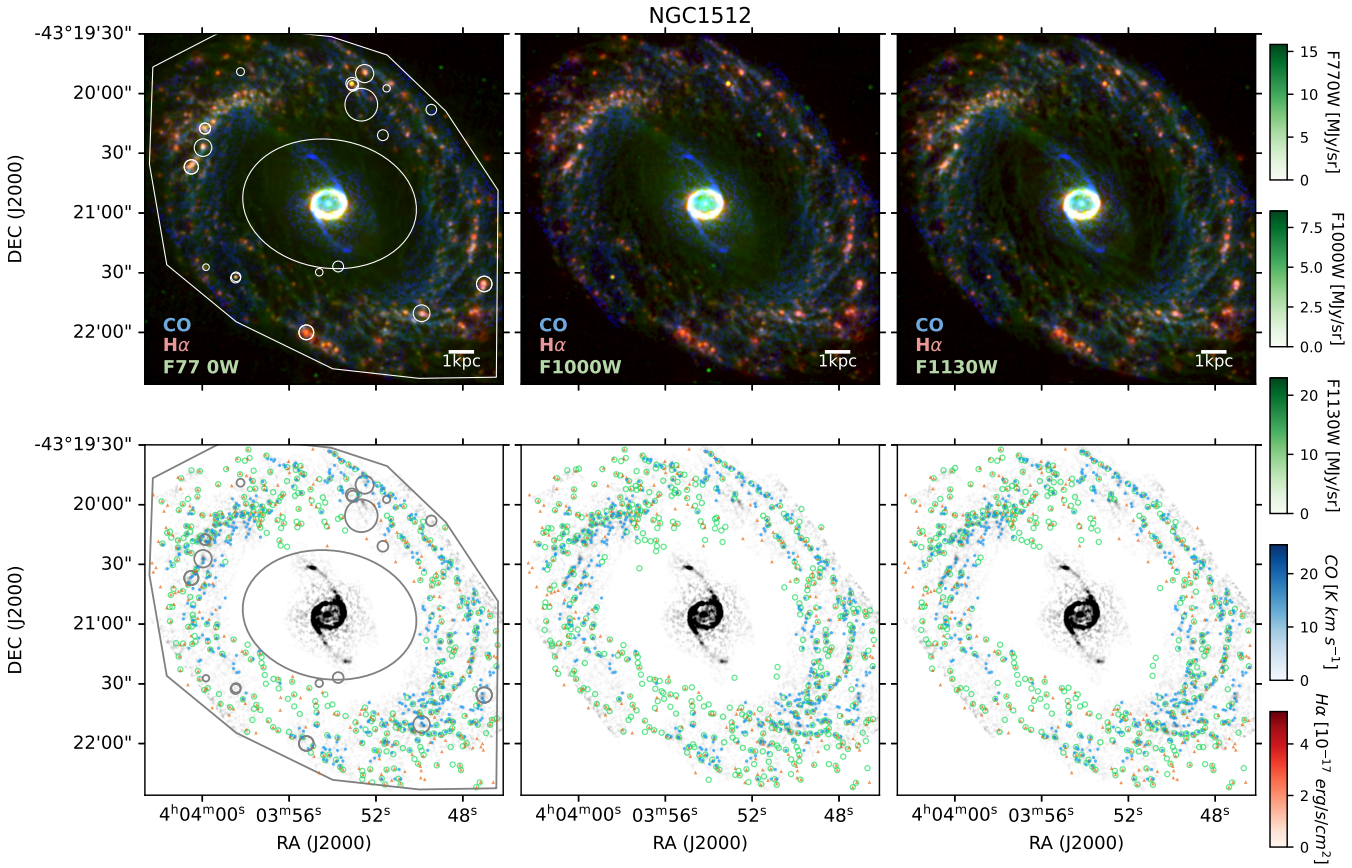

Figure 21. Similar to Figure 16, showing observations and identified emission peaks of NGC 1512.

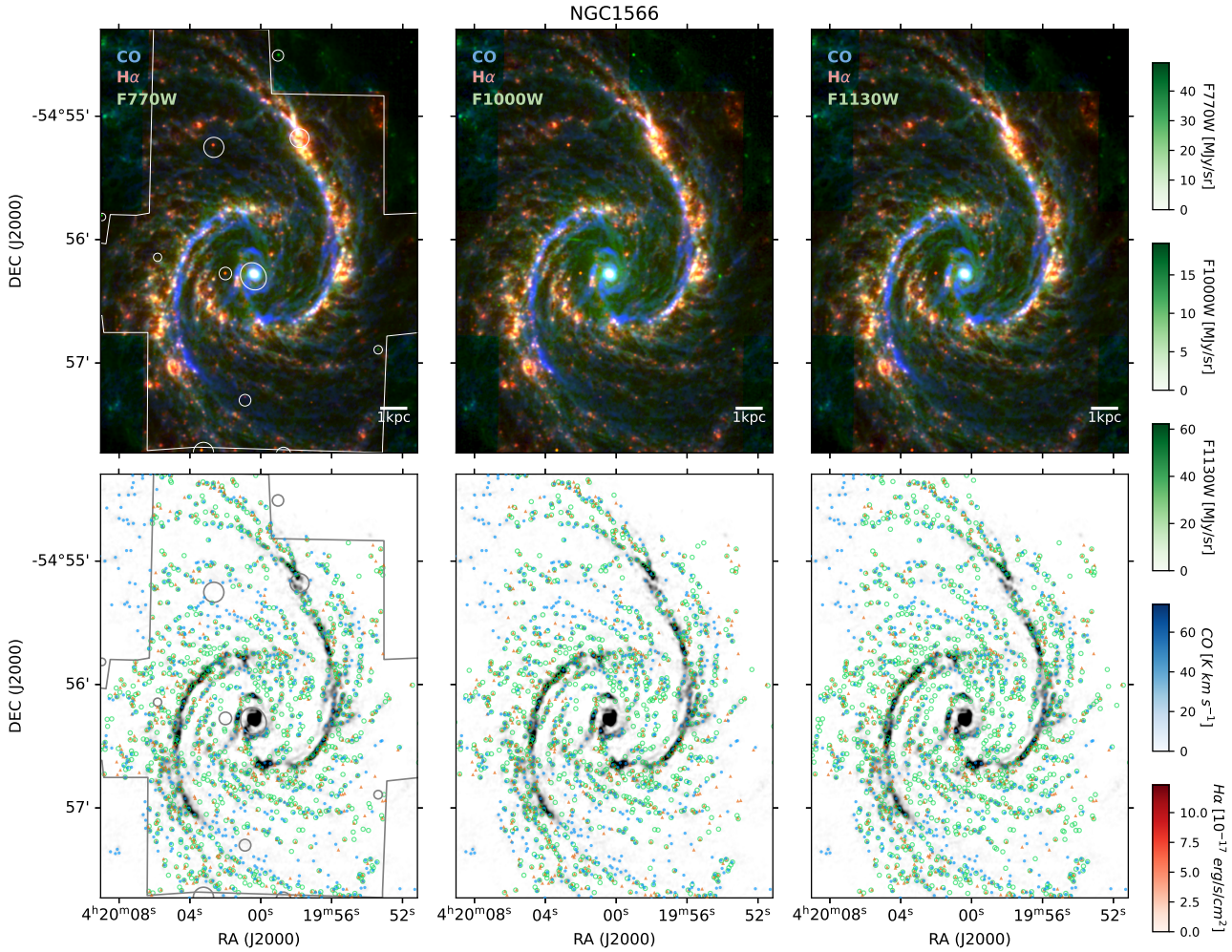

Figure 22. Similar to Figure 16, showing observations and identified emission peaks of NGC 1566.

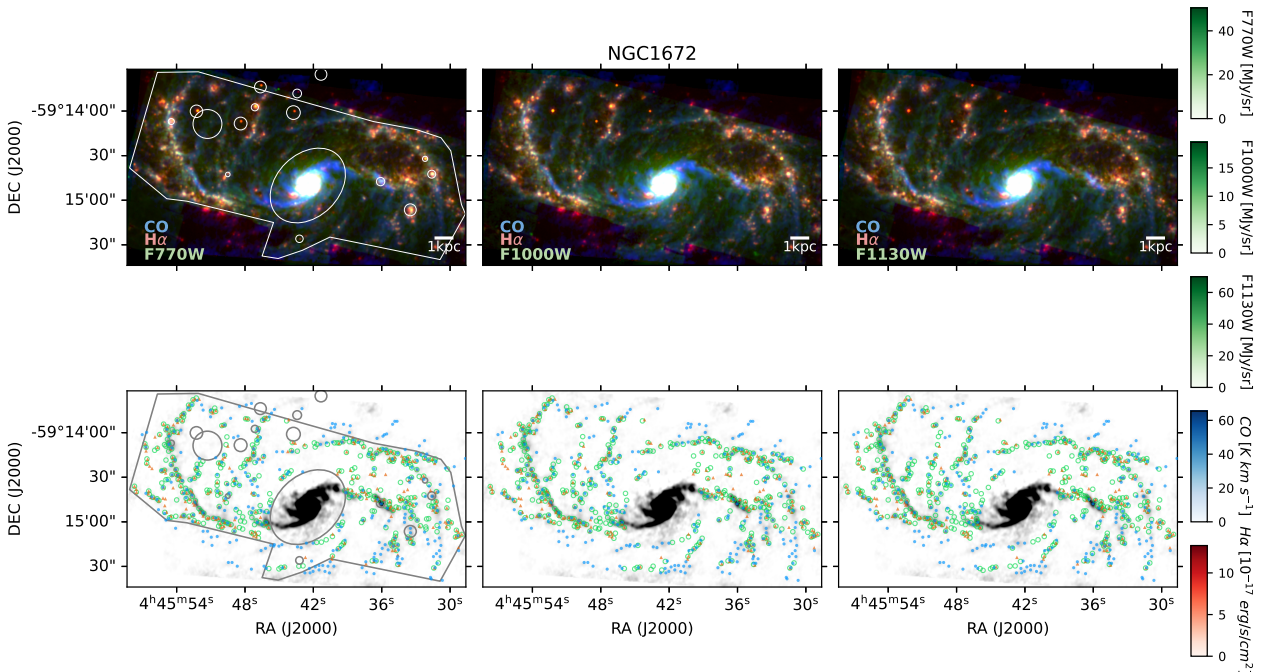

Figure 23. Similar to Figure 16, showing observations and identified emission peaks of NGC 1672.

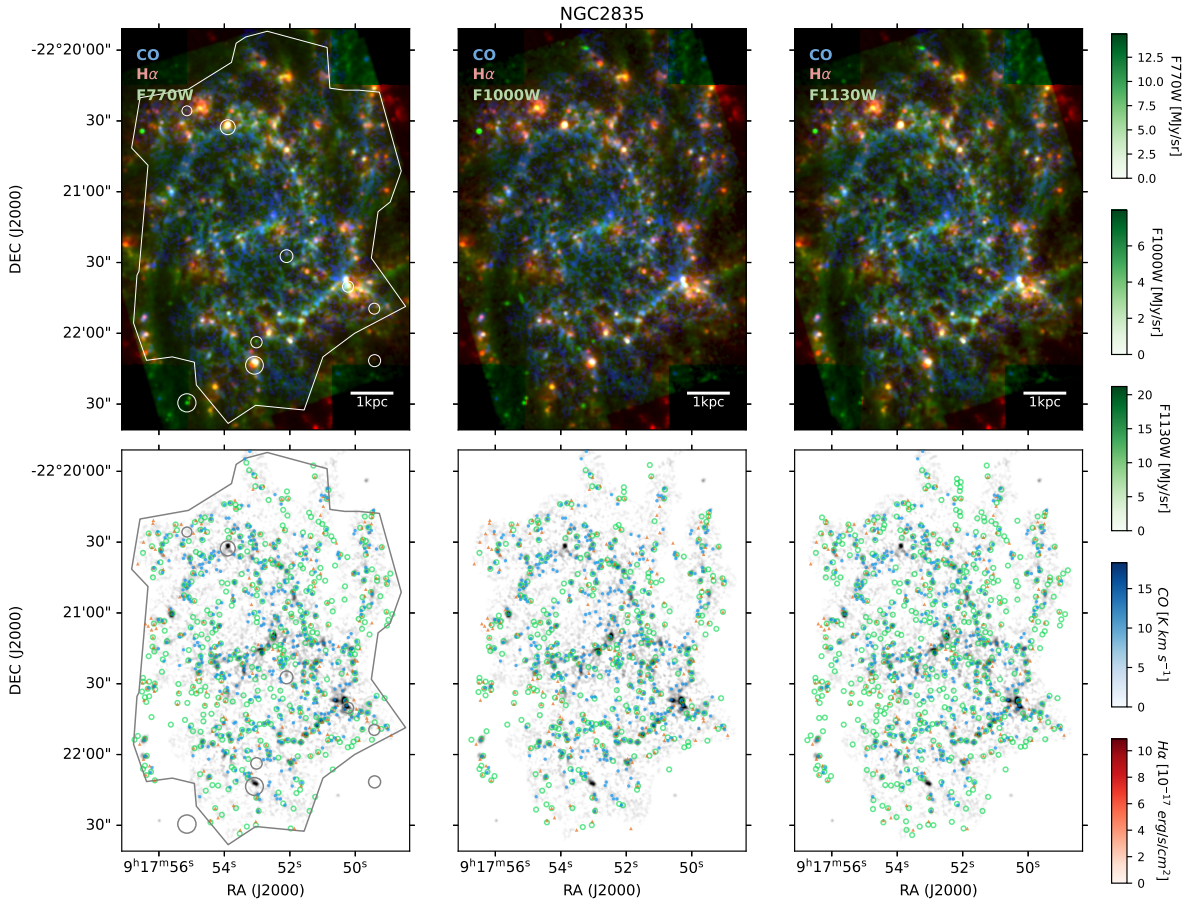

Figure 24. Similar to Figure 16, showing observations and identified emission peaks of NGC 2835.

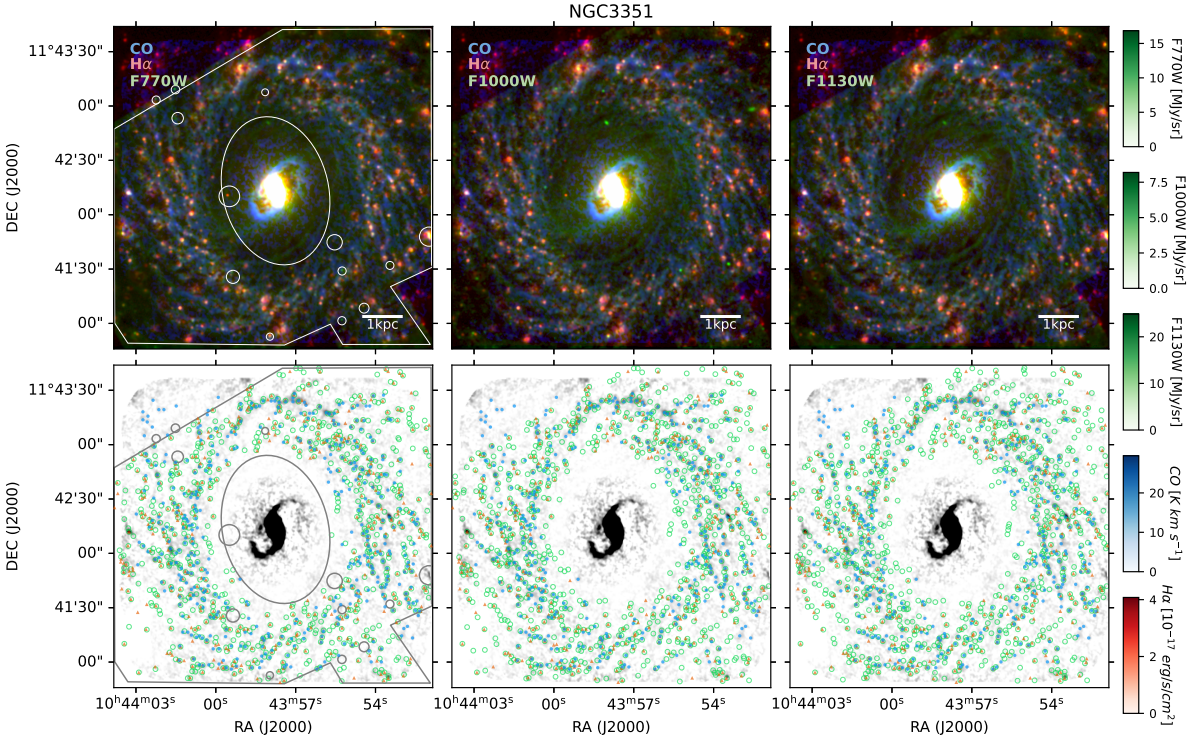

Figure 25. Similar to Figure 16, showing observations and identified emission peaks of NGC 3351.

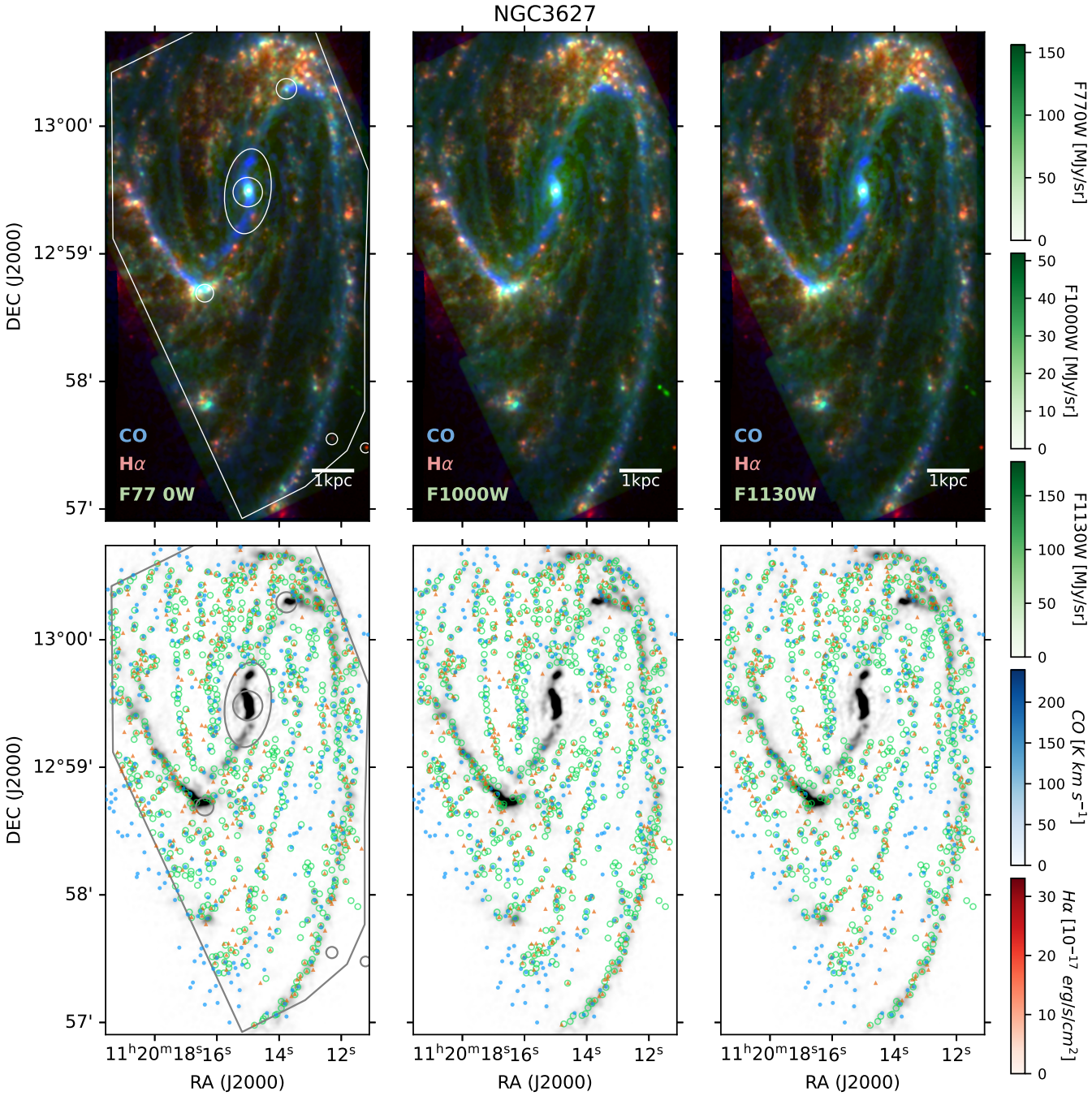

Figure 26. Similar to Figure 16, showing observations and identified emission peaks of NGC 3627.

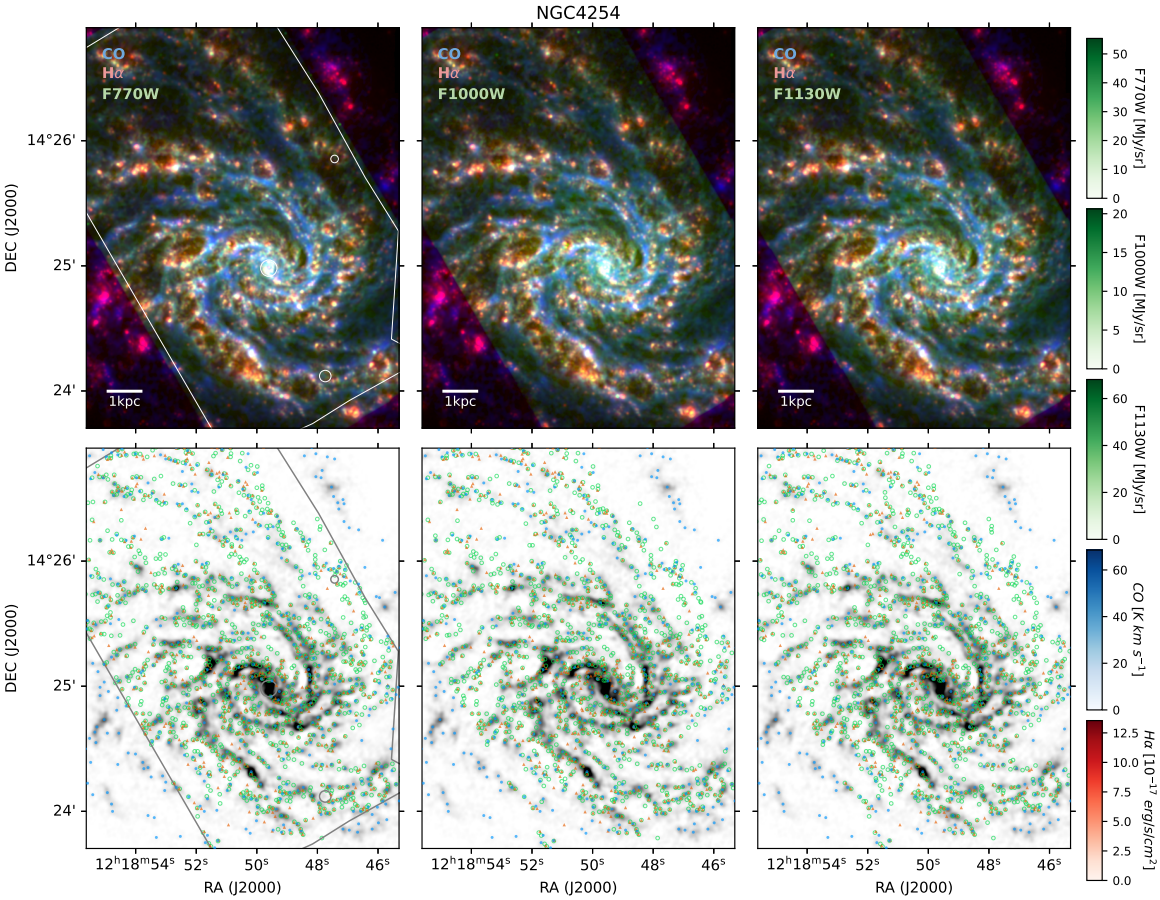

Figure 27. Similar to Figure 16, showing observations and identified emission peaks of NGC 4254.

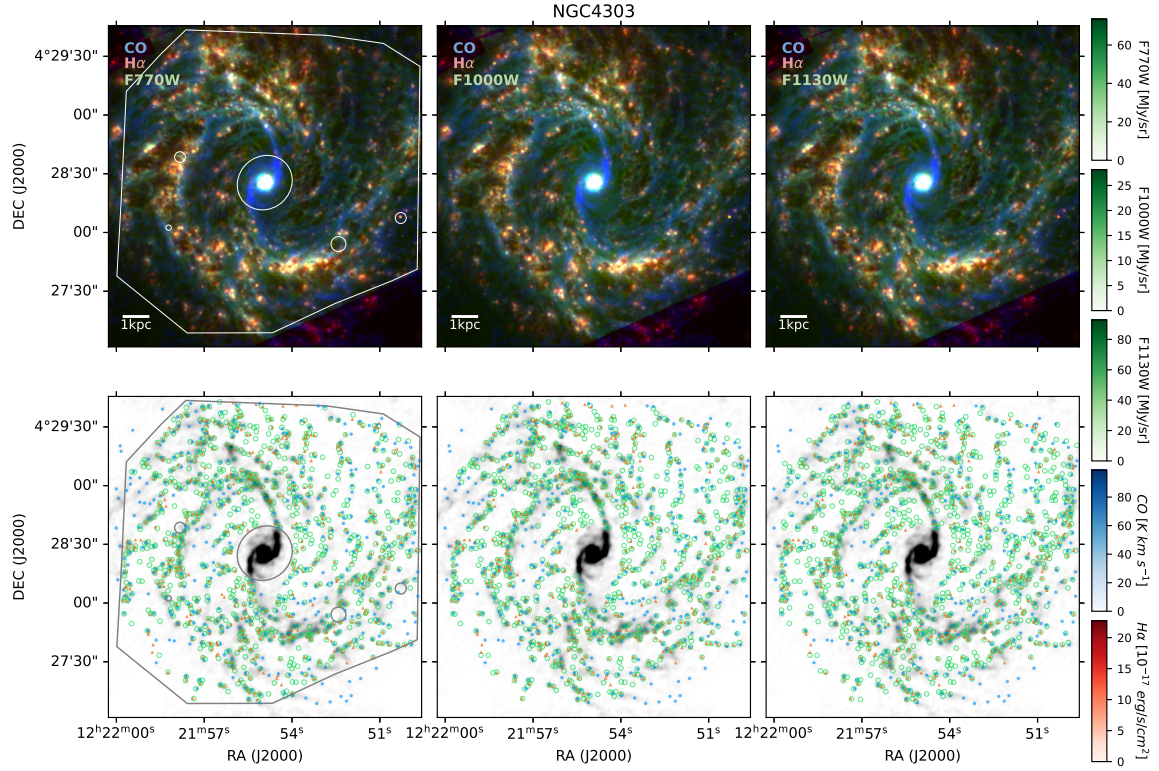

Figure 28. Similar to Figure 16, showing observations and identified emission peaks of NGC 4303.

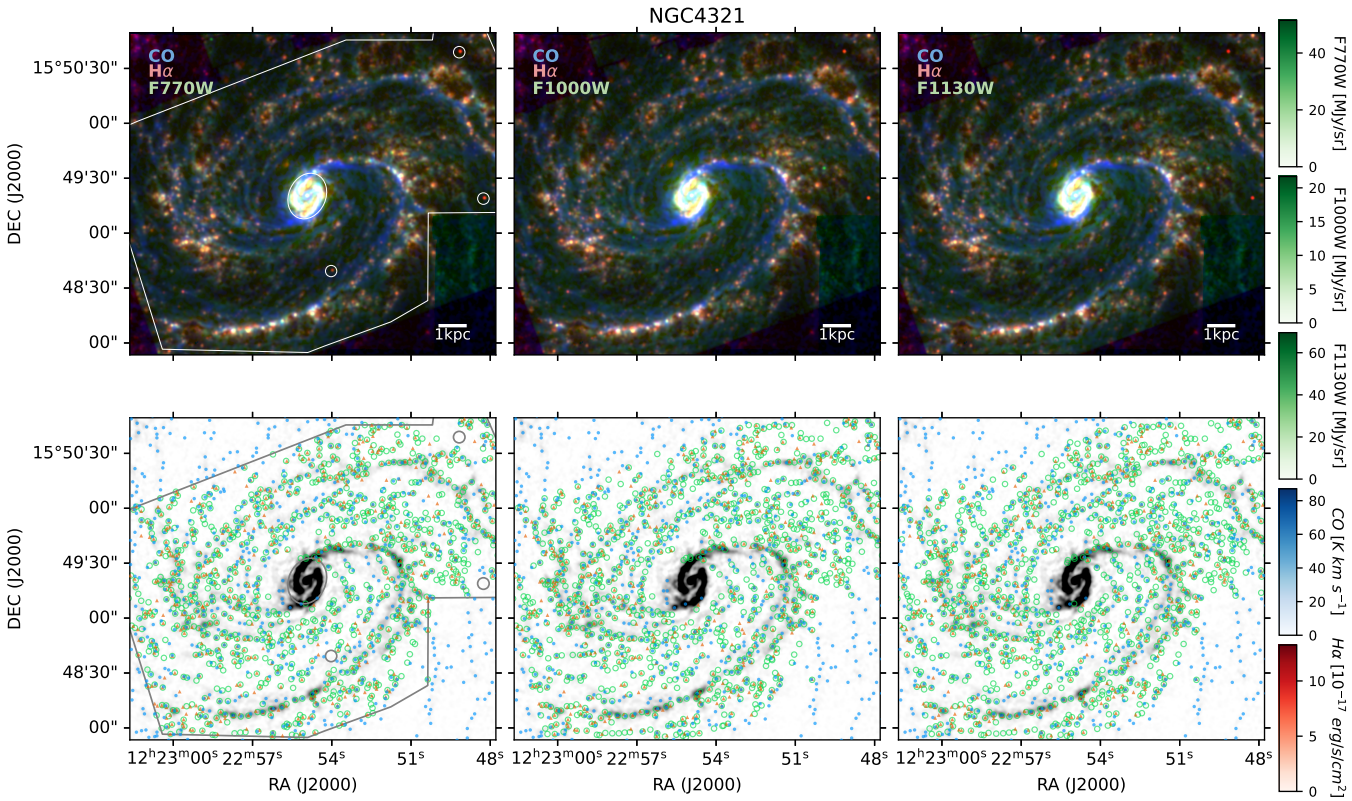

Figure 29. Similar to Figure 16, showing observations and identified emission peaks of NGC 4321.

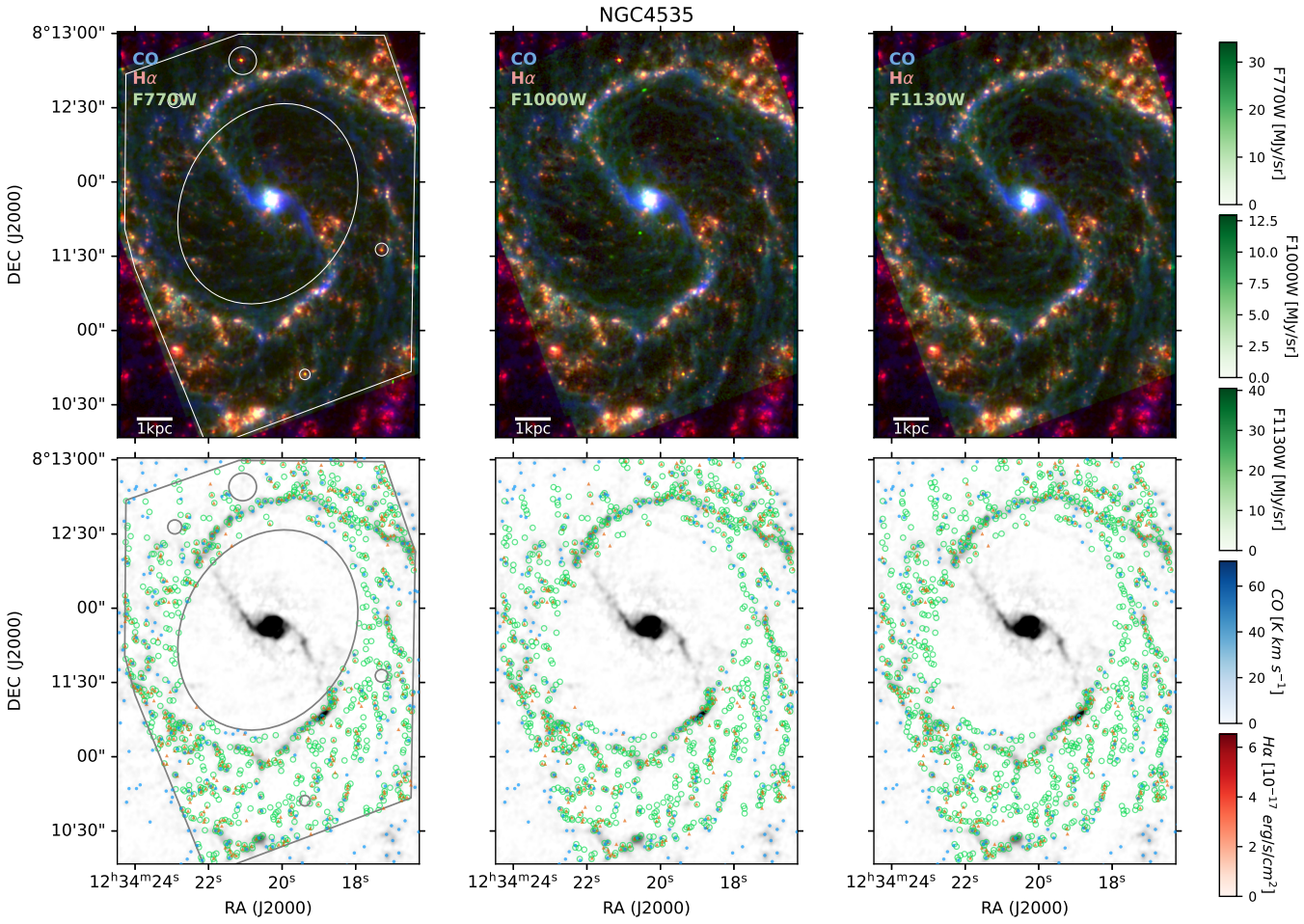

Figure 30. Similar to Figure 16, showing observations and identified emission peaks of NGC 4535.

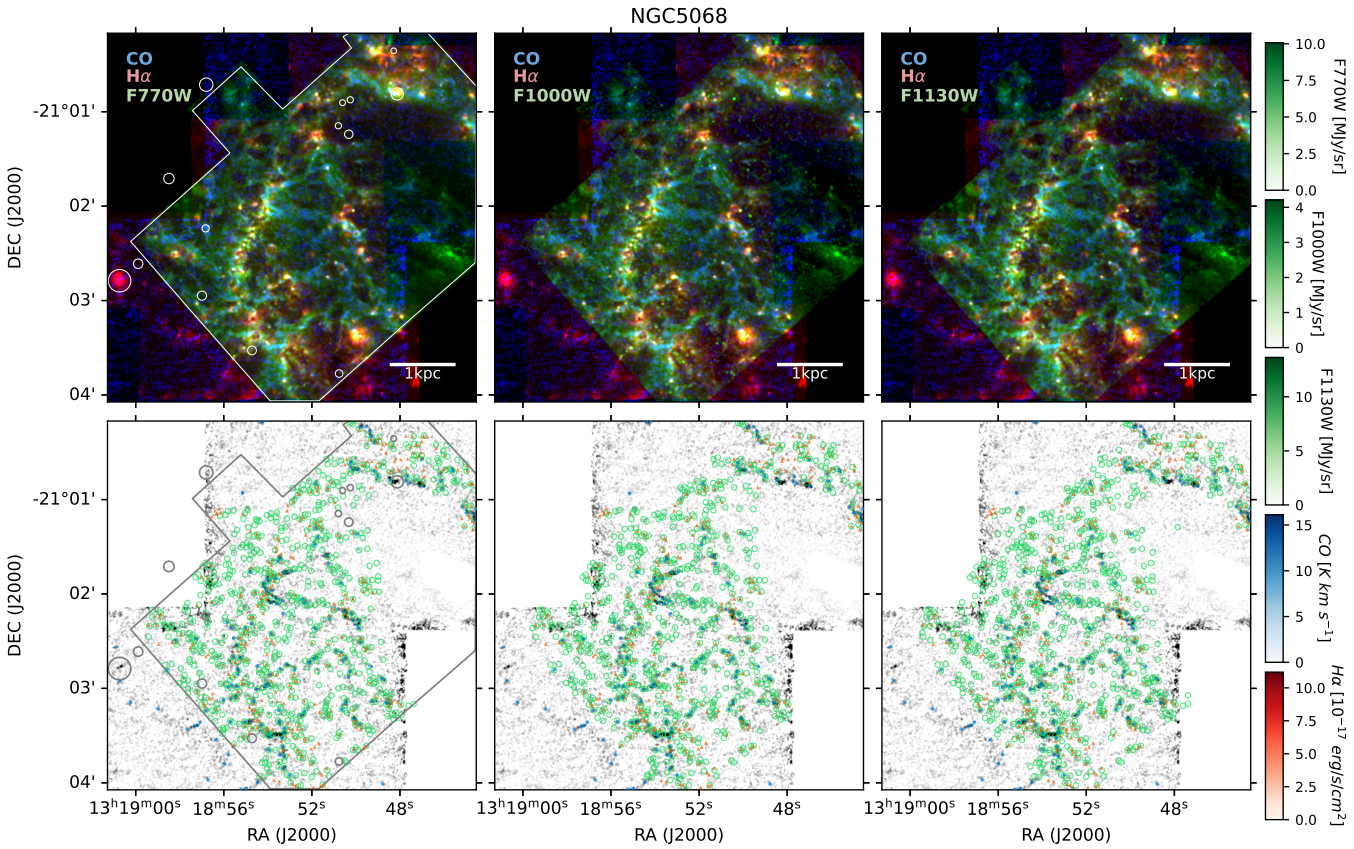

Figure 31. Similar to Figure 16, showing observations and identified emission peaks of NGC 5068.

Appendix B
Accuracy of Our Measurements

J. M. D. Kruijssen et al. (2018) listed a set of requirements that our measurements have to satisfy in order to be considered accurate within 30% error. We verify whether these are fulfilled for our constrained parameters (t_g, t_{fb}, and λ).

1. The mid-IR emitting timescale (t_g) and the Hα emitting timescale (t_s) should differ by no more than 1 order of magnitude. This is satisfied in all galaxies across all mid-IR bands with $|\log(t_g/t_s)| < 0.77$.
2. Individual star-forming regions should be sufficiently resolved with $\lambda > 1.5\, l_{ap,min}$. Across all mid-IR bands, this is not satisfied in NGC 1365, NGC 1512, and NGC 4321. Only in the analysis with 7.7 μm, two additional galaxies (NGC 1300 NGC 2835) suffer from insufficient resolution. In these galaxies, the ratio $\lambda/l_{ap,min}$ ranges from 1.3–1.4, indicating that only t_g is robust while t_{fb} and λ are upper limits.
3. We verify that the number of identified emission peaks in both mid-IR and Hα maps is above 35 (see also Figure 1, as well as Figures 16–31).
4. The measured mid-IR-to-Hα flux ratio on a small scale with apertures placed on mid-IR (Hα) peaks should not be below (above) the galactic average value. This is satisfied, as shown in Figure 2.
5. The global SFR of the analyzed region should not fluctuate by more than 0.2 dex during the last evolutionary cycle ($\tau = t_g + t_s - t_{fb}$), when averaged over a time period of t_g or t_s. Using the SFR history measured by I. Pessa et al. (2023), we verify that this condition is satisfied.
6. Regions undergoing evolution from gas to stars should be detected in both the mid-IR and the Hα map at some point of their lifecycle. This requirement can be verified by examining whether the sensitivity in mid-IR observations matches that of Hα observations. According to A. K. Leroy et al. (2023), the 1σ noise at 1.″7 of JWST mid-IR emission ranges from 0.2–0.5 $M_\odot$ pc^{-2}, obtained using a median CO-to-mid-IR ratio and a typical CO-to-H_2 conversion factor. We first estimate the minimum gas cloud mass corresponding to a typical 5σ sensitivity by multiplying the representative 1σ noise (0.3 $M_\odot$pc^{-2} across mid-IR bands) by 5 and the area corresponding to the size of 1.″7 at a typical distance of 15 Mpc. This yields a 5σ detection threshold corresponding to a gas cloud mass of $\sim 1.8 \times 10^4\, M_\odot$. We then multiply this by the mean star formation efficiency per cloud lifecycle as constrained within our method (3%; J. Kim et al. 2022) to obtain the expected minimum star-forming region mass ($\sim 500\, M_\odot$) from mid-IR observations. The minimum mass is compared to the minimum mass of the stellar population required to generate the typical 5σ sensitivity of the Hα map ($\sim 8 \times 10^{37}$ erg s^{-1} kpc^{-2}) on the scales of star-forming regions ($\lambda \sim 120$ pc). We obtain the initial mass using the STARBURST99 model with an assumption that star formation was instantaneous 5 Myr ago. We find that the minimum mass from mid-IR ($\sim 500\, M_\odot$) matches well with that from Hα ($\sim 600\, M_\odot$).

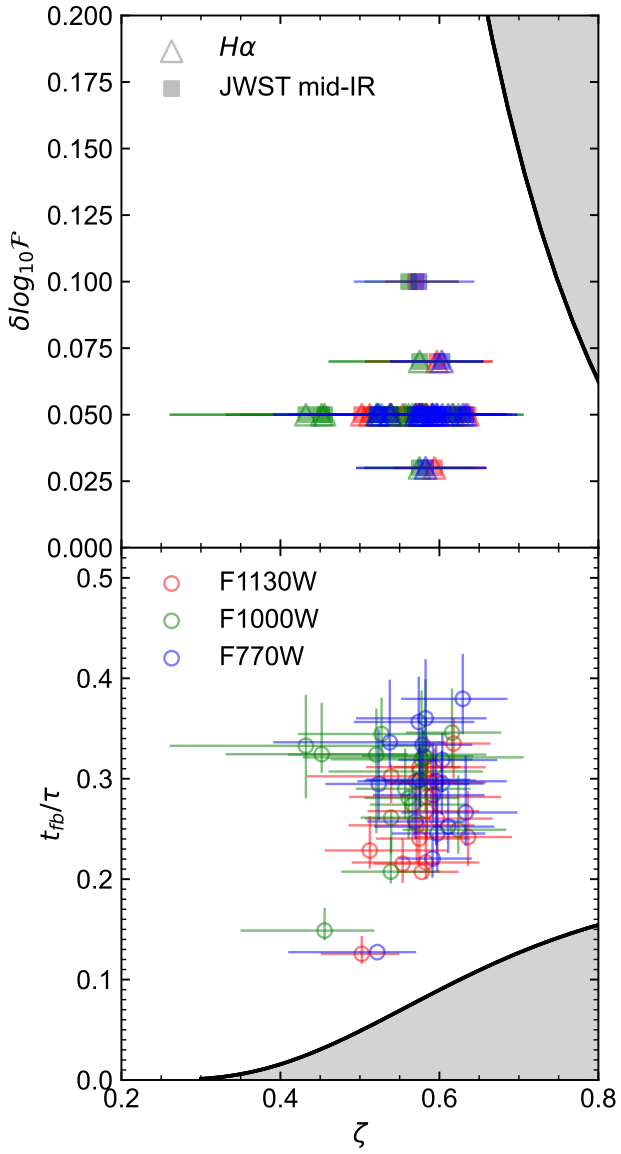

Figure 32. Top panel: the flux contrast ($\delta\log_{10}\mathcal{F}$) adopted during the peak identification for mid-IR (square) and Hα (triangles) observations shown as a function of the average filling factor (ζ). Across our analysis with each mid-IR band, shown as 7.7 μm (blue), 10 μm (green), and 11.3 μm (red), the adopted flux contrast is well below the upper limit (gray region). Bottom panel: measured $t_{\rm fb}/\tau$ as a function of ζ. In both panels, the gray region indicates the parameter space where the high filling factor biases our measurements of the $t_{\rm fb}$ (J. M. D. Kruijssen et al. 2018).

7. When regions are crowded, a small enough flux contrast ($\delta\log_{10}\mathcal{F}$) needs to be adopted during the peak identification process to distinguish adjacent peaks. J. M. D. Kruijssen et al. (2018) provided upper limits for $\delta\log_{10}\mathcal{F}$ as a function of ζ, which represents the filling factor of emission peaks. The ζ is defined as $2r/\lambda$, where the r is the mean radius of gas or SFR tracer peaks. We obtain the average ζ by weighting the ζ for each gas and SFR tracer with their associated timescales. Figure 32 shows that the adopted $\delta\log_{10}\mathcal{F}$ is well below the upper limit.
8. Galaxies with a high filling factor (ζ) might be incorrectly constrained to have a longer feedback timescale. In Figure 32, we compare the ratio between the feedback timescale ($t_{\rm fb}$) and the total duration of the evolutionary cycle ($\tau = t_{\rm g} + t_{\rm s} - t_{\rm fb}$) as a function of ζ to the analytical predictions of J. M. D. Kruijssen et al. (2018), outlining the region where the constrained $t_{\rm fb}$ should be considered to be an upper limit due to the high filling factor. We find that none of our measurements fall into this region.
9. As shown in the bottom panel of Figure 32, we ensure that the $t_{\rm fb}/\tau$ is above 0.05 and below 0.95 in all of our measurements.
10. Similarly to requirement (5) above, during the last evolutionary cycle (τ), the SFR should not vary by more than 0.2 dex when averaged over a time period of $t_{\rm fb}$. This is satisfied using the same argument as above.
11. After masking the dense central regions of the galaxy, we ensure that visual inspection does not identify areas with substantial blending.

To summarize, we find that almost all of the requirements are satisfied except for condition (2). This is not satisfied for NGC 1365, NGC 1512, and NGC 4321 across all three mid-IR bands. NGC 1300 and NGC 2835 also fail to satisfy this condition for our measurements with 7.7 μm as the gas tracer. This implies that the measured $t_{\rm fb}$ and λ are upper limits for this subset of galaxies, as indicated in Table 3.

Appendix C
Impact of Masking Extremely Bright Peaks

Our method uses flux averages and its distributions to determine the mid-IR-to-Hα flux ratios and their associated uncertainties. Therefore, exceedingly bright emission peaks that do not represent the overall cloud and H II region population can potentially bias our measured timescales. For example, in the LMC, when 30 Doradus is included in the analysis, constituting $\sim$20% of the total Hα emission, J. L. Ward et al. (2022) found that the 1σ uncertainty of the derived molecular gas cloud lifetime almost doubles from $t_{\rm g}^{\rm CO} = 11.8^{+2.7}_{-2.2}$ Myr to $12.8^{+5.1}_{-3.6}$ Myr. M. Chevance et al. (2020a) showed that masking a very bright molecular cloud (referred to as the "headlight" cloud in C. N. Herrera et al. 2020) makes small differences in derived timescales when obtained averaging over the entire galaxy. However, the difference becomes significant when focusing on smaller regions within the galaxy, which makes the headlight cloud dominate more than 10% of the total CO flux. Then, the measured molecular gas cloud lifetime changes from $t_{\rm g}^{\rm CO} = 16^{+4.3}_{-2.8}$ Myr with mask to >25 Myr without masking the "headlight" cloud, when the analysis is performed on a radial bin with a width of 1 kpc (M. Chevance et al. 2020a).

In Table 4, we show how the masking of bright peaks changes our timescale measurements and the fraction of flux enclosed in the mask relative to the total emission in the galactic disk with centers excluded. We show comparisons for all of the galaxies that required additional masking of peaks compared to the masks adopted in J. Kim et al. (2022). We find that our measurements with and without bright peaks masked agree within 1σ uncertainties. The masking also does not seem to affect uncertainties, most likely because the bright peaks do not dominate the total flux as much as 30 Doradus (20% in Hα flux), and our values are obtained by averaging over the whole galaxy.

Table 4

Comparison of Our Measurements of Mid-IR Emitting Timescale ($t_g^{7.7\ \mu m}$), Feedback Timescale ($t_{fb}^{7.7\ \mu m}$), and Region Separation Length ($\lambda^{7.7\ \mu m}$), with and without Masking Exceedingly Bright Emission Peaks

Galaxy	With Exceedingly Bright Peaks Masked			Without Masking			F_{mask}	
	$t_g^{7.7\ \mu m}$ (Myr)	$t_{fb}^{7.7\ \mu m}$ (Myr)	$\lambda^{7.7\ \mu m}$ (pc)	$t_g^{7.7\ \mu m}$ (Myr)	$t_{fb}^{7.7\ \mu m}$ (Myr)	$\lambda^{7.7\ \mu m}$ (pc)	7.7 μm (%)	Hα (%)
NGC 1087	$21.5^{+2.3}_{-3.4}$	$6.6^{+1.1}_{-1.1}$	125^{+23}_{-17}	$20.5^{+3.1}_{-4.0}$	$6.4^{+1.2}_{-1.1}$	122^{+86}_{-23}	2.6	5.3
NGC 1300	$19.7^{+1.8}_{-1.7}$	<7.4	<150	$18.1^{+2.2}_{-1.7}$	<7.4	<167	2.9	5.5
NGC 1365	$18.2^{+4.1}_{-2.7}$	<6.9	<237	$17.5^{+3.5}_{-2.8}$	<6.8	<249	1.7	6.2
NGC 1512	$11.7^{+1.8}_{-1.2}$	<5.5	<238	$13.8^{+1.5}_{-1.7}$	<5.7	<215	7.9	16.4
NGC 1672	$19.0^{+2.2}_{-3.3}$	$7.0^{+1.1}_{-0.9}$	194^{+104}_{-30}	$23.6^{+3.0}_{-5.8}$	$8.7^{+0.2}_{-1.9}$	182^{+100}_{-36}	5.3	11.3
NGC 2835	$15.7^{+2.1}_{-2.1}$	<4.9	<148	$16.8^{+2.5}_{-2.5}$	<5.3	<156	4.1	8.4

Note. F_{mask} shows the fraction of masked flux (in each 7.7 μm and Hα observation) relative to the total flux in the galactic disk, excluding the central region.

ORCID iDs

Jaeyeon Kim https://orcid.org/0000-0002-0432-6847
Mélanie Chevance https://orcid.org/0000-0002-5635-5180
Lise Ramambason https://orcid.org/0000-0002-9190-9986
Kathryn Kreckel https://orcid.org/0000-0001-6551-3091
Ralf S. Klessen https://orcid.org/0000-0002-0560-3172
Daniel A. Dale https://orcid.org/0000-0002-5782-9093
Adam K. Leroy https://orcid.org/0000-0002-2545-1700
Karin Sandstrom https://orcid.org/0000-0002-4378-8534
Ryan Chown https://orcid.org/0000-0001-8241-7704
Thomas G. Williams https://orcid.org/0000-0002-0012-2142
Sumit K. Sarbadhicary https://orcid.org/0000-0002-4781-7291
Francesco Belfiore https://orcid.org/0000-0002-2545-5752
Frank Bigiel https://orcid.org/0000-0003-0166-9745
Enrico Congiu https://orcid.org/0000-0002-8549-4083
Oleg V. Egorov https://orcid.org/0000-0002-4755-118X
Eric Emsellem https://orcid.org/0000-0002-6155-7166
Simon C. O. Glover https://orcid.org/0000-0001-6708-1317
Kathryn Grasha https://orcid.org/0000-0002-3247-5321
Annie Hughes https://orcid.org/0000-0002-9181-1161
J. M. Diederik Kruijssen https://orcid.org/0000-0002-8804-0212
Janice C. Lee https://orcid.org/0000-0002-2278-9407
Debosmita Pathak https://orcid.org/0000-0003-2721-487X
Ismael Pessa https://orcid.org/0000-0002-0873-5744
Erik Rosolowsky https://orcid.org/0000-0002-5204-2259
Jiayi Sun https://orcid.org/0000-0003-0378-4667
Jessica Sutter https://orcid.org/0000-0002-9183-8102
David A. Thilker https://orcid.org/0000-0002-8528-7340

References

Agertz, O., Pontzen, A., Read, J. I., et al. 2020, MNRAS, 491, 1656
Anand, G. S., Lee, J. C., Van Dyk, S. D., et al. 2021, MNRAS, 501, 3621
Aniano, G., Draine, B. T., Gordon, K. D., & Sandstrom, K. 2011, PASP, 123, 1218
Astropy Collaboration, Price-Whelan, A. M., Lim, P. L., et al. 2022, ApJ, 935, 167
Astropy Collaboration, Price-Whelan, A. M., Sipőcz, B. M., et al. 2018, AJ, 156, 123
Astropy Collaboration, Robitaille, T. P., Tollerud, E. J., et al. 2013, A&A, 558, A33
Barnes, A. T., Longmore, S. N., Dale, J. E., et al. 2020, MNRAS, 498, 4906
Belfiore, F., Leroy, A. K., Williams, T. G., et al. 2023, A&A, 678, A129
Belfiore, F., Santoro, F., Groves, B., et al. 2022, A&A, 659, A26
Bialy, S., Burkhart, B., Seifried, D., et al. 2025, ApJ, 982, 24
Bigiel, F., Leroy, A., Walter, F., et al. 2008, AJ, 136, 2846
Blitz, L., Fukui, Y., Kawamura, A., et al. 2007, in Protostars and Planets V, ed. B. Reipurth, D. Jewitt, & K. Keil (Tucson, AZ: Univ. Arizona Press), 81
Bolatto, A. D., Wolfire, M., & Leroy, A. K. 2013, ARA&A, 51, 207
Calzetti, D., Kennicutt, R. C., Engelbracht, C. W., et al. 2007, ApJ, 666, 870
Chastenet, J., Sandstrom, K., Chiang, I.-D., et al. 2019, ApJ, 876, 62
Chastenet, J., Sutter, J., Sandstrom, K., et al. 2023, ApJL, 944, L11
Chevance, M., Kruijssen, J. M. D., Hygate, A. P. S., et al. 2020a, MNRAS, 493, 2872
Chevance, M., Kruijssen, J. M. D., Krumholz, M. R., et al. 2022, MNRAS, 509, 272
Chevance, M., Kruijssen, J. M. D., & Longmore, S. N. 2025, arXiv:2501.13160
Chevance, M., Kruijssen, J. M. D., Vazquez-Semadeni, E., et al. 2020b, SSRv, 216, 50
Chevance, M., Krumholz, M. R., McLeod, A. F., et al. 2023, in ASP Conf. Ser. 534, Protostars and Planets VII, ed. S. Inutsuka et al. (San Francisco, CA: ASP), 1
Chevance, M., Madden, S. C., Fischer, C., et al. 2020c, MNRAS, 494, 5279
Chiang, I.-D., Sandstrom, K. M., Chastenet, J., et al. 2024, ApJ, 964, 18
Chown, R., Leroy, A. K., Sandstrom, K., et al. 2025, ApJ, 983, 64
Chown, R., Li, C., Parker, L., et al. 2021, MNRAS, 500, 1261
Clark, P. C., Glover, S. C. O., Klessen, R. S., & Bonnell, I. A. 2012, MNRAS, 424, 2599
Corbelli, E., Braine, J., Bandiera, R., et al. 2017, A&A, 601, A146
Dale, D. A., Gil de Paz, A., Gordon, K. D., et al. 2007, ApJ, 655, 863
Diaz, A. I., Terlevich, E., Vilchez, J. M., Pagel, B. E. J., & Edmunds, M. G. 1991, MNRAS, 253, 245
Draine, B. T., Dale, D. A., Bendo, G., et al. 2007, ApJ, 663, 866
Draine, B. T., & Li, A. 2007, ApJ, 657, 810
Draine, B. T., Li, A., Hensley, B. S., et al. 2021, ApJ, 917, 3
Egorov, O. V., Kreckel, K., Sandstrom, K. M., et al. 2023, ApJL, 944, L16
Eibensteiner, C., Sun, J., Bigiel, F., et al. 2024, A&A, 691, A163
Elmegreen, B. G. 2000, ApJ, 530, 277
Emsellem, E., Schinnerer, E., Santoro, F., et al. 2022, A&A, 659, A191
Engargiola, G., Plambeck, R. L., Rosolowsky, E., & Blitz, L. 2003, ApJS, 149, 343
Feldmann, R., Gnedin, N. Y., & Kravtsov, A. V. 2011, ApJ, 732, 115
Fujimoto, Y., Chevance, M., Haydon, D. T., Krumholz, M. R., & Kruijssen, J. M. D. 2019, MNRAS, 487, 1717
Galliano, F., Galametz, M., & Jones, A. P. 2018, ARA&A, 56, 673
Gao, Y., Tan, Q.-H., Gao, Y., et al. 2022, ApJ, 940, 133
Gordon, K. D., Engelbracht, C. W., Rieke, G. H., et al. 2008, ApJ, 682, 336
Grasha, K., Calzetti, D., Adamo, A., et al. 2019, MNRAS, 483, 4707
Grasha, K., Calzetti, D., Bittle, L., et al. 2018, MNRAS, 481, 1016
Groves, B., Kreckel, K., Santoro, F., et al. 2023, MNRAS, 520, 4902
Hassani, H., Rosolowsky, E., Leroy, A. K., et al. 2023, ApJL, 944, L21
Haydon, D. T., Kruijssen, J. M. D., Chevance, M., et al. 2020, MNRAS, 498, 235
Hensley, B. S., & Draine, B. T. 2023, ApJ, 948, 55
Herrera, C. N., Pety, J., Hughes, A., et al. 2020, A&A, 634, A121
Hirota, A., Egusa, F., Baba, J., et al. 2018, PASJ, 70, 73
Holm, S. 1979, Scandinavian Journal of Statistics, 6, 65
Hu, Z., Wibking, B. D., Krumholz, M. R., & Federrath, C. 2024, MNRAS, 534, 2426

Hunter, J. D. 2007, CSE, 9, 90
Hygate, A. P. S. 2020, PhD Thesis, Ruperto-Carola-University of Heidelberg
Hygate, A. P. S., Kruijssen, J. M. D., Chevance, M., et al. 2019, MNRAS, 488, 2800
Jameson, K. E., Bolatto, A. D., Leroy, A. K., et al. 2016, ApJ, 825, 12
Jeffreson, S. M. R., Krumholz, M. R., Fujimoto, Y., et al. 2021, MNRAS, 505, 3470
Jones, A. G., Bendo, G. J., Baes, M., et al. 2015, MNRAS, 448, 168
Kawamura, A., Mizuno, Y., Minamidani, T., et al. 2009, ApJS, 184, 1
Keller, B. W., Kruijssen, J. M. D., & Chevance, M. 2022, MNRAS, 514, 5355
Kennicutt, R. C., & Evans, N. J. 2012, ARA&A, 50, 531
Kennicutt, R. C. J. 1998, ARA&A, 36, 189
Kim, J., Chevance, M., Kruijssen, J. M. D., et al. 2021, MNRAS, 504, 487
Kim, J., Chevance, M., Kruijssen, J. M. D., et al. 2022, MNRAS, 516, 3006
Kim, J., Chevance, M., Kruijssen, J. M. D., et al. 2023, ApJL, 944, L20
Klessen, R. S., & Glover, S. C. O. 2016, SAAS, 43, 85
Kreckel, K., Faesi, C., Kruijssen, J. M. D., et al. 2018, ApJL, 863, L21
Kreckel, K., Ho, I. T., Blanc, G. A., et al. 2019, ApJ, 887, 80
Kruijssen, J. M. D., & Longmore, S. N. 2014, MNRAS, 439, 3239
Kruijssen, J. M. D., Pfeffer, J. L., Crain, R. A., & Bastian, N. 2019a, MNRAS, 486, 3134
Kruijssen, J. M. D., Schruba, A., Hygate, A. P. S., et al. 2018, MNRAS, 479, 1866
Kruijssen, J. M. D., Schruba, A., Chevance, M., et al. 2019b, Natur, 569, 519
Lai, T. S. Y., Armus, L., U, V., et al. 2022, ApJL, 941, L36
Lai, T. S. Y., Smith, J. D. T., Baba, S., Spoon, H. W. W., & Imanishi, M. 2020, ApJ, 905, 55
Lang, P., Meidt, S. E., Rosolowsky, E., et al. 2020, ApJ, 897, 122
Lee, J. C., Sandstrom, K. M., Leroy, A. K., et al. 2023, ApJL, 944, L17
Leitherer, C., Schaerer, D., Goldader, J. D., et al. 1999, ApJS, 123, 3
Leroy, A. K., Hughes, A., Liu, D., et al. 2021b, ApJS, 255, 19
Leroy, A. K., Sandstrom, K., Rosolowsky, E., et al. 2023, ApJL, 944, L9
Leroy, A. K., Sandstrom, K. M., Lang, D., et al. 2019, ApJS, 244, 24
Leroy, A. K., Schinnerer, E., Hughes, A., et al. 2017, ApJ, 846, 71
Leroy, A. K., Schinnerer, E., Hughes, A., et al. 2021a, ApJS, 257, 43
Leroy, A. K., Walter, F., Sandstrom, K., et al. 2013, AJ, 146, 19
Li, Y., Crocker, A. F., Calzetti, D., et al. 2013, ApJ, 768, 180
Lu, A., Boyce, H., Haggard, D., et al. 2022, MNRAS, 514, 5035
Lucas, W. E., Bonnell, I. A., & Dale, J. E. 2020, MNRAS, 493, 4700
Madden, S. C., Cormier, D., Hony, S., et al. 2020, A&A, 643, A141
Makarov, D., Prugniel, P., Terekhova, N., Courtois, H., & Vauglin, I. 2014, A&A, 570, A13
Mayker Chen, N., Leroy, A. K., Lopez, L. A., et al. 2023, ApJ, 944, 110
Mayker Chen, N., Leroy, A. K., Sarbadhicary, S. K., et al. 2024, AJ, 168, 5
McKinney, W. 2010, Proc. 9th Python in Science Conf., ed. S. van der Walt & M. Millman, (Austin, TX: SciPy), 56
Meidt, S. E., Hughes, A., Dobbs, C. L., et al. 2015, ApJ, 806, 72
Meixner, M., Gordon, K. D., Indebetouw, R., et al. 2006, AJ, 132, 2268
Miura, R. E., Kohno, K., Tosaki, T., et al. 2012, ApJ, 761, 37
Oey, M. S., López-Hernández, J., Kellar, J. A., et al. 2017, ApJ, 844, 63
Onodera, S., Kuno, N., Tosaki, T., et al. 2010, ApJL, 722, L127
Pan, H.-A., Schinnerer, E., Hughes, A., et al. 2022, ApJ, 927, 9
Pathak, D., Leroy, A. K., Thompson, T. A., et al. 2024, AJ, 167, 39
Paturel, G., Andernach, H., Bottinelli, L., et al. 1997, A&AS, 124, 109
Pedrini, A., Adamo, A., Calzetti, D., et al. 2024, ApJ, 971, 32
Pessa, I., Schinnerer, E., Sanchez-Blazquez, P., et al. 2023, A&A, 673, A147
Pineda, J. L., Langer, W. D., Goldsmith, P. F., et al. 2017, ApJ, 839, 107
Rosolowsky, E., Hughes, A., Leroy, A. K., et al. 2021, MNRAS, 502, 1218
Sandstrom, K. M., Chastenet, J., Sutter, J., et al. 2023b, ApJL, 944, L7
Sandstrom, K. M., Koch, E. W., Leroy, A. K., et al. 2023a, ApJL, 944, L8
Schinnerer, E., Hughes, A., Leroy, A., et al. 2019, ApJ, 887, 49
Schinnerer, E., & Leroy, A. K. 2024, ARA&A, 62, 369
Schruba, A., Kruijssen, J. M. D., & Leroy, A. K. 2019, ApJ, 883, 2
Schruba, A., Leroy, A. K., Walter, F., Sandstrom, K., & Rosolowsky, E. 2010, ApJ, 722, 1699
Scott, D. W. 1992, Multivariate Density Estimation (Wiley: New York)
Semenov, V. A., Kravtsov, A. V., & Gnedin, N. Y. 2021, ApJ, 918, 13
Silk, J. 1997, ApJ, 481, 703
Smith, J. D. T., Draine, B. T., Dale, D. A., et al. 2007, ApJ, 656, 770
Smith, R. J., Glover, S. C. O., Clark, P. C., Klessen, R. S., & Springel, V. 2014, MNRAS, 441, 1628
Sternberg, A., Bialy, S., & Gurman, A. 2024, ApJ, 960, 8
Sun, J., Leroy, A. K., Ostriker, E. C., et al. 2020, ApJ, 892, 148
Sun, J., Leroy, A. K., Rosolowsky, E., et al. 2022, AJ, 164, 43
Sutter, J., Sandstrom, K., Chastenet, J., et al. 2024, ApJ, 971, 178
Syed, J., Soler, J. D., Beuther, H., et al. 2022, A&A, 657, A1
Teng, Y.-H., Sandstrom, K. M., Sun, J., et al. 2023, ApJ, 950, 119
Thilker, D. A., Lee, J. C., Deger, S., et al. 2023, ApJL, 944, L13
Toribio San Cipriano, L., Domínguez-Guzmán, G., Esteban, C., et al. 2017, MNRAS, 467, 3759
Tumlinson, J., Peeples, M. S., & Werk, J. K. 2017, ARA&A, 55, 389
Turner, J. A., Dale, D. A., Lilly, J., et al. 2022, MNRAS, 516, 4612
Verley, S., Corbelli, E., Giovanardi, C., & Hunt, L. K. 2009, A&A, 493, 453
Virtanen, P., Gommers, R., Oliphant, T. E., et al. 2020, NatMe, 17, 261
Ward, J. L., Chevance, M., Kruijssen, J. M. D., et al. 2020, MNRAS, 497, 2286
Ward, J. L., Kruijssen, J. M. D., Chevance, M., Kim, J., & Longmore, S. N. 2022, MNRAS, 516, 4025
Waskom, M. L. 2021, JOSS, 6, 3021
Whitcomb, C. M., Sandstrom, K., Leroy, A., & Smith, J. D. T. 2023, ApJ, 948, 88
Williams, J. P., de Geus, E. J., & Blitz, L. 1994, ApJ, 428, 693
Williams, T., Egorov, O., Rosolowsky, E., et al. 2023, Physics at High Angular resolution in Nearby GalaxieS - JWST ("PHANGS-JWST"), STScI/MAST, doi:10.17909/EW88-JT15
Williams, T. G., Kreckel, K., Belfiore, F., et al. 2022, MNRAS, 509, 1303
Williams, T. G., Lee, J. C., Larson, K. L., et al. 2024, ApJS, 273, 13
Wolfire, M. G., Hollenbach, D., & McKee, C. F. 2010, ApJ, 716, 1191
Wolfire, M. G., Vallini, L., & Chevance, M. 2022, ARA&A, 60, 247
Zabel, N., Davis, T. A., Sarzi, M., et al. 2020, MNRAS, 496, 2155